Design and prototyping of two high resolution boron based neutron detectors BODELAIRE and BASTARD

Tim Wagner

Masterarbeit in Physik
angefertigt im Physikalischen Institut

vorgelegt der
Mathematisch-Naturwissenschaftlichen Fakultät
der
Rheinischen Friedrich-Wilhelms-Universität
Bonn

August 2017

I hereby declare that this thesis was formulated by myself and that no sources or tools other than those cited were used.

Bonn, ...
                    Date   Signature

1. Gutachter: Prof. Klaus Desch
2. Gutachter: Prof. Ian Brock

Acknowledgements

At this point I would like to thank everyone who supported me during the work on my master thesis. First and foremost I would like to thank Klaus Desch for the opportunity to write the master thesis in his group. I would like to thank Jochen Kaminski and Markus Köhli for their support and valuable discussions we had. Additionally I would also like to thank Ian Brock for evaluating my thesis.

Special thanks to all people who took part in the TPC-meetings on Mondays for the discussions and tips regarding my thesis. Finally I would also like to thank my colleagues in the office for the relaxing time and fun we had.

Contents

Introduction

In particle physics it is always necessary to detect all kinds of particles. For charged particles this is rather easy, as they ionize the medium they traverse. If a particle is not charged it will not ionize the medium and the task to detect it will get more complicated. This thesis will focus on the detection of a specific neutral particle: The neutron. As the neutron is not charged it can not be detected directly, but has to undergo a reaction to be detected. For high energy neutrons there is the calorimeter for detection of strongly interacting particles, but what about low energy neutrons?

There is a different way to detect low energy neutrons. Typically nuclear reactions are used to create charged particles and the reaction products are detected in order to conclude that there was a neutron interaction. For a long time counting tubes were the most commonly used method to detect them. The counting tubes are filled with Helium-3 (He-3), where the neutrons interact with. Also the He-3 serves as a counting gas, thus only one component is necessary. The reaction of the neutron with the He-3 produces a proton and tritium, which are both charged.

With the need for more security after 9/11 also the need to detect neutrons grew, as neutrons are also emitted by radioactive materials. He-3 counting tubes have been widely used for this purpose. As a result of that the price for He-3 grew rapidly, as the only source for He-3 is the decay of thermonuclear weapons. In thermonuclear weapons tritium is used as a component. Tritium decays to He-3 with a half life time of approximately 12 years. The demand was way higher than the supply and the previous stockpile of He-3 shrank and the price increased. Another downside of the He-3 counting tubes is their spatial, as they can only detect if there was a neutron in the gas volume, but not where exactly.

Thus new detectors with high spatial resolution are needed for neutron detection. In Bonn two detectors, BASTARD and BODELAIRE, are being developed with the aim of high rate capability and high spatial and time resolution. Both detectors are based on another neutron conversion material which is boron-10. The reaction of a neutron with boron-10 also produces two charged particles which can be detected, but it is not usable as a counting gas. A gas which could be used as a counting gas and contains boron would be boron trifluoride. Unfortunately it is highly toxic and therefore rarely used. Instead solid boron-10, in the form of boron carbide, is used for neutron conversion. The detectors will be operated with Ar CO_2, a standard counting gas. Additionally to achieve high spatial resolution they will have a highly granular

readout which is based on a gas electron multiplier (GEM) foil for the BASTARD detector. The BODELAIRE detector uses the working principle of a time projection chamber (TPC) with the GridPix as a readout chip.

In this thesis the BASTARD detector has been designed. This will include the design of the structure on the GEM foil and also the case of the detector. For the BODELAIRE detector a prototype will be designed and built. The prototype measures the characteristics of converted neutrons showing the capabilities of the GridPix chip. The characteristics will be studied and a reconstruction for the neutron interaction point will be developed. This is done in order to use neutrons to resolve macroscopic structures and determine the spatial resolution of the constructed prototype.

Physics background

2.1 Physics of neutrons

The neutron was discovered in 1932 by James Chadwick [1]. He found that in a reaction of beryllium and alpha particles in addition to gamma rays [2] also an unknown neutral particle with approximately the mass of the proton was produced. He called that particle the neutron and described the reaction which produces the neutron from Beryllium irradiated with alpha particles as

$$\text{Be}^9 + \alpha \rightarrow \text{C}^{12} + \text{n}.$$
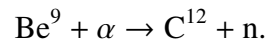
This discovery lead to a new field of physics to be explored in the following years.

2.1.1 Properties of the neutron

The mass of the neutron was determined by experiments on the most simple bound system the deuteron, as it only consists of a proton and a neutron. The mass of the deuteron and the mass of the proton were well known and with the binding energy of the deuteron, the neutron mass could be derived. The neutron mass was measured to be $1.008665\,\text{u}^1$ [3], which is slightly heavier than the proton with a mass of $1.007276\,\text{u}$. As the neutron is slightly heavier it can undergo a β-decay into a proton, electron and electron-anti-neutrino. The decay of the neutron was first observed in 1948 by Arthur Snell [4] and its mean lifetime was determined to be $(880.2 \pm 1.0)\,\text{s}$ [5]. It is not charged and has a spin of $1/2$ [6]. The neutron mainly interacts via nuclear interaction or scatters with nuclei. Some of the properties are summarized in table 2.1.

2.1.2 Neutron interactions

The main interaction neutrons undergo with matter is scattering. When neutrons have low energies additionally they can be absorbed by specific elements. The energy scales for a neutron are classified as follows: For energies above $10\,\text{MeV}$ neutrons are considered high energetic,

---

^{1} 1 u is equal to 1.660277×10^{-24} g, which is 1/12 of the mass of a C^{12} atom.

The Neutron	
Mass	$(1.00866491588 \pm 0.00000000049)\,\text{u}$
	$(939.5654133 \pm 0.0000058)\,\text{MeV}$
Lifetime	$(880.2 \pm 1.0)\,\text{s}$
Charge	0
Spin	$\frac{1}{2}$

Table 2.1: Properties of the neutron. [5]

above 1 MeV medium energetic, above 50 eV as fast neutrons, between 0.5 eV and 50 eV as epithermal, below 0.5 eV as thermal neutrons and below 1 meV as cold neutrons.

The neutron can form a compound state with a nucleus, which has a lifetime of more than 10^{-17} s. The nucleus is in an excited state and the excitation energy equals the kinetic and binding energy of the neutron. Upon decay of the compound state a neutron with the same kinetic energy as the captured one is released. This process is called compound elastic scattering or resonance scattering, because the cross section shows resonance like behavior. Also the excitation energy can be released as one or several photons instead of releasing the neutron, which is then called radiative capture. The resulting nucleus is often unstable and decays via β-decay. An other way to deexcite the nucleus is that a charged particle or several neutrons can be emitted. The resulting emission of a charged particle is called charged capture and for the neutral particles it is called neutral capture. If only one neutron gets released, but with a lower energy compared to the incoming neutron, it is called inelastic scattering, as the nucleus gained some energy and is still in an excited state. Finally also fission can occur for the heaviest nuclei.

Neutrons can also interact with nuclei without forming a compound nucleus. For most neutrons this is done via direct elastic scattering, where direct refers to scattering without the formation of a compound state. While direct elastic scattering can always occur, the formation of a compound nucleus is a resonance reaction, as it can only be formed if the kinetic energy if the incident neutron corresponds to an excitation level of the compound nucleus. The cross section for direct elastic scattering slowly varies with the energy, whereas the cross section for the formation of a compound nucleus has sharp maxima at resonance energies. While direct elastic scattering is possible for all energies, the formation of a compound nucleus is mostly possible for the lower neutron energies, meaning fast neutrons and neutrons with less energy.

All these interactions can happen with all elements, although the cross sections vary drastically. Especially between different isotopes of the same element the cross section varies largely. For thermal neutrons with energies in the order of milli-electron volts there are multiple isotopes with a high cross section for neutron capture. Those isotopes for example are helium-3, lithium-6, boron-10, cadmium-113, gadolinium-155 or 157 and uranium-235. The reactions and cross sections for these elements are given in table 2.2. In the table on can see which elements are useful for detection and which are not as useful, because of the resulting products. The first three elements are useful for usage in a detector, as they produce multiple charged particles which are easily detectable. Cadmium and gadolinium are not as useful for usage in a detector, as the resulting product is a photon and most of the background when detecting neutrons are

also photons. As cadmium has a high neutron capture cross section for thermal neutrons with a steep fall of the cross section for higher energies, it is often used as a thermal neutron shield instead.

Element	Reaction			Cross section
^{3}He	^{3}He + n	$\rightarrow$	^{3}H + p + 764 keV	5 327 b
^{6}Li	^{6}Li + n	$\rightarrow$	^{3}H + α + 4.78 MeV	936 b
^{10}B	^{10}B + n	$\rightarrow$	^{7}Li + α + 2.79 MeV (6%)	3 840 b
	^{10}B + n	$\rightarrow$	^{7}Li* + α + 2.31 MeV (94%)	
^{113}Cd	^{113}Cd + n	$\rightarrow$	^{114}Cd + γ + 9.04 MeV	20 000 b
^{155}Gd	^{155}Gd + n	$\rightarrow$	^{156}Gd+γ+e$^-$+(30–180) keV	56 200 b
^{157}Gd	^{157}Gd + n	$\rightarrow$	^{158}Gd+γ+e$^-$+(30–180) keV	242 000 b
^{235}U	^{235}U + n	$\rightarrow$	fission fragments + 160 MeV	690 b

Table 2.2: Typical elements which capture neutrons. All the cross sections are given for neutrons with an energy of 25.2 meV which corresponds to a velocity of $2\,200\,\mathrm{m\,s^{-1}}$. [7]

2.1.3 Boron as a neutron converter

For the detector in this thesis boron-10 was chosen to be the neutron conversion material. The reaction of a neutron with boron-10 leads to two charged particles as fragments like indicated in table 2.2. The alpha particle can be easily detected, whereas the lithium ion has less kinetic energy due to its mass. Additionally the energy loss of the lithium ion is higher thus the range of the lithium ions is less than half compared to the range of the alpha particle in boron, which is $4\,\mu$m. In order to have a quantitative measure for the contribution of the different conversion products to the spectrum, the simulated spectrum can be seen in figure 2.1. It shows the simulated spectra for thicknesses of the boron layer of (100–1 900) nm. The alpha particle or helium ion can be still detected for layer thicknesses of more than 2 000 nm, but lithium does not significantly contribute for layer thicknesses beyond 1 500 nm. Thus the layer thickness has to be below 1 500 nm in order to be able to detect both conversion products. The maximal range of the conversion products in a counting gas, for example Ar CO_2, is approximately 9 mm for the highest energy helium, whereas the lithium typically has shorter tracks [8]. The energy loss and range of those particles can be seen in figure 2.2.

2.1.4 Neutron sources

As neutrons have a limited lifetime, there are no free neutrons existing in nature and they must be produced via some reaction.
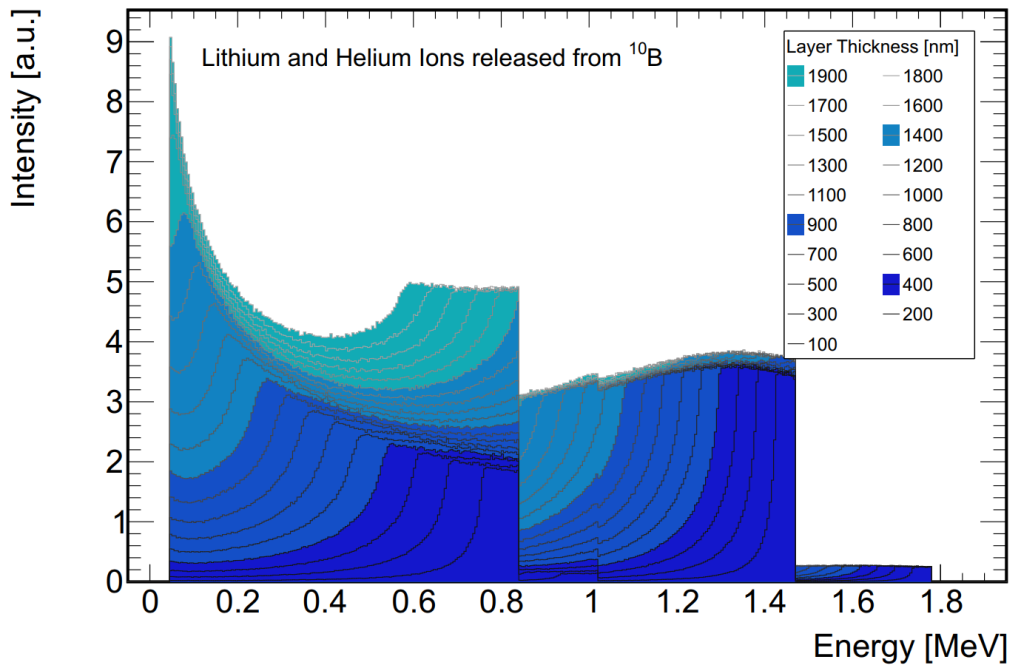There are different means of obtaining free neutrons and some of them will be discussed here. The method known to most people is fission. Some of the heaviest nuclei can decay due to spontaneous fission. During fission there are always some neurons produced, thus they can be
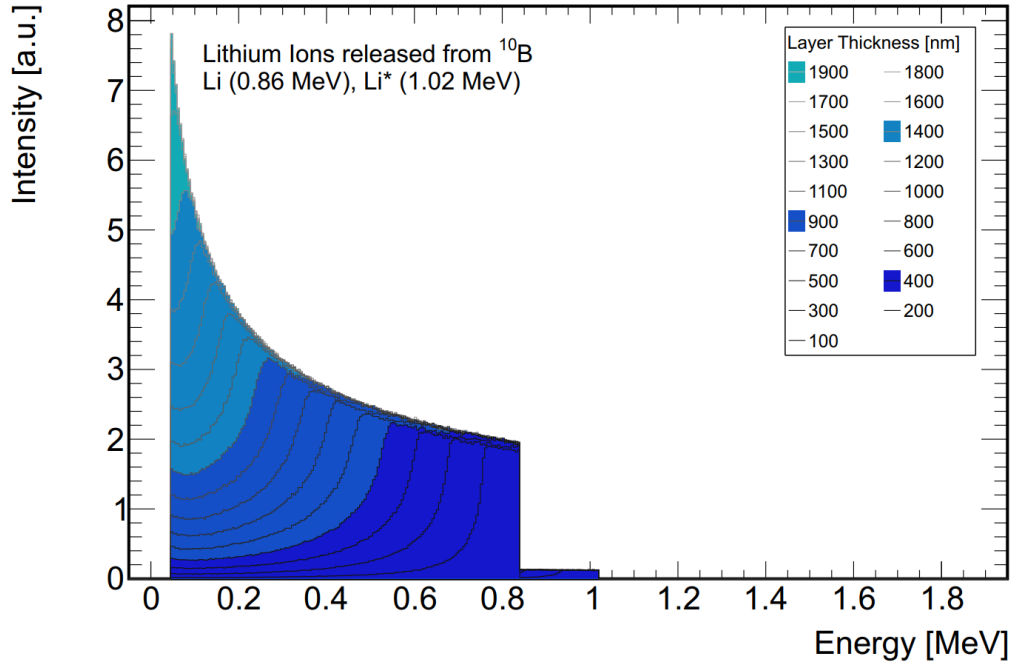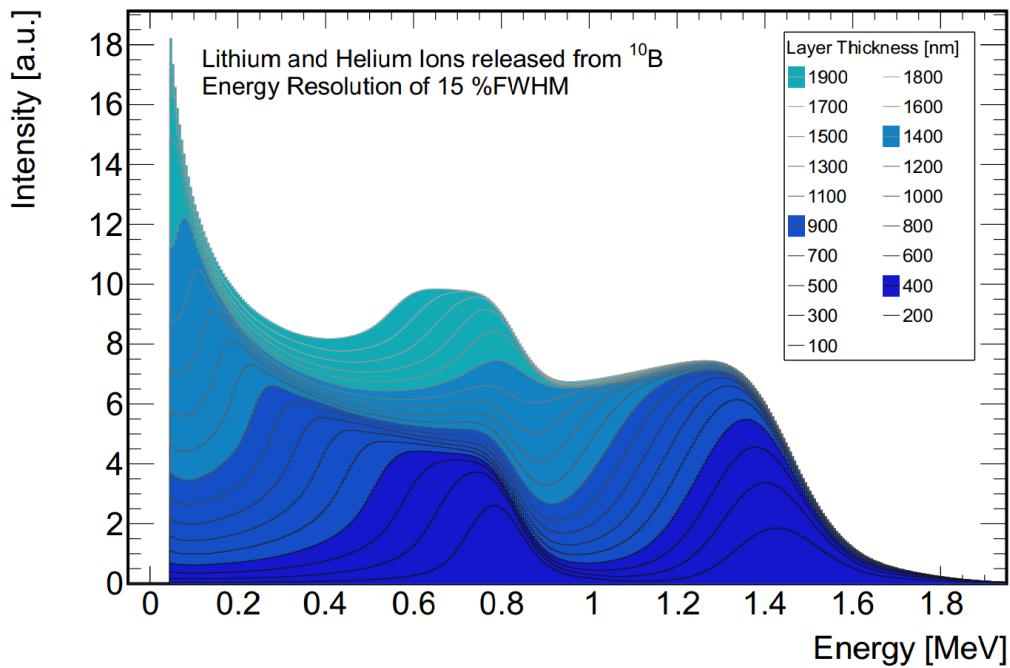
(a) Li from boron-10
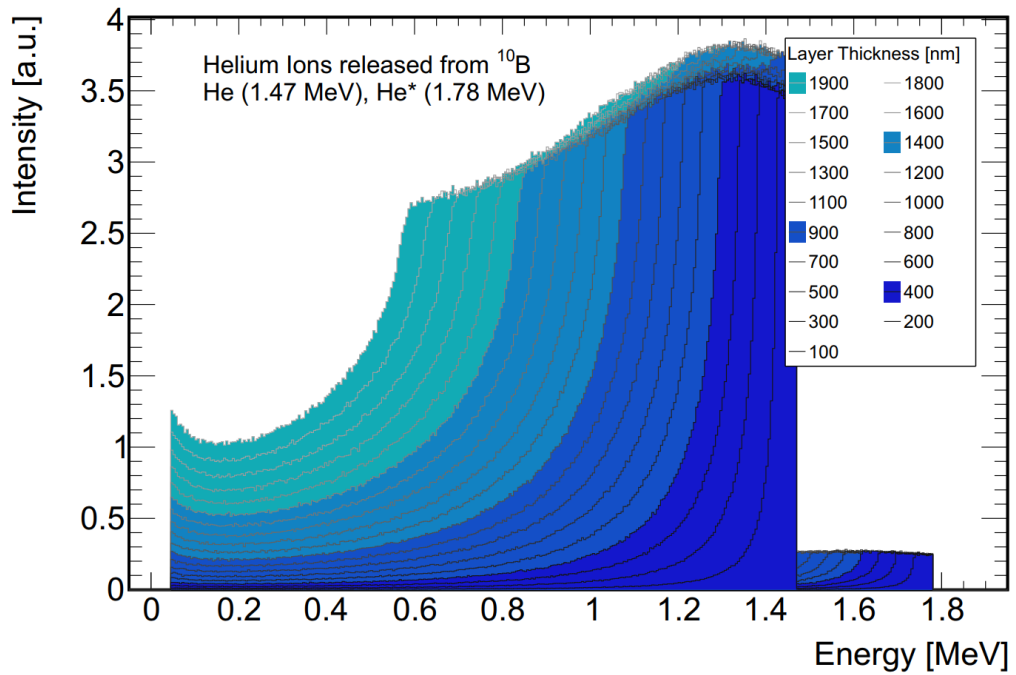
(b) He from boron-10

(c) Li and He from boron-10

(d) Li and He with 15% FWHM resolution

Figure 2.1: Spectra for different thicknesses of boron-10 layers. The spectra show the energy distribution for the different reaction products of a neutron interacting with boron-10 when exiting the boron-10 layer. The layer thickness varies from 100 nm to 1 900 nm. They are color coded in groups of 500 nm. The spectra are separated by different particles: Lithium (a), Helium (b) and both (c). Additionally the combined spectra convoluted with an energy resolution of 15% is depicted (d). [9]
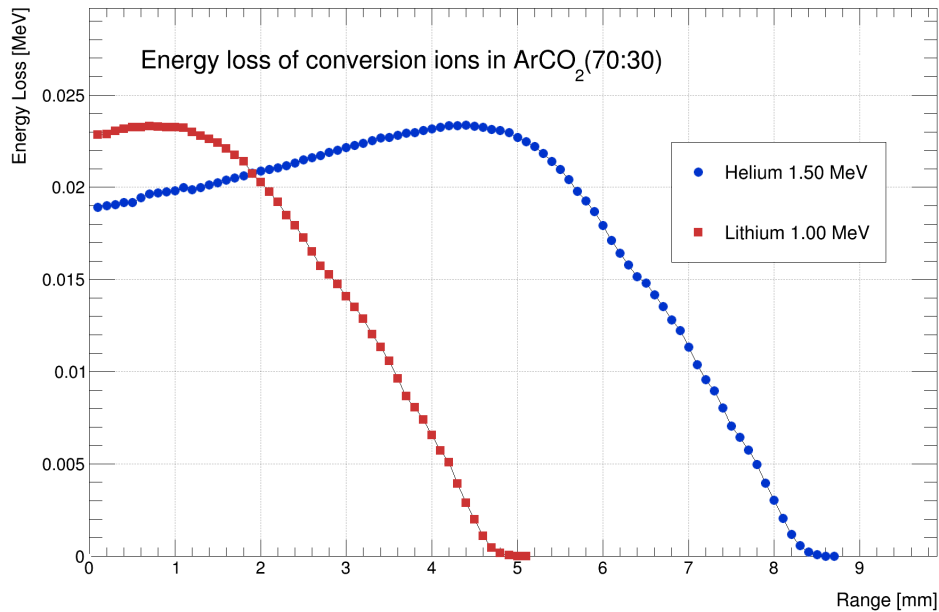
Figure 2.2: Energy loss of neutron conversion products in Ar CO$_2$. For lower energies the curves get shifted to the left. [10]

used as neutron sources. In addition to spontaneous fission there is also the neutron-induced fission, which needs a neutron to interact with the nucleus in order to induce fission. Typically, if one subtracts the neutrons needed for neutron induced fission, one fission process effectively yields about one neutron per reaction. An element that can be used as a fission source is uranium (U^{235}) for example. The typical energy one fission neutron has is in the order of 2 MeV with a broad spectrum [11].

An other method to obtain free neutrons is via radioisotopes. The working principle of radioisotopes is, that one uses an element which can absorb alpha particles and then emit neutrons. A prominent example for such an element is beryllium (Be^9). If beryllium absorbs an alpha particle it will decay to carbon and an additional neutron.

$$\text{Be}^9 + \alpha \rightarrow \text{C}^{12} + \text{n} + 5.704\,\text{MeV}$$
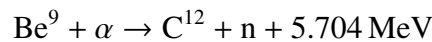
For this reaction a source of alpha particles is needed, but that is rather simple as there are many alpha radiators. Typical elements that are mixed with beryllium are radon (Ra^{226}) and americium (Am^{241}). The sources are then labeled according to the contents, like radon-beryllium or americium-beryllium.

It is also possible to have nuclear reactions with other particles, like deuterons. The reaction a deuteron typically undergoes is with tritium. This is then called fusion and during this reaction the deuteron and tritium are fused to helium and a neutron.

$$\text{H}^3 + \text{H}^2 \rightarrow \text{He}^4 + \text{n} + 17.588\,\text{MeV}$$
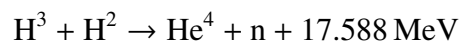
Also there is a charged method called spallation. The spallation method needs a particle accelerator in order to shoot accelerated particles at a target and release neutrons due to the impact. The advantage of a spallation source is that the production of neutrons can be precisely controlled, as the particle beam can be precisely controlled. It is possible to create short neutron pulses by shooting short bunches of particles on the target. The energy of the neutrons can be varied by varying the energy of the incoming particle beam and most importantly the intensity of such a neutron source is very high, as one reaction produces lots of neutrons per incoming particle. Typical particles used for acceleration are protons, but also deuterons are an alternative. All those sources provide high energetic neutrons and they have to be decelerate in order to use them for nuclear reactions that require thermal neutrons. This is done via elastic scattering with light elements, in order to have a large energy loss. This process is called moderation and will be discussed in the next chapter.

2.1.5 Moderation

As the neutrons that are emitted by neutron sources typically do not have energies that are beneficial for detection via conversion it is necessary to slow them down. The process of slowing down the neutrons is called moderation. The principle is relatively easy, as it only relies on elastic collisions and the energy loss that comes along with the collision. At energies of several MeV the collision of a neutron with a nucleus can be considered non-relativistically and simple conservation laws apply. The calculations follow [12] closely.
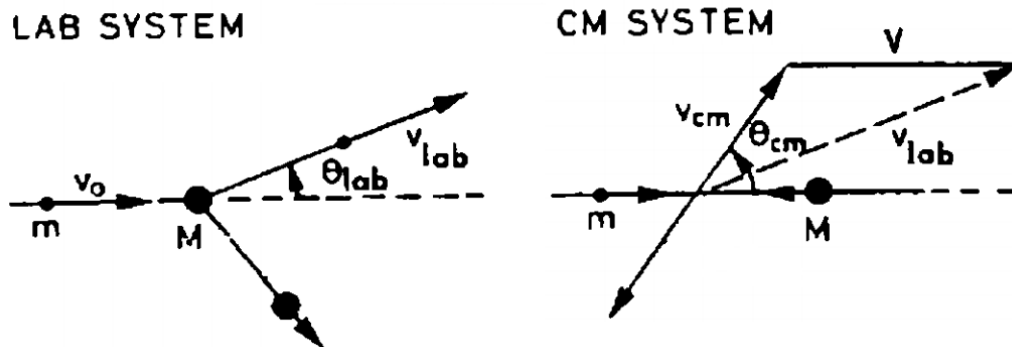

Figure 2.3: Laboratory system and center of mass system for an elastic collision of a neutron with a nucleus of mass M. [12]

As the problem can be treated nonrelativistically one can consider a collision of a neutron with a nucleus in the lab frame (see figure 2.3). The velocity of the neutron shall be v_0 and the rest mass of the nucleus M. Furthermore one can work with mass units of the neutron, which means that $m_n = 1$ and therefore $M = A$, where A is the atomic mass number of the nucleus, as this simplifies all calculations. If one now transforms to the center of mass system the velocity of the neutron is

$$v_{\text{cm}} = \frac{A}{A+1}v_0 \tag{2.1}$$

and the velocity of the nucleus is

$$V = \frac{1}{A+1} v_0. \tag{2.2}$$

After the collision the neutron changes the direction, but retains the velocity in the center of mass system (see figure 2.3). Therefore one can calculate the velocity of the neutron in the lab system by

$$(v_{\text{lab}})^2 = (v_{\text{cm}})^2 + V^2 - 2v_{\text{cm}}V \cos(\pi - \theta_{\text{cm}}) \tag{2.3}$$

where θ_{cm} is the center of mass scattering angle. Now one can substitute equation 2.1 and 2.2 into equation 2.3 and obtain

$$(v_{\text{lab}})^2 = \left(\frac{A}{A+1}\right)^2 v_0^2 + \left(\frac{1}{A+1}\right)^2 v_0^2 - 2\frac{A}{(A+1)^2} v_0^2 \cos(\pi - \theta_{\text{cm}}). \tag{2.4}$$

Using equation 2.4 one can calculate the energy of the neutron after the collision, with $E = \frac{1}{2}mv^2$.

$$\frac{E}{E_0} = \left(\frac{v_{\text{lab}}}{v_0}\right)^2 = \frac{A^2 + 1 + 2A \cos(\theta_{\text{cm}})}{(A+1)^2} \tag{2.5}$$

With equation 2.5 one can see that the energy of the scattered neutron is limited by

$$\left(\frac{A-1}{A+1}\right) E_0 < E < E_0, \tag{2.6}$$

where the limits correspond to the scattering with $\cos\theta_{\text{cm}} = \pm 1$.

By equation 2.6 one can see that the scattering on light nuclei is much more efficient, as it can transfer more energy to the nucleus. This is also why one uses hydrogenous materials for the moderation of neutrons such as water or, like in the case of this thesis, Polyethylene $(C_2H_4)_n$.

In order to determine the average number of collisions one neutron has to undergo to reach a specific energy one can use the logarithmic change in energy

$$u = \ln E_0 - \ln E = \ln \frac{E_0}{E} \tag{2.7}$$

where E_0 is the initial energy and E is the final energy. Form equation 2.5 one can see that after one collision at an an angle θ, u is given by

$$u(\theta) = \ln \frac{(A+1)^2}{A^2 + 1 + 2A \cos\theta} \tag{2.8}$$

Now one can calculate the average $u(\theta)$ by integrating over all directions and dividing by 4π.

This yields the average logarithmic energy loss ξ.

$$\xi = \langle u(\theta) \rangle = \int u(\theta) \frac{d\Omega}{4\pi} = \frac{1}{2} \int \ln \frac{(A+1)^2}{A^2 + 1 + 2A \cos \theta} d(\cos \theta)$$
$$\xi = 1 + \frac{(A-1)^2}{2A} \ln \frac{A-1}{A+1} \tag{2.9}$$

This leads to an interesting fact, that the average logarithmic energy loss after one collision is constant and independent of the initial energy. If one now wants to calculate the average number of collisions for a neutron to slow down from an energy E_0 to an energy E, it simplifies to

$$n = \frac{u}{\xi} = \frac{1}{\xi} \ln \frac{E_0}{E}. \tag{2.10}$$

An example for such a calculation would be carbon as a moderator ($\xi = 0.158$). So that for a neutron of $1\,\text{MeV}$ energy slowing it to thermal energies of $25\,\text{meV}$ it would need $(1/0.158) \ln(1\,\text{MeV}/25\,\text{meV}) \approx 111$ collisions. Instead hydrogen, with $\xi = 1$, needs only 17.5 collisions. So here one sees the effect of light nuclei on the effectiveness of moderation.

2.2 Physics of charged particles in matter

If a neutron is converted to charged particles they have to be detected. This is done by detecting the charge generated by the particles when they traverse the detector. The charge is set free due to the energy loss of the traversing particle. This chapter will explain the basic principle of charged particles interacting with matter, detection of the generated charge and the signal generation.

2.2.1 Ionization and ionization mechanisms

In order to detect a particle, it has to interact with matter. A charged particle traversing matter can interact in several ways. It can for example collide with a shell electron of an atom in the matter. If the energy transfer is higher than the binding energy, the atom will be ionized. This will happen multiple times along the path of the charged particle, but is a statistical process and thus not always the same amount of electrons will be produced. If one of the primary electrons, which are produced by the traversing charged particle, has a high energy and is capable of ionizing more gas atoms it is called a delta electron and leaves a most likely perpendicular track to the initial track if the charged particle. The creation of a delta electron is mostly relevant for high energy particles, thus not that relevant for the energy ranges in this thesis.
All energy loss is summarized by a differential formula, namely the Bethe-Bloch formula [13].

$$-\left\langle \frac{dE}{dx} \right\rangle = \frac{4\pi}{(4\pi\epsilon)^2} \frac{Z^2 e^4 n_e}{m_e c^2 \beta^2} \left(\frac{1}{2} \ln \frac{2 m_e c^2 \beta^2 \gamma^2 T_{max}}{I^2} - \beta^2 - \frac{\delta}{2} \right) \tag{2.11}$$

Here Z is the charge of the traversing particle, n_e is the electron density of the material, m_e is

the mass of the electron, β is the velocity of the traversing particle, γ is the relativistic factor, T_{max} is the maximal kinetic energy transmitted to one electron in a single collision, I is the mean excitation energy, which characterizes the material and δ is a density correction term, that describes screening effects. The Bethe-Bloch formula shows, that the mean energy loss depends on the velocity of the particle and the material it traverses, but not the mass of the particle itself. The shape of the Bethe-Bloch formula is as follows and can be seen in figure 2.4. For low energies the energy loss decreases with $1/\beta^2$ and reaches a minimum near $\beta\gamma \approx 3-4$. Particles with a $\beta\gamma$ at or above that minimum are called minimum ionizing particles (MIP). The energy loss of minimum ionizing particles is about $2\,\mathrm{MeV\,cm^2\,g^{-1}}$ and almost independent of the material, except for very light materials. For higher energies the energy loss increases logarithmically, but due to the density corrections the increase saturates. For very low energies or very high energies the Bethe-Bloch-Formula is not valid anymore, but it covers most of the relevant energy values for particle physics.
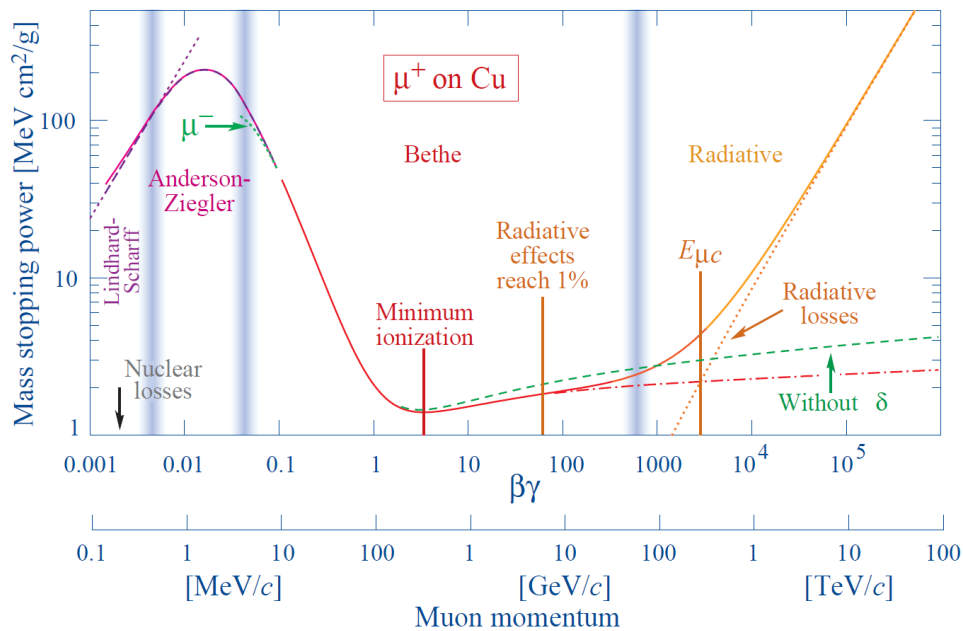

Figure 2.4: The energy loss of a charged particle, or mass stopping power, in matter. Here a muon in copper is taken as an example. The central part of the curve depicts the shape of the Bethe-Bloch Formula. [5]

In the Bethe-Bloch formula all mechanisms of losing energy are summarized, but in order to detect a traversing particle one has to generate a charge cloud. There are some different mechanisms to generate electrons and ions by collisions. The two mechanisms to be distinguished are primary and secondary ionization. Primary ionization occurs, if the incident charged particle directly interacts with an atom and produces one or more electrons.

Secondary ionization is not directly created by the incident charged particle. For secondary ionization one has to distinguish further, as it can happen instantaneous or also retarded. The secondary ionization that happens instantaneous is typically created by interaction with charged particles created with primary ionization. The charged particles can interact with the atoms the

same way as the incident charged particle does. For retarded secondary ionization the incident charged particle typically only excites the atom or molecule it collides with instead of ionizing it. The excited atom or molecule can then interact with other atoms or molecules and yield electrons. In order for an excited atom or molecule to produce electrons it has to interact with an other atom or molecule with lower ionization threshold or form a bound state. These effects are known as Penning effect or Jesse effect.

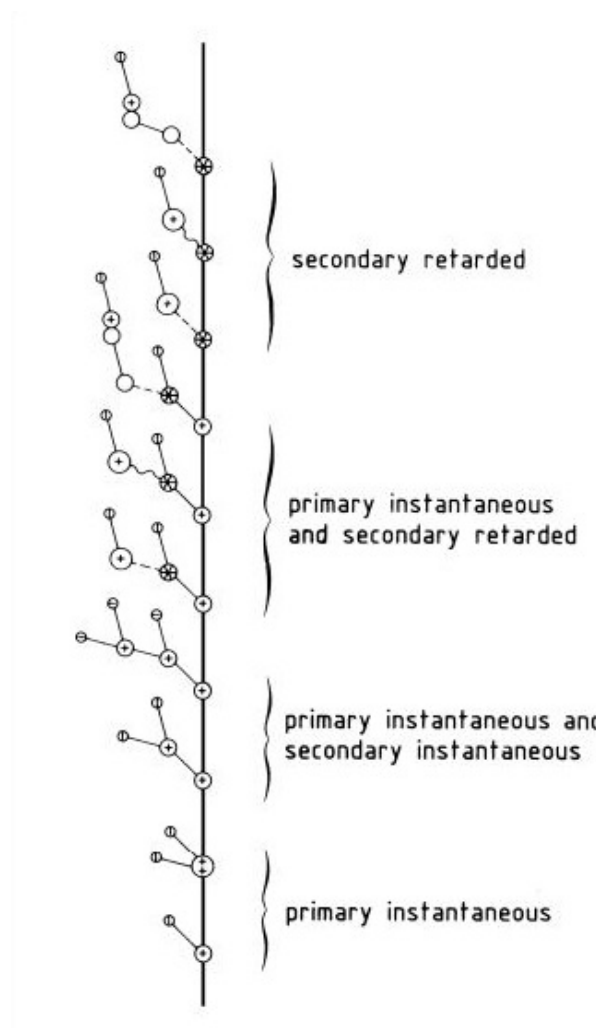A depiction of all those processes can be seen in figure 2.5.

Figure 2.5: Several ionization mechanisms. Primary ionization is directly created by the incident charged particle, whereas secondary ionization is created by other processes for example by excited atoms or molecules. [14]

2.2.2 Drift of electrons in gas

In order to understand the drift of electrons in a gas, one has to consider the motion of a charged particle in the presence of an electric and magnetic field $\vec{E}$ and $\vec{B}$ (Langevin equation).

$$m\frac{\mathrm{d}\vec{u}}{\mathrm{d}t} = e\vec{E} + e\left[\vec{u}\times\vec{B}\right] - K\vec{u} \tag{2.12}$$

Here, m and e are mass and charge of the electron traversing the gas, $\vec{u}$ is its velocity and K describes the friction which is caused by collisions with gas molecules. Moreover, one can define a characteristic time

$$\tau = \frac{m}{K}. \tag{2.13}$$

For $t \gg \tau$, one can assume that $\vec{u}$ is constant and the solution of equation 2.12 becomes

$$\vec{u} = \frac{e\tau|\vec{E}|}{m}\frac{1}{1+\omega^2\tau^2}\left\{\hat{\vec{E}} + \omega\tau\left[\hat{\vec{E}}\times\hat{\vec{B}}\right] + \omega^2\tau^2\left(\hat{\vec{E}}\cdot\hat{\vec{B}}\right)\hat{\vec{B}}\right\}, \tag{2.14}$$

where $\hat{\vec{E}}$ and $\hat{\vec{B}}$ are the unit vectors of the fields $\vec{E}$ and $\vec{B}$. The cyclotron frequency ω is defined as

$$\omega = \frac{e}{m}|\vec{B}|.$$

Here one can see, that the direction of the drift is characterized by the dimensionless parameter $\omega\tau$. For no magnetic field ($\omega\tau = 0$) the drift is along the direction of the electric field $\vec{E}$ and one can define the mobility as the proportionality parameter between the drift velocity $\vec{u}$ and the electric field $\vec{E}$.

$$\mu = \frac{e\tau}{m} \tag{2.15}$$

For large $\omega\tau$ and not perpendicular electric and magnetic fields the drift direction mainly points in the direction of the magnetic field $\vec{B}$. Where as for large $\omega\tau$ and perpendicular fields ($\vec{E}\cdot\vec{B} = 0$), the drift direction is mainly along $\vec{E}\times\vec{B}$ direction. It follows that for time independent and homogeneous fields the drift velocity will be constant and the traversed distance can be calculated by $s = ut$.

2.2.3 Diffusion

Besides the drift of electrons, also diffusion plays an important role in the transport of electrons. As the electrons scatter with the gas atoms they get deflected from their path, which leads to a broadening of the charge cloud transversal to the direction of movement. Thus the total electron current density $\vec{J}$ consists of two parts, namely the part proportional to the drift and one part proportional to the diffusion.

$$\vec{J} = n\vec{u} - D\nabla n$$

Here n is the electron density and D is the diffusion coefficient. I can be shown, if one assumes

that the current is conserved, that the solution is

$$n(t) = \left(\frac{1}{\sqrt{4\pi Dt}}\right)^3 \exp\left(\frac{-r(t)^2}{4Dt}\right),$$

if the charge cloud moves along the z- axis with a velocity u, so that $r(t)^2 = x^2 + y^2 + (z - ut)^2$. With this one can conclude that the width of the charge cloud after a time t is given by

$$\sigma_{x,y} = \sqrt{2Dt}.$$

The diffusion coefficient can also be related to the microscopic quantities of the electron

$$D = \frac{2}{3}\frac{\epsilon}{m_e}\tau,$$

where ϵ is the electron energy and τ is the characteristic time, as derived in equation 2.13. As the electrons are in a thermal equilibrium with the gas, the energy of the electrons an be expressed as $\epsilon = 3/2kT$. The time can be expressed as $t = L/u$ with $u = \mu E$ and L the drift distance, if the drift is along the electric field. One can use equation 2.15 to eliminate the mobility μ to get the following equation for the width of the charge cloud.

$$\sigma_{x,y} = \sqrt{2\frac{kT}{eE}L}$$

Besides constants only the temperature, electric field and drift distance influence the diffusion. Thus one can see that the diffusion is proportional to $\sqrt{L}$ and the proportionality constant is called the transverse diffusion coefficient $D_T = \sqrt{2kT/(eE)}$. In case of a magnetic field parallel to the drift direction the track of the electrons is bent, as they follow a helix pattern rather than a straight line, thus the transverse diffusion is reduced:

$$\frac{D_T(\omega)}{D_T(\omega = 0)} = \frac{1}{1 + \omega^2\tau^2}$$

Also the diffusion in longitudinal direction can be described by $\sigma_z = D_L\sqrt{z}$ with D_L the longitudinal diffusion coefficient. In general D_T and D_L are different, because of the dependence on the mean time between collisions, which is higher in longitudinal direction. D_L will also not be influenced by a magnetic field parallel to the drift direction.

2.2.4 Gas amplification

As the primary electrons created by the incident ionizing particle are hard to detect one amplifies the signal by applying a strong electric field. In a strong electric field the electrons are accelerated and reach energies in the order of the ionization energy of the gas. Thus they generate secondary electrons by ionizing collisions with the gas atoms. Over a certain distance this leads to an exponential growth in the number of electrons. This can be described with the following

differential equation.

$$\frac{\mathrm{d}N}{\mathrm{d}x} = \alpha N$$

Here N is the number of electrons and α is the first Townsend coefficient, which can be expressed by the mean free path of an electron as $\alpha = 1/\lambda$ with λ being the mean free path. The solution to this differential equation, assuming a constant α, which is valid for a constant electric field, is a single exponential. As it is more useful to know the relative increase instead of the absolute number of electrons, one defines the gain G as

$$G = \frac{N(x)}{N_0} = \exp(\alpha x)$$

As the collisions in the gas follow a statistically distributed process, the gain G is a mean value. Its distribution can be described by a Polya function. The first Townsend coefficient, or correspondingly the mean free path, is dependent on the applied electric field and also the gas mixture. Thus the Gain varies with the applied electric field and the choice of the gas mixture.

2.2.5 Signal induction

To understand the signal generated by a detector, one has to understand how that signal is produced by the detected charge. The signal does not appear, when the charge reaches the detection plane, but is already induced prior to that.

When a charge q drifts towards an electrode, there will be an induced charge on that electrode. The main problem is calculating the charge on one electrode if the setup has multiple electrodes. The solution for this problem can be obtained by solving the Poisson equation with a moving charge, but that is rather complicated. An easier method is the usage of a mirror charge. The charge q drifting towards the electrode will induce a mirror charge $-q$ on the electrode. This yields no current by it self, but if the electrode is separated, the induced on each segment will change with time and thus yield a current. The charge q_n induced on the nth pad of the electrode will depend on the position $\vec{x}$ of the charge q. In total, when summing over all pads, it yields the induced charge $-q$.

$$Q_{\mathrm{total}}^{\mathrm{ind}} = \sum_n q_n = -q$$

If the charge moves then the position will change with time and also the induced charge will change with time, thus yield a current.

$$I_n(t) = -\frac{\mathrm{d}}{\mathrm{d}t} q_n(\vec{x}(t))$$

In order to determine the total charge induced on a segment of the electrode at a certain time T one has to integrate the current.

$$Q_n^{\mathrm{ind}}(T) = \int_0^T I_n(t)\mathrm{d}t$$

At the end of the drift time, when the charge q arrives at segment m of the electrode, the total

charge on the segment *m* is *q*, whereas the integral for all other segments yields zero. This means, that the charges induced in the segments will change until the charge has arrived at the readout.

In a detector usually not only one charge induces a signal, but as there are multiple charges (ions and electrons), the induction of the current stops when all charges reach an electrode. Usually first the electrons reach an electrode, as they move much faster, compared to the ions. This will induce a very short, but also high signal until they reach the readout. When the ions reach the electrode the signal induction stops.

As it is quite tedious to compute the induced signal for each drifting charge with the mirror charge method, an easier method was developed by Ramo [15] and Shockley [16]. The Ramo-Shockley Theorem simplifies this by using a weighting field and the drift trajectory to calculate the induced current for each segment. The main advantage is, that the weighting field has only to be calculated once for each segment. In order to calculate the induced current on an electrode *n* from the drifting charge *q* with the trajectory $\vec{x}(t)$ one can use

$$I_n(t) = -q\vec{E}_n(\vec{x}(t)) \cdot \frac{\mathrm{d}\vec{x}(t)}{\mathrm{d}t}.$$

Here $\vec{E}_n(\vec{x})$ is the weighting field of the electrode *n*, which has only to be calculated once. It can be determined by calculating the electric field when electrode *n* is set to 1 V and all other electrodes are set to 0 V.

CHAPTER **3**

Technical background

3.1 European spallation source

The European spallation source (ESS) [17] will be a large user facility where neutron beams will be provided. The neutron beams can be used to investigate a lot of questions, like molecular building blocks of matter [18]. The ESS will have the worlds most powerful pulsed neutron source, as it will be 100 times brighter than already existing neutron sources [19]. It is being built in Lund, which is in Sweden, and the construction started in 2014. According to the construction plan the first neutrons will be produced in 2019 and it should be fully operational by 2025 meeting its design specifications. It will provide 22 research instruments to investigate properties of materials with neutrons.

The name already gives the neutron production mechanism away, as it will be done via spallation. For the spallation a helium cooled tungsten wheel target will be used. Protons derived from hydrogen gas will be accelerated in a linear accelerator and the collide with the target. Due to the collision of the high energy protons with the tungsten target high energy neutrons will be produced. The neutrons will be redirected to the experimental areas and can be used for experiments there. As mostly thermal neutrons are needed for experiments the neutrons will be moderated from approximately ten percent of the speed of light to the speed of sound. The moderation and guidance to the experimental area will be done with reflectors and moderators. This technique will provide thermal neutrons in intense pulses for the experiments.

The neutrons will be generated in pulses with a pulse length of 2.86 ms and a repetition frequency of 14 Hz. In order to generate those pulses the linear accelerator will accelerate protons over a distance of about 490 m to 2.5 GeV and collide them with the tungsten target. To obtain the neutron flux needed the accelerator beam power has to be 5 MW. This will lead to a peak neutron flux of 40×10^{15} cm^{-2} s^{-1} and an average flux of 1.6×10^{15} cm^{-2} s^{-1}. If one compares that with already existing machines it is way better. The J-PARC facility has a peak flux of 20×10^{15} cm^{-2} s^{-1}, but only an average flux of 0.1×10^{15} cm^{-2} s^{-1} and the PIK has an average flux of 1.2×10^{15} cm^{-2} s^{-1}, but is not as big and is not operated in pulsed mode as it is a reactor. The accelerator and the tungsten wheel will be cooled with liquid helium and the cooling system will be responsible for the whole ESS machine. Also the neutron scattering instruments and the conventional facilities will be cooled by the integrated cooling system. This keeps the cost and

maintenance low and makes it possible to control the facility all at once and have a machine protection system for the whole facility.

3.2 Gas electron multiplier

The Gas electron multiplier (GEM) [20] was invented by Fabio Sauli in 1997. GEM foils are used to amplify a charge signal inside a gaseous detector. The amplification takes place in holes, that are located in the GEM foil. The avalanche amplification can be a factor of 100 to 1000 for single electrons. If the electrons traverse the hole the avalanche will take place, but they can also hit the surface of the GEM and thus be absorbed. Additionally parts of the electrons created by the avalanche can also be absorbed by the lower side of the GEM if they are generated close to the edges of the holes. Thus only a percentage of all generated electrons leave the avalanche area. If one multiplies the real gain of a GEM foil with its efficiency one obtains the effective gain, which is in the order of 100. The efficiency has to be broken into two parts. The first part is the absorption on the upper side of the GEM, where the incoming electrons get lost and the second part is on the lower part of the GEM, where parts of the avalanche can be absorbed. The avalanche effect of a GEM foil can be used multiple times to obtain a measurable output signal. GEM foils are made of kapton and copper in layers. Usually there is a 50 µm thick kapton layer coated with copper on both sides. In them GEM foil there are holes in a regular, usually hexagonal, pattern which can be seen in figure 3.1(a). Typical holes have an inner diameter of 50 µm and an outer diameter of 70 µm. The closest distance between two holes is called the pitch and typically is about 140 µm. All these dimensions can also be changed, as the GEM foils are fabricated on demand for the user. By applying a voltage across the copper layers one creates a strong electric field inside the holes. Due to the very high electric field an avalanche occurs inside the holes and leads to electron multiplication. The electric field inside the holes of a GEM foil can be seen in figure 3.1(b).

3.3 Time Projection Chamber

The Time Projection Chamber (TPC) [21] was first introduced by David R. Nygren in 1976. It is made of a gas filled volume with a usually central cathode which divides the gas volume. The cathode is set at a high potential with the anode at typically ground. This leads to an electric field between the cathode and anode where the electrons and ions created by the traversing particle drift. For the operation of a TPC the electric field between the cathode and anode should be as homogeneous as possible. This is achieved by enclosing the gas volume with a field cage. The field cage is made to provide a continuous potential drop in order to have no field distortions inside the gas volume. Additionally to the gas volume one needs timing information, when the particle, which should be detected, traverses the TPC. This can be either done, by exactly knowing when the particle will be created, like in accelerator experiments or by having a trigger. The trigger is usually an other very fast detector which the particle has to traverse first in order to reach the gas volume of the TPC. The traversing particle will then ionize the gas along its trajectory and the released electrons will drift towards the anode. At the anode the electrons

(a) Microscopic picture of a GEM foil.

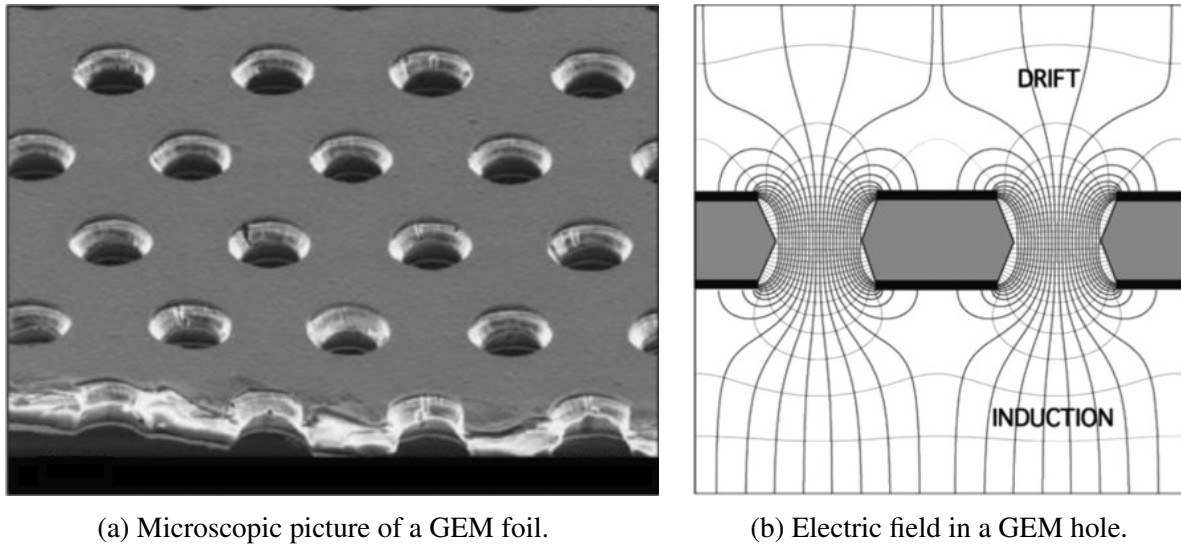(b) Electric field in a GEM hole.

Figure 3.1: Microscopic picture of a GEM foil and the corresponding electric field in the GEM holes. In the microscopic picture one can see the typical diameter and pitch of the holes of 70 μm and 140 μm respectively. [20]

will be detected, usually with an avalanche process in order to generate a detectable signal. The anode is typically made out of a highly granular readout, as the full three dimensional track shall be reconstructed. The first two dimensions are given by the detection at the anode and the third dimension is calculated with the timing information. If one wants to measure additional properties of the particle traversing one can apply a magnetic field in order to bent the track of the particle. By measuring the curvature one can determine the momentum of the traversing particle. In order to calculate the third coordinate and the momentum one has to know the properties of the detection gas very well in order to know the drift velocity of the electrons.

3.4 GridPix

The GridPix [22] is a pixelised readout chip consisting of a Timepix chip and an integrated gas amplification structure (InGrid) [23]. The integrated gas amplification structure is put on top of the Timepix chip with a photo-lithographic post-processing procedure. The process used to create the integrated gas amplification structure will be explained in section 3.4.3. The GridPix used for measurements has a protection layer made of silicon-nitrite of 8 μm thickness.

3.4.1 Timepix

The Timepix chip [24] is a pixelised readout chip. It is an evolution from the Medipix2 [25] chip and is designed for single photon counting. The size of the Timepix chip is 14 mm × 16 mm, where 14 mm × 14 mm is the active area. It has 256 × 256 pixels with a pitch of 55 μm. The area not equipped with pixels is used to connect the chip to its carrier board via bonding wires.

The electronics of one pixel can be seen in figure 3.2. The charge is collected by an octagonal pixel anode with a width of 20 μm after amplification and then compared to a threshold. If it exceeds the threshold the pixel will, depending on the operation mode, increment a 14bit register. The operation mode and threshold can be set with an 8 bit Pixel Configuration Register (PCR) for the pixel operation mode and a 4 bit register for the threshold adjustment. The Pixel Configuration Register (PCR) contains 4 bits for the threshold equalization for the pixel, 2 bits for the operation mode (P0 and P1), 1 bit for masking (Mask) and 1 bit for enabling test pulse input (Testbit). The 14 bit Register functions as the counter of the pixel when it is active. It has a dynamic range of 11810 counts, which is less than 14 bit because some bits are reserved for other information.

The operation modes of the pixel, depending on P0 and P1, are as follows:

1. Event counting mode (P0 = 0 and P1 = 0): Each event that exceeds the threshold increments the counter by 1.

2. Time Over Threshold (TOT) mode (P0 = 1 and P1 = 0): The counter is incremented as long as the signal exceeds the threshold.

3. Time Of Arrival (TOA) mode (P0 = 1 and P1 = 1): The counter is incremented from the first moment when the signal exceeded the threshold until the shutter is closed.

The timing of the pixel can be seen in figure 3.3. There one also sees one drawback of the Timepix chip, that it needs a shutter signal. Only when the shutter signal is a logical low the pixel is able to detect something. Thus one needs to open the shutter before the charge arrives at the pixel. Additionally one pixel in TOT or TOA mode can not separate multiple hits, as in the TOT mode it integrates all the charge arriving on the pixel during the time the shutter is open. In case of the TOA measurement it yields the timing information when the pixel was first hit and is not sensitive to later hits. Another downside is that one pixel can be set to either TOT or TOA mode and is not able to measure both simultaneously. These issues are addressed with the new Timepix3 chip [26], as the new Timepix3 does not need a shutter anymore and is able to handle multi hits correctly.

3.4.2 InGrid

The integrated gas amplification structure or **In**tegrated **Grid** (InGrid) is put onto the Timepix with photo-lithographic post-processing [28]. The details on the processing procedure can be found in section 3.4.3. In picture 3.4 one can see a photo of an InGrid structure. The Timepix with the protection layer can be seen on the bottom. On top there are the tiny pillars holding the aluminum grid. Due to very precise alignment the holes in the grid are located directly above the pixels of the Timepix chip. With a suitable gas gain it is also possible to detect single electrons with this InGrid and Timepix combination.

In order to achieve mechanical stability not the whole Timepix active area is covered with the InGrid structure. The sides of the InGrid are supported by walls instead of pillars to hold the whole InGrid structure. The top side of the walls is also covered with the grid and thereby provide a place to connect the high voltage.
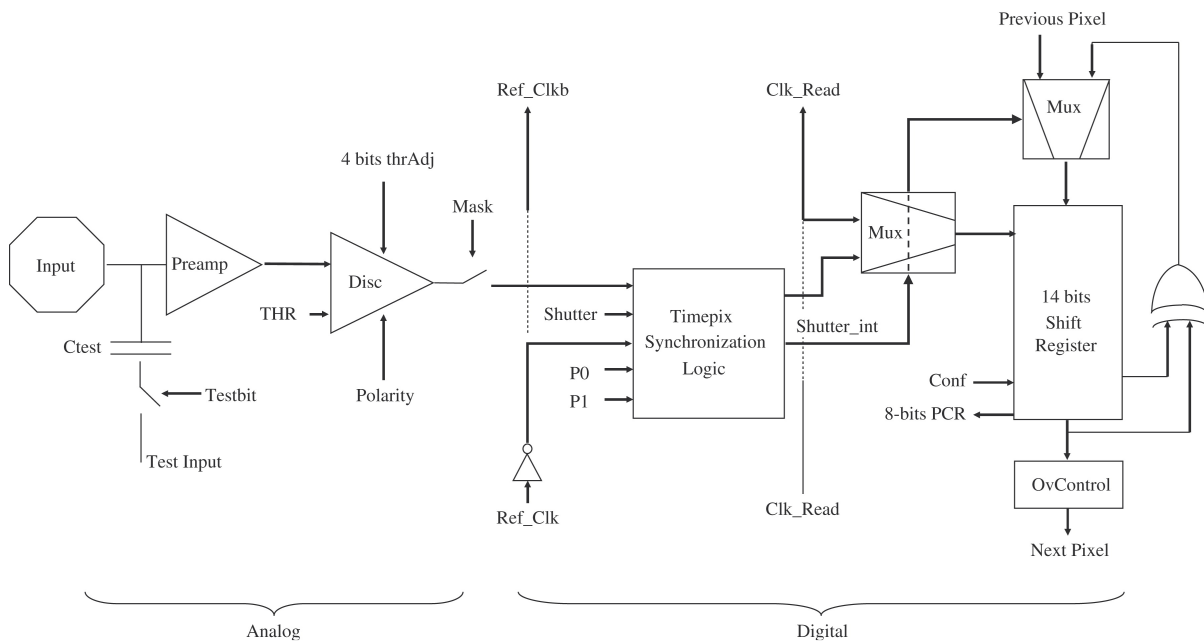
Figure 3.2: The electronics of a single pixel of the Timepix chip. In the analog part, which is depicted on the left, one can see the octagonal readout pad connected to the charge sensitive preamplifier and discriminator. There is also the input for test pulses , which can be injected via a capacitance. The part on the right is the digital part of the pixel. In the digital part the logic is located and also here the pixel operation mode is defined. The bits P0 and P1 can be set to the different operation modes, as described in the text. The register is used for storing the data until the pixel is read out. [24]
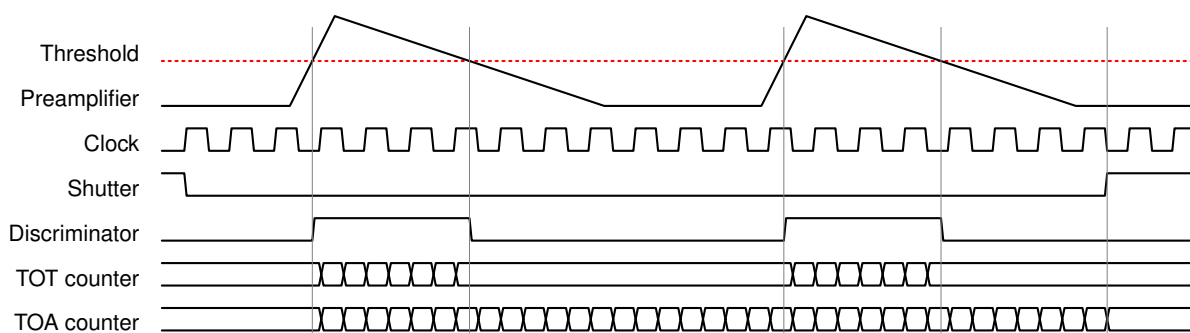
Figure 3.3: The timing of a Timepix pixel can be seen in this figure. The incoming charge signal is amplified by the preamplifier and if it exceeds the threshold it will set the discriminator to high. As long as the discriminator is set to high a pixel set to TOT mode will count. Multiple hits on the pixel will be added together. If the pixel is set to TOA mode it will start counting when the discriminator first goes to high and stop counting when the shutter closes. [27]
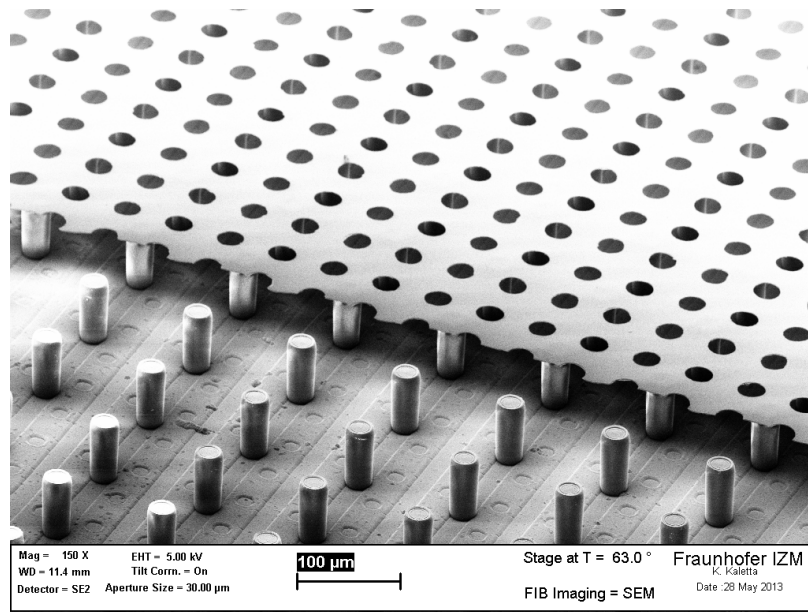
Figure 3.4: Microscopic view of a Timepix chip with an InGrid on top. Parts of the grid were removed to obtain a better visibility. [29]

3.4.3 **Fabrication of an InGird**

Here the fabrication process of an InGrid onto a Timepix will be described. The fabrication steps are described in more detail in [30]. The process is sketched in figure 3.5 and described in the steps below. The enumeration of the steps matches the enumeration in the picture.

1. The start is a bare Timepix chip that will be processed.

2. The first manufacturing step is to add a resistive protection layer made of silicon nitrite onto the Timepix chip. This consist of several sub-steps, as one sub-step can only generate a certain thickness. The number of sub-steps determines the final thickness of the protection layer. Typical values of the thickness lie between $2\,\mu m$ and $8\,\mu m$.

3. Next a negative photoresist (SU-8) is deposited on top via spin coating. The typical thickness of this layer is $50\,\mu m$ and it will be developed to build the supporting structure for the grid.

4. In order to form the supporting structure a mask is placed on top of the photoresist and it is exposed with ultraviolet light. The areas exposed to the light will then stay after cleaning of the photoresist. The structures created in this step are pillars in the active area of the chip and walls at the sides of the chip. The diameter of one pillar is typically $30\,\mu m$ and the pitch between them is $110\,\mu m$ and $165\,\mu m$, as the pillars are placed in between the pixels.

5. Then aluminum is sputtered on top of the photoresist. The aluminum will later form the grid, which is used for gas amplification. The thickness is typically $1\,\mu m$.

6. A mask for the holes in the grid is applied to the top of the aluminum layer with photolitography.

7. The grid holes are then etched into the aluminum layer and the mask for them is removed. The typical hole diameter is 30 μm and they are centered above one pixel each.

8. Lastly the photoresist which was not irradiated with ultraviolet light is cleaned and the structure is complete.
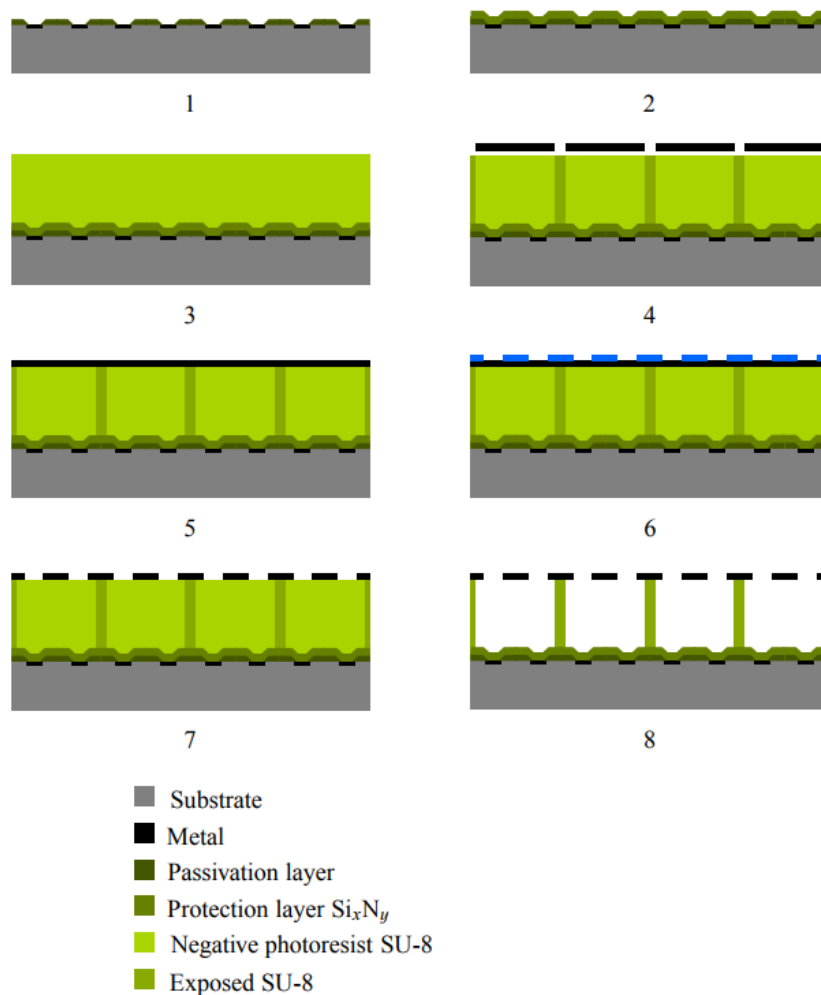

Figure 3.5: Sketch of fabrication steps for manufacturing an InGrid. The steps for the fabrication are explained in chapter 3.4.3. [31]

3.4.4 Octoboard

As the area one GridPix covers is only about $2\,cm^2$, it is useful to use multiple chips. On an Octoboard there are eight chips mounted in a 4×2 array on a carrier board. In picture 3.6 one can see such an Octoboard. The chips are connected with wire bonds to the PCB and the readout is performed in a series. On the back side of the PCB one can see 3 connectors. The outer ones are used for the high voltage connection of the grid above the pixels and the central one is used for communication between the chips and the readout system. The Octoboard can be mounted onto an intermediate board, where the high voltage and the slow control and data connections are located. A picture of an intermediate board can be seen in picture 3.7.
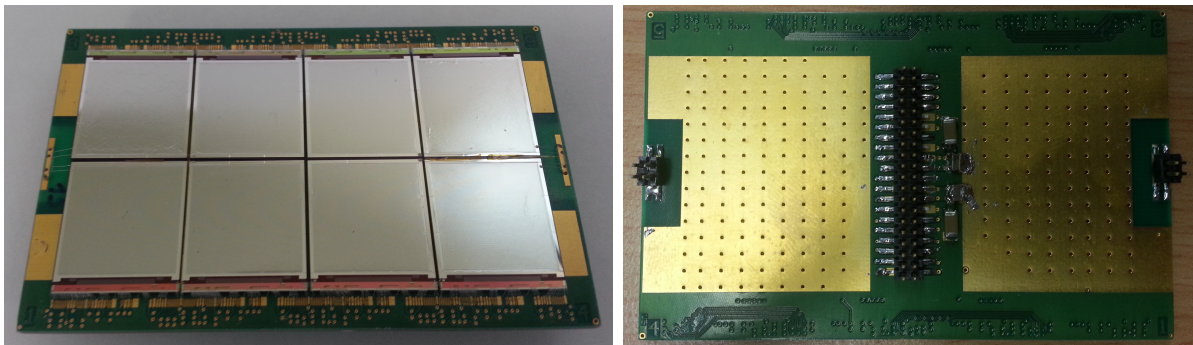
(a) Top view of an Octoboard.   (b) Bottom view of an Octoboard.

Figure 3.6: Depiction of an Octoboard with eight GridPix on top. The top side is the side, where the eight GridPix are mounted and the bottom side in where the connectors to the intermediate board are located. The photo of the bottom side was taken with a dummy with no GridPix mounted, as one can not place the Octoboard on the side where the GridPix are located without damaging it. The Octoboard depicted here is not the Octoboard that was used for the measurements. The Octoboard used for the measurements can be seen in chapter 8.3.

3.5 Readout system

The readout of the Timepix Octoboard is done by a Scalable Readout System (SRS) [32], in order to be able to scale the number of Octoboards to high numbers and instrument bigger areas [33].
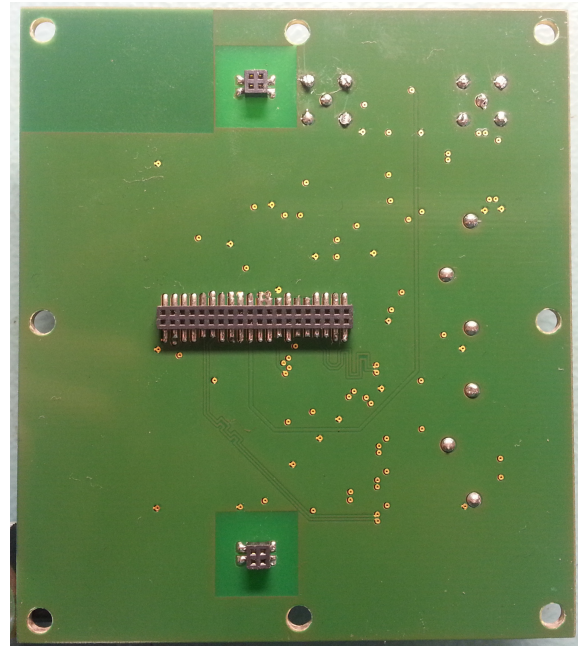
3.5.1 Hardware

The SRS Hardware consists of multiple parts. All of them will be described in this section. The Octoboard, where the GridPix are located is connected to an intermediate board. The intermediate board functions as a connector board for multiple connections to the Octoboard. The picture 3.7 shows the intermediate board and the connections. The two HDMI connectors are used for communication with the readout system. One of them is used for the slow control, the other for the data transfer. The slow control contains all instructions that shall be give to the

Octoboard. It is also possible to disconnect some of the signals, for example the shutter signal, in order to use an external signal, that can be generated by an external trigger. The external shutter signal has to be fed into the upper left LEMO connector and the solder bridge has to be set to the appropriate connection. The other signal that can be fed externally is the test pulse, which is used for calibration of the GridPix. The test pulse is fed into the right LEMO connector. The high voltage has to be connected to the solder pads (see orange cables). The four remaining solder pads are to be used for the power supply of the intermediate board and the Octoboard.
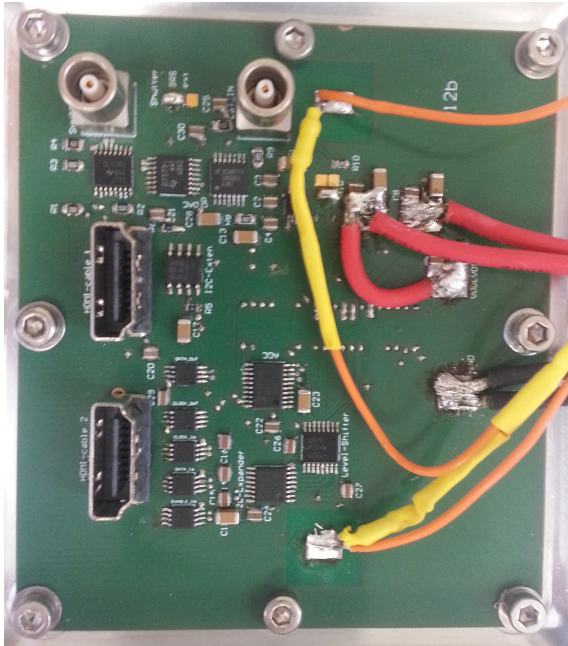
(a) Top view of the intermediate board. (b) Bottom view of the intermediate board.

Figure 3.7: Depiction of the intermediate board that was used for the measurements. The first picture shows the top side, where all electronics and connectors are located. There are also six solder pads for power supply and high voltage connections, which are already connected. The two HDMI connectors are used for the communication with the readout system. The LEMO connectors can be used to feed the shutter and test pulses externally if required. On the bottom side one sees the connectors to the Octoboard, where the central one is used for communication and powering and the outer ones are used for high voltage supply.

Via the HDMI connectors the intermediate board is connected to the so called C-card. The C-card is used as a connector to the front end card (FEC), as the FEC does not support HDMI cables directly. The C-card has five HDMI connectors and two LEMO connectors. The top most HDMI connector, right below the two LEMO connectors, is used for the slow control. The other four are used for data transfer. This means that up to four Octoboards can be connected to one C-card. This requires a different intermediate board though, because it has to support four Octoboards too, as there is only one slow control connector and four data connections. The LEMO connectors are used to feed signals into the FEC. The top most LEMO connector can be used to trigger the readout cycle externally. For the lower one it was planed to give feedback when the readout cycle is finished, but this was unfortunately never implemented into

the firmware.

The front end card (FEC) is used to compute the data that is generated by the Octoboard. A picture of the FEC with a C-card attached can be seen in figure 3.8. The FEC is programmable with a different firmware, depending on the number of chips to be connected. There are two different versions of the firmware, one for a single chip and one for Octoboards. It is also possible to connect multiple FECs with each other in order to establish a communication with more Octoboards. On the FEC the work is done by a field programmable gate array (FPGA) [34]. The FPGA processes the data sent via the HDMI cables and does a first step to shrink the size of the data in the form of zero suppression. It also sends the instructions to the intermediate board via the slow control, depending on the instructions is gets from the controlling computer. Additionally it converts the data into a different format to send it to a computer. The transfer to the computer is done via an Ethernet cable. On the computer the packages sent by the FPGA are collected and interpreted by the so called Timepix Operation Software (TOS).

(a) FEC from left side   (b) FEC from right side
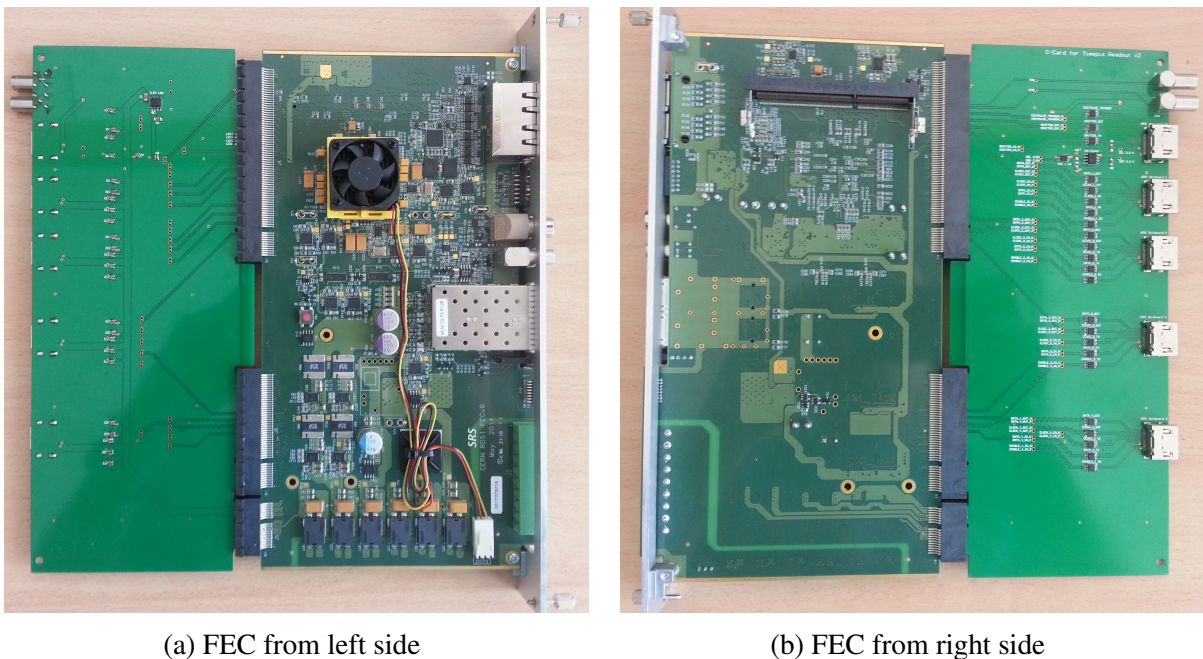
Figure 3.8: The two pictures show the front end card (FEC) and the C-card from both sides. The FEC houses the FPGA which processes all data sent by the chip. The C-card serves as a connector from the HDMI cables to the FEC.

The FEC with the C-card mounted is placed inside a SRS crate. This crate has the power supply for the FEC and serves as a mounting place for several FECs. A picture of a SRS crate with some FECs can be seen in figure 3.9.

3.5.2 Timepix Operation Software

The Timepix Operation Software (TOS) is used to communicate with the FPGA and receive the data from the FPGA. On the FPGA the Timepix Operation Firmware (TOF) [35] is collecting
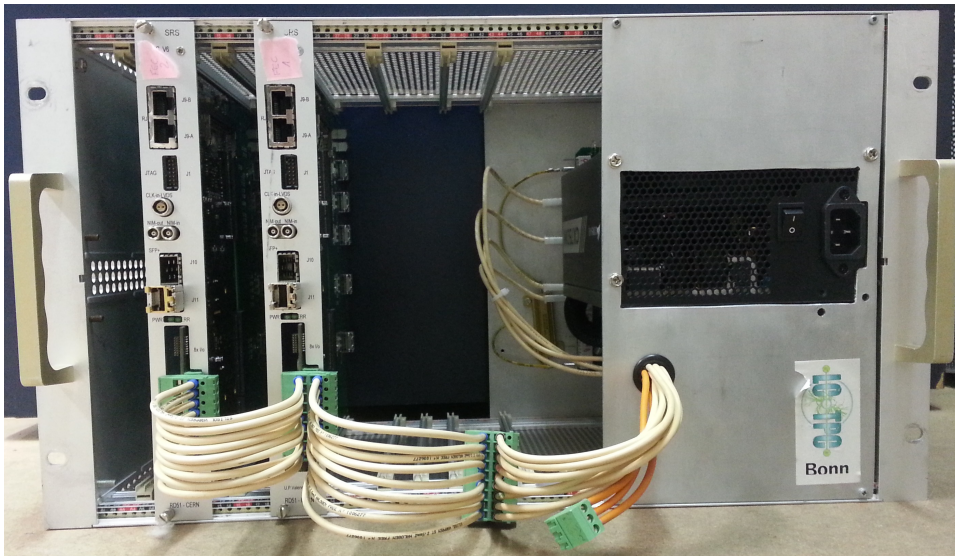
Figure 3.9: A SRS crate with two FECs mounted inside is depicted.

all the data output by the Octoboards. TOS is build as a console program written in C++ and has several functions for configuration and data taking available. Upon starting the software one has to set the operation mode. The user has to tell how many GridPix are connected and how many FECs are used for that. Then the software is able to communicate with all those FECs and also the corresponding chips. It is able to calibrate the chips and do the data taking.

For the calibration there are functions available to equalize the output of the chips and to calibrate the TOT value sent by the chips with test pulses. The calibration typically has to be done only once per chip, if the external conditions do not change. The calibration files then have to be loaded to the chips and the chips are then ready for data taking. The data taking is automated within TOS by asking the user for the data taking mode and then it is possible to let it run continuously and also abort it anytime.

The output by TOS is either zero suppressed or the full matrix read by the chip, depending on the mode the user specified. In case of the zero suppressed data, which is the default case, the data is saved on frame by frame basis into text files. There is one text file created per frame. If the user chose the full matrix readout, TOS will generate one text file per chip per frame, e.g. eight files per frame for one Octoboard.

The Timepix Operation software (TOS) was first developed in Mainz and is now under continuous development and improvement in Bonn by M. Gruber.

BASTARD

4.1 Aim of detector

The boron based multi stage tracking detector (BASTARD) is a neutron detector aimed for high rate capability and also decent spatial resolution. The detector mainly consists out of gas electron multiplier (GEM) foils that are modified in a specific way. The change of the GEM foil compared to the usual GEM foils will be explained in the next section. The BASTARD detector will consist out of several modules that can be stacked in order to obtain a higher detection efficiency, as a single boron layer of 1 μm only detects 5 to 7 percent of all neutrons. Additionally one module already has a decent active area of about $900 \, \text{cm}^2$. The BASTARD detector could for example be used for small angle neutron scattering as it is done in [36].

4.2 Design

The design of one BASTARD module is depicted in figure 4.2. It mainly consists of a GEM foil and the frame for the GEM foil. The frame is also the case of the detector module. When multiple modules are stacked they will be directly put on top of each other. The large holes inside the GEM are used to transfer the detector gas between the different stacked modules, such that only one input and one exit for the gas has to be applied. The input and exit will be on the top or bottom cover of the stack respectively.

The GEM foil is structured, as it can be seen in figure 4.1(a) and 4.1(b). The structure looks quite complicated, but there was no easier way to fulfill the requirements that are imposed on the structure. The structure should be separated in strips and the strips on both sides of the GEM foil should be perpendicular to each other. Additionally the area around the holes in the GEM foil should be regular and not cut by the strip structure. This way the top structure was designed. At first the strips had straight edges, but that lead to a variation of the are around the GEM holes, which should not be the case. Thus the strips had to be designed to have always the same structure around one GEM hole and the result of that can be seen in figure 4.1(a).

The bottom structure was originally intended to have the same pattern as the top structure, but it was not possible, as the holes are a different pattern if one wants to make it perpendicular to

the top structure. The first attempt was to ignore the requirement to have it perpendicular and the top structure was placed on the bottom layer, such that there is an angle of 60° instead of 90°. After longer discussions this concept was discarded, as perpendicular strips are required. This lead to the new design, which had to have a different structure and a different pitch than the top structure. The new structure can be seen in figure 4.1(b). Due to the different pattern of the holes the pitch had to be different on the top and on the bottom. The pitch of the top side is 242.5 µm and the pitch on the bottom side is 280 µm. This leads to different amount of strips on both sides of the (quadratic) GEM foil, but is not problematic if one keeps that in mind during the analysis of the data.

This GEM foil consists of five layers. The layers are alternating copper and kapton layers. The top most layer consists of copper and is constructed like the pattern depicted in figure 4.1(a). Then a kapton layer follows to isolate from the next copper layer. The kapton layer has holes inside exactly on the same positions as the copper layer above. The next, middle, copper layer is constructed like the pattern in figure 4.1(b). The next kapton layer is a solid kapton layer with no structure. Then a solid copper layer without a structure follows. On this copper layer the boron-10 will be coated for the neutron conversion area. For a detailed description of the dimensions of the structures on the copper layers have a look at the corresponding pictures and their caption. This structure will then be mounted inside a frame (see figure 4.2) and stacked on top of each other (see figure 4.3). This way the bottom most copper layer of the module above acts as a cathode for the next layer, thus the structure is easily expandable.

4.3 Working principle

The single module of the BASTARD detector will not work as a single module, as one needs at minimum two of them in order to have a contained gas volume. The upper one works as a cathode for the next one. Additionally the solid copper layer, that is the cathode, has to be coated with boron in order to obtain a surface for neutron conversion. If one neutron converts on that layer the resulting two charged particles will go back to back. One of them will enter the gas volume and thus leave a track. This track will then drift towards the anode layer of the next module. The anode layer is the structured layer of the GEM foil. As the GEM foils have holes an avalanche will form inside them. The formation of the avalanche is accompanied by an induction of a signal on both the top and also the middle layer of the module. Both of these layers are structured with strips perpendicular to each other. This leads to signals that can be used to reconstruct the position of the track in two dimensions. With the information about the track one can reconstruct the point where the track left the boron and thus the neutron interaction point.

The first module for testing is planned to have 10 cm × 10 cm of active area, whereas the final module should have 30 cm × 30 cm of active area. This leads to 412 strips on the top layer and 357 strips on the bottom layer. All of those have to be routed to a connector in order to read the out. Additionally one has to take care of the frame of the detector, which should be secured by screws. The routing should also include a larger safety margin around the screws, as the GEMs will be on high voltage. This routing was also done and an example for that can be seen in figure 4.4. The connectors are planned to fit a board that houses two VMM3 application specific

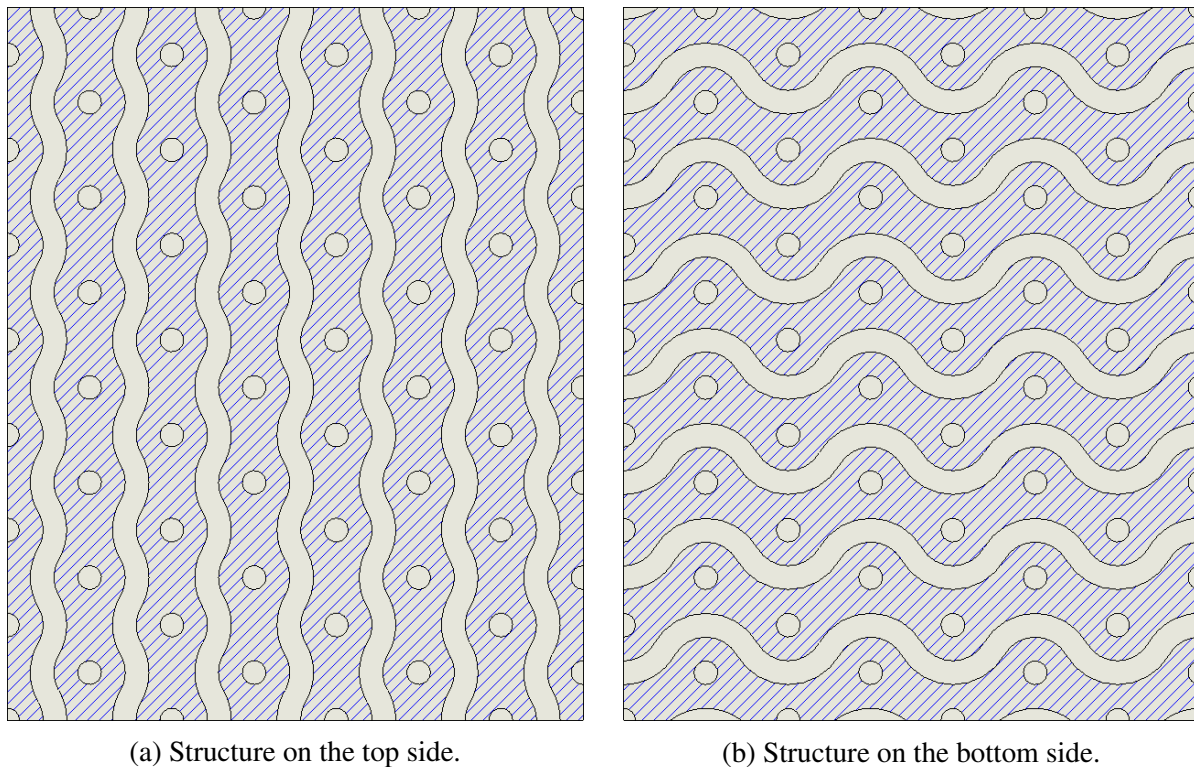(a) Structure on the top side. (b) Structure on the bottom side.

Figure 4.1: Depiction of the copper structure in the layers of the GEM foil. The hatched area is copper and the rest is etched out. The holes are arranged in a hexagonal pattern, which are also etched through the kapton compared to the structure, which is only etched through the copper. The dimensions of the segment shown here is 2.1 mm high and 1.7 mm wide. The holes have a diameter of 70 μm and a pitch of 280 μm, which is doubled compared to the standard GEM. The area that is required to be copper around the holes stretches for 70 μm from the hole.

integrated circuits (ASIC). This board supports 64 channels per ASIC, thus 128 channels in total.

As the production of the GEM foils takes quite some time - in fact several months - only the design was done during the master thesis. The main focus was set onto the BODELAIRE detector, which is described in the next chapter.
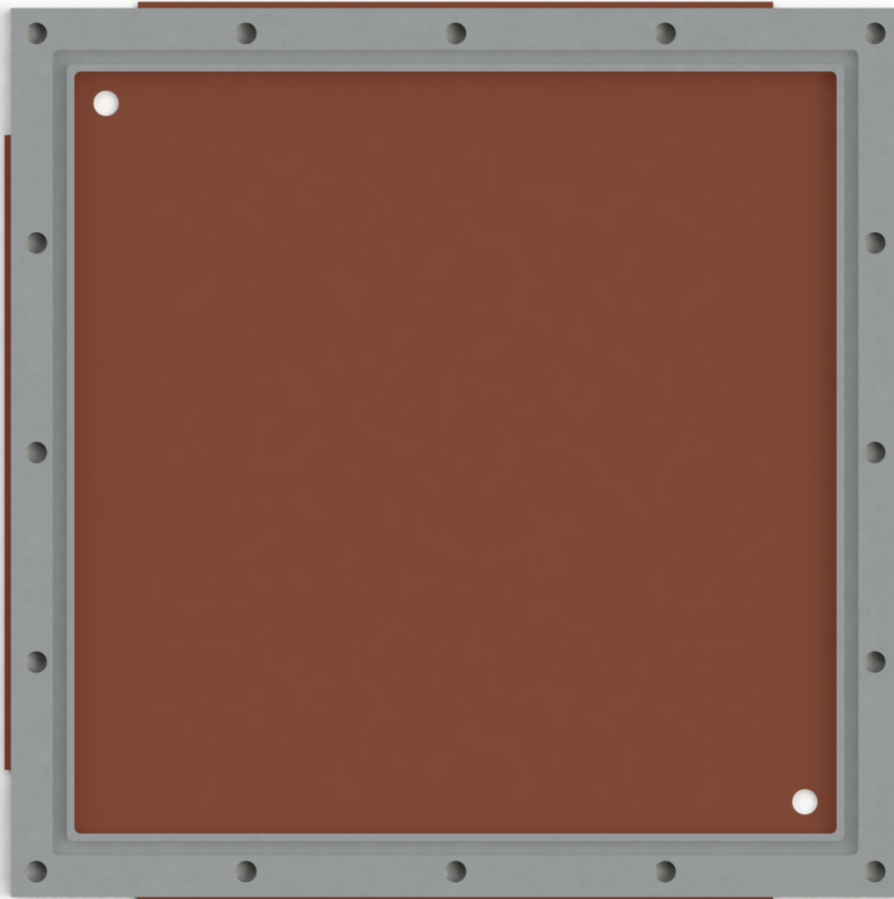
Figure 4.2: A single BASTARD module can be seen. One can see the GEM foil and the frame holding it. There are two bigger holes through the GEM foil in order to make a gas flow possible to adjacent modules. The central part of the GEM will have the structure, as described in the text and depicted in figure 4.1. In the outer part the strips of the GEM will be routed to connectors outside the case. The connectors and the outer part of the GEM foil are left away, but the position is indicated with the small strips sticking out of the frame.
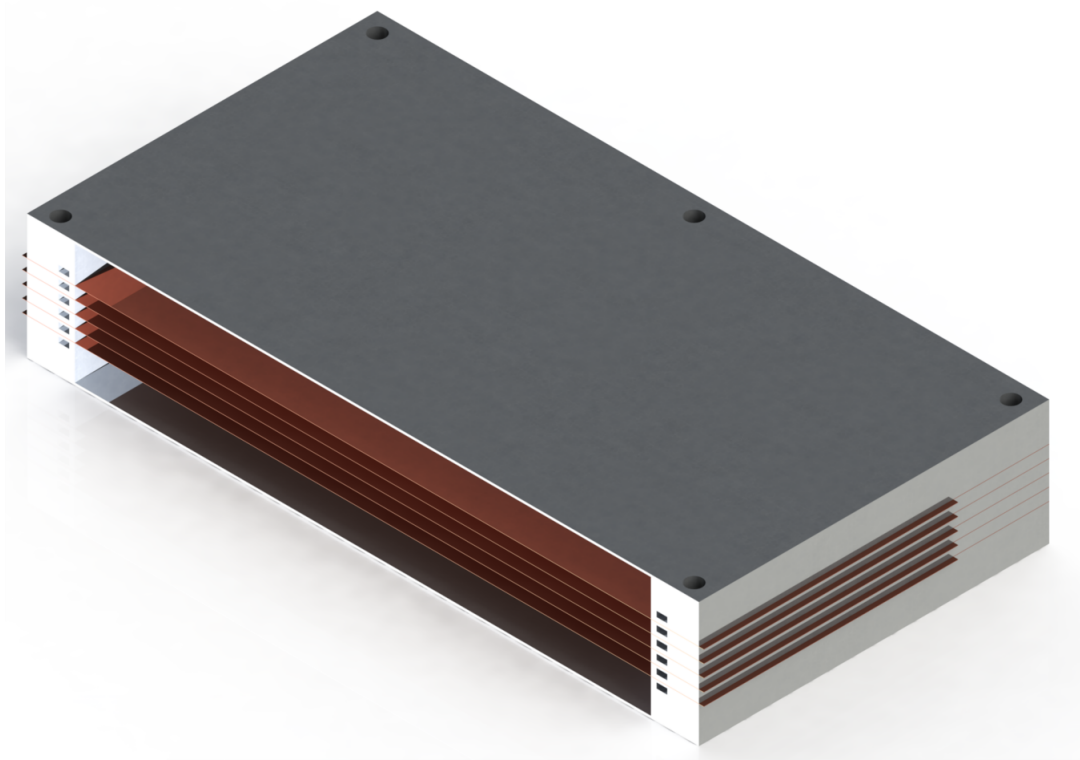
Figure 4.3: A cut through stack of five BASTARD modules can be seen. The modules additionally have end caps on the top and bottom, in order to contain the gas volume and have a gas inlet (which is not depicted here).
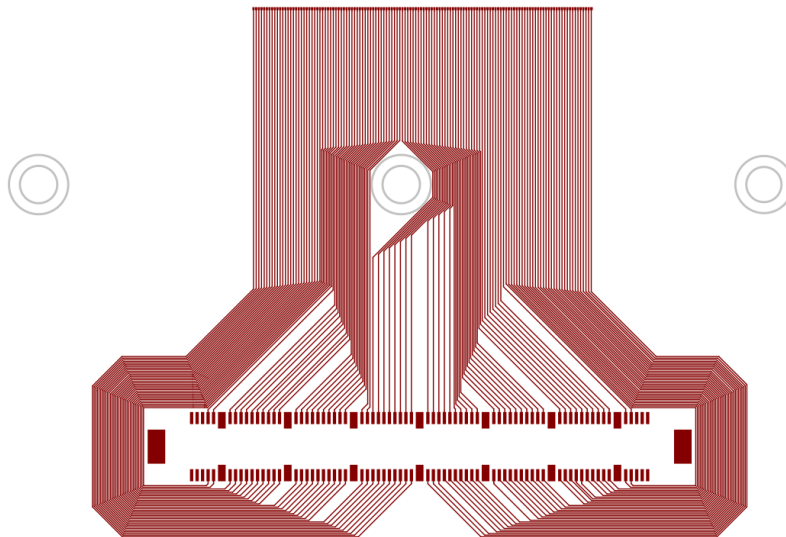
Figure 4.4: An example for the routing for the connection of the strips in the GEM foil to the connector. The pads on the top of the picture indicate the strips, which have a pitch of 242.5 μm and the screw holes of the mounting frame are indicated by the circles, where the outer circle indicates the safety margin. The connector is the HIROSE FX10A-140P/14-SV [37].

BODELAIRE

5.1 Aim of detector

The boron detector with light and ionization reconstruction (BODELAIRE) is a neutron detector with high spatial and time resolution. This is achieved by using the working principle of a time projection chamber (TPC) and a highly granular readout. The detector is built in modular segments in order to instrument large areas. The BODELAIRE detector could for example be used for neutron imaging [38] or fundamental neutron physics [39].

5.2 Design

The design of the BODELAIRE detector can be seen in picture 5.1 and 5.2. On picture 5.1 there are multiple modules of the BODELAIRE detector mounted together. This can also be extended even further by attaching more modules to the sides. The top half and also the bottom half of the modules are separated by a cathode for the electric field. This way the module is split in two parts and has basically double the size. The walls will work as a field cage and guide the electric field to the anode. Additionally the walls act as a trigger for the TPC as they are also partly made of a scintillator. The walls are also connected to silicon photo multipliers, which can be seen below and above the anode. The anodes of the modules are located either on the very top or on the very bottom. Inside the anode the readout chip for highly granular readout is located. The readout is done with multiple GridPix.

5.3 Working principle

In picture 5.2 a detailed depiction of one module of the BODELAIRE detector is shown. The wall of the detector consists of several layers. First, from the inside to the outside, there is a thin boron layer. The born layer has a thickness of about 1 μm, as the particles created by a neutron interaction shall escape to both sides. If it would be significantly thicker one of the reaction products could potentially not escape the born layer and thus the interacting neutron will not be detected. The thin born layer is coated onto a scintillator. The scintillator is used to

Figure 5.1: A picture of multiple modules of the BODELAIRE detector. For a more detailed depiction of one module see picture 5.2 and the chapter 5.3. [10]

detect one of the particles that gets created in the boron due to a neutron interaction. Thereby the scintillator yields light and it can be used as a trigger for the time projection chamber. In order to obtain a good light transport the scintillator is mounted on a glass carrier [40, 41]. The glass carrier also gives the required mechanical stability to the structure. The other side of the glass is then coated with a reflective material, in order to keep all light inside and not lose it. The scintillator it self is also planned to be very thin. This is because it has a lower background if it is thin and only neutron interactions shall be detected. The light transported inside the glass is then guided to silicon photo multipliers (SiPM) in order to be detected.

In order to have a homogeneous field inside the detector the wall also has to act as a field cage. Therefore the boron layer has to be either made of strips and have a continuous voltage drop or be highly resistive. The readout plane at the bottom of the detector will consist of multiple GridPix. These GridPix will have the Timepix3 as a detection chip, as it is a significant improvement compared to the Timepix chip.

If a neutron converts inside the boron layer (for details on the conversion see chapter 2.1.3) it yields two charged particles flying back to back. One of them, in this example lithium, will enter the scintillator and loose all or most of its energy there. This will yield a light signal, which is detected by the SiPM and is used as a trigger signal for the time projection chamber. The other particle, in this example helium, will enter the gas volume and leave a track of ionization. This track will drift to the readout plane and is detected. Thereby one can reconstruct the track in three dimensions, based on the timing information and the detected signal on the GridPix. Thus it is easy to determine the neutron interaction point as this is the position where the track exited the boron layer.
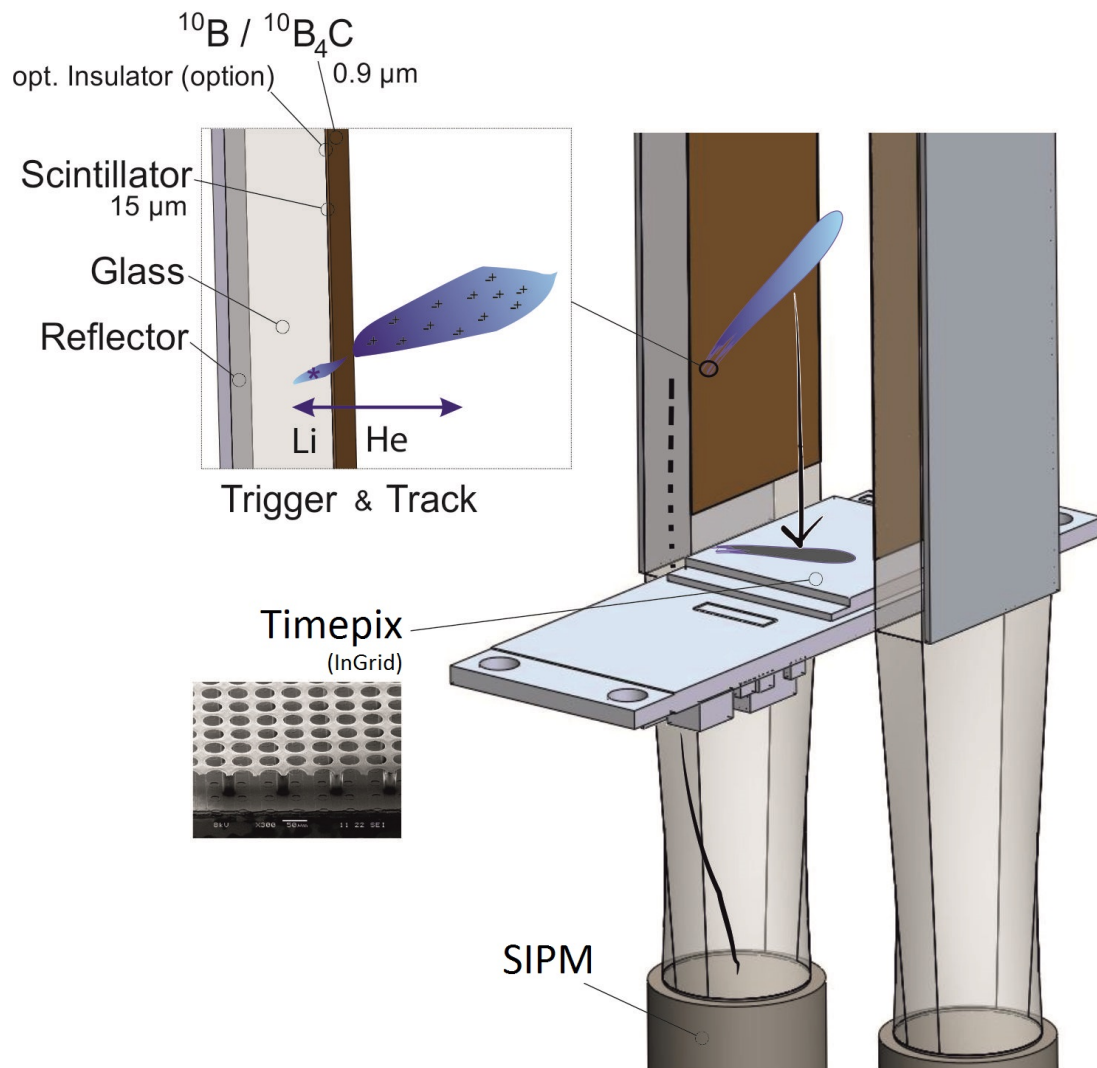
Figure 5.2: I this picture one sees the general setup of one module of the BODELAIRE detector. For a detailed description please refer to the chapter 5.3. [10]

Construction of a prototype detector

This chapter will describe the development process of a prototype detector for the BODELAIRE detector concept. The design of said prototype and measurements done with it and also the challenges that came along will be discussed.
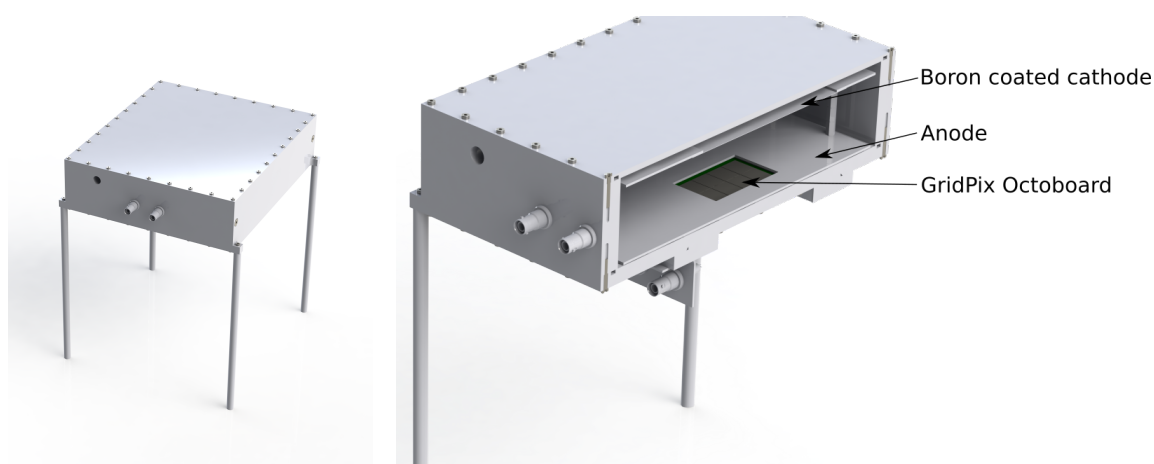
6.1 Design

Upon developing the prototype detector it started with an old detector casing, as it is easier to repurpose an old detector case instead of building a new one from ground up. Some parts had to be adjusted and changed to fit the new prototype. The final design can be seen from the exterior in figure 6.1(a). The exterior of the detector was already existent, but the module with the Octoboard and the Intermediate board had to be done all new. Additionally the bottom had to be manufactured again, as the part available had a manufacturing error that led to big gas leaks. For that all of the detector had to be constructed in an computer aided design (CAD) program SolidWorks [42]. This way also a 3D model of the detector is available and the pictures shown here could be rendered with said software.

In the picture 6.1(b) one can see a cut through the detector. In this cut about half of the detector is cut away, as the most important part, the Octoboard, is in the center. For the Octoboard a module had to be designed to fit the board and also to not have a conductive connection with the three connectors of the Octoboard, but a heat transfer in order to keep it relatively cool. The heat transfer is easily achieved by directly placing the areas that are meant to dissipate the heat in contact with the case. For the connectors there has to be big enough holes in order to avoid sparks of the high voltage. Additionally there were some capacitors on the back of the Octoboard and also some gaps in order to mount and dismount the Octoboard that had to be accounted for. On the other side where the intermediate board had to be placed there had to be cutouts for the soldering pins that are sticking out. Additionally to keep everything gas tight an o-ring had to be placed there. The position of the o-ring is relatively close to all the cut outs, as there is not very much space left. In order to obtain a connection via the connectors between the Octoboard and the intermediate board, the intermediate board had to be embedded into the aluminum plate that the distance is not too big. This module then had to have the correct screw holes in order to be mounted to the remaining detector casing, including an other o-ring

to achieve gas tightness. All of these cutouts can be seen in picture 6.2.

The anode plate inside the detector had to get a fitting cutout in order to leave the Octoboard free and not damage it, including the wire bonds. This was relatively easy as one just had to leave some space from the edges of the Octoboard. Additionally a cathode had to be mounted above and connected to high voltage, but hat was rather trivial, as there were enough high voltage connectors available on the detector casing. The first plan for the cathode was, that it would have a bigger cutout in order to mount a boron coated aluminum sheet there. But it turned out that this was not needed, as tape fulfilled the mounting job easier and no cutout with screws was needed.

(a) Detector case · (b) Cut through detector

Figure 6.1: The left picture shows the final design of the detector case. There are two out of five high voltage connectors visible. Additionally one sees the inlet for the gas system, here depicted only as a hole in the case. On the right picture one sees a cut through the detector. There one sees the boron coated cathode on top and the anode and Octoboard on the bottom.

6.2 Setup for measurement

There were two setups for measurement. The second setup is actually an improved iteration of the first one. In Bonn there is an americium-beryllium source available as a neutron source (for additional information on neutron sources see chapter 2.1.4). As the americium-beryllium source yields high energy neutrons, these have to be moderated. This is done by placing the source in a box. The box is made out of polyethylene (PE) and can be seen in picture 6.3. There is the space for the detector and also for the source. The PE contains high amounts of hydrogen, thus is a good moderator for neutrons due to the similar mas of hydrogen and neutrons. The initial setup was chosen based on a simulation, which varied the position of the source to the detector and also the amount of PE plates in between them. The simulation for the chosen setup can be seen in figure 6.4. The setup then provides thermal neutrons inside the box that can be used for detection. The difference between the first setup (see picture 6.5(a)) and the second one (see picture 6.5(b)) is actually only the arrangement of the PE plates inside the box. The PE

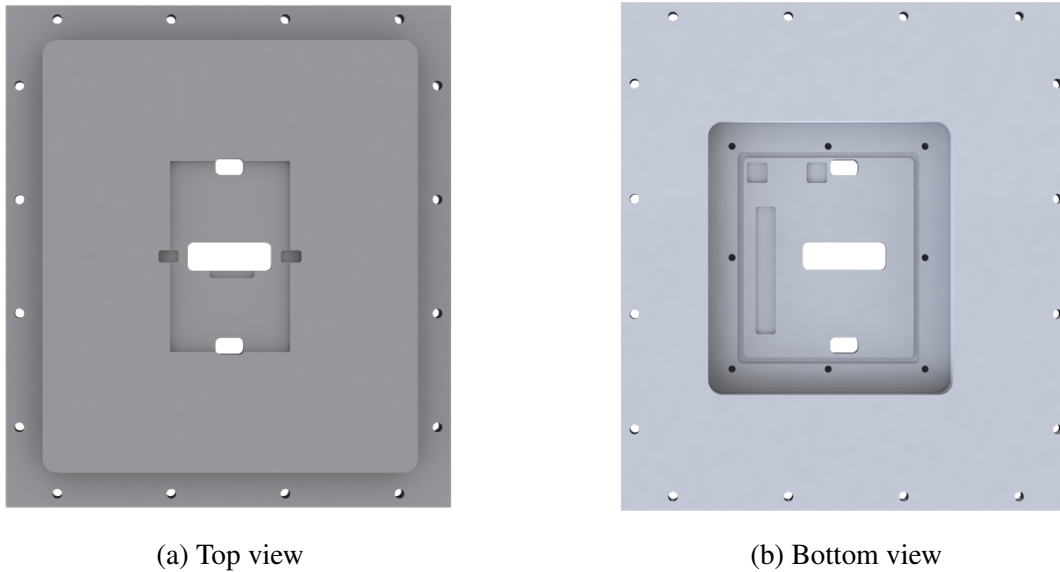(a) Top view　　　　　　　　　　　　　　(b) Bottom view

Figure 6.2: The Module was designed to support the Octoboard and the intermediate board. On the top the Octoboard has to be mounted and on the bottom the intermediate board is to be mounted.

plates were rearranged to improve the thermal neutron flow through the detector. The thermal neutron flow was measured with a helium-3 counting tube, as the counting tube has a bigger conversion volume for the neutrons, thus is more sensible. With this setup the rate of detected events with the detector is about 0.5 Hz.

6.3 Measurement techniques

During the measurements and reconstruction work there were some changes regarding the readout of the detector. The first runs were done without a trigger, as no timing information was recorded. In the reconstruction steps it turned out that timing information is necessary to find the correct neutron conversion point. Thus a trigger was needed and the reasoning for that will be explained below.

6.3.1 No trigger

The first measurements were done without a trigger. The detector ran in a full TOT mode (see chapter 3.4.1) and the frame duration was about 1 s. With this setup one was able to measure the tracks of the neutrons and could see the direction of the converted neutrons. One could get a view of the shape the tracks are and develop a first reconstruction. It was not possible to determine the position of the neutron interaction, as there was an ambiguity between two possible points. As there are always two options for the interaction point one has to differentiate them. An additional layer of complexity is that the starting point for helium is at the lowest ionization density of the track and for lithium it is the other way around. Because of that one had to distinguish lithium and helium tracks in order to use the ionization density as a criterion
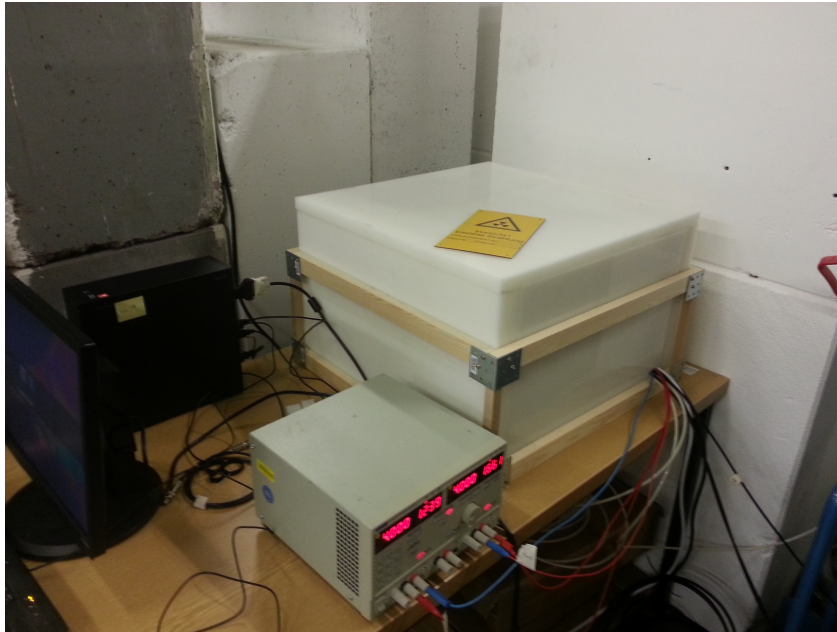
Figure 6.3: The polyethylene box where the detector and neutron source are located. Additionally one sees the power supply for the Octoboard and all the other cables necessary for operation going into the box.

to determine the starting point. This was not possible, thus an other method had to be found to resolve the ambiguity. Additional information was needed and with a trigger this could be gained by recording timing information. In order to obtain timing information some of the pixel that ran in TOT mode had to be changed to TOA mode. With the TOA mode it was possible to determine the stating point.

6.3.2 With trigger

The trigger was needed, if one wants to measure with timing information, as the frame could not have a long duration after the event occurred. The TOA (see chapter 3.4.1) counter can only count up to 11810 and with a clock of 40 MHz this leads to maximal duration of 295.3 µs after the track has been detected. If the frame would be recorded for longer the counter will count into an overflow and the information is useless. There was a measurement done with a frame duration of 250 µs in order to test the quality and quantity of the data. It turned out that it was only possible to detect 150 frames with a converted neutron in 48 h. Thus it is clear that a trigger is absolutely necessary in order to improve the detection rate. Therefore the trigger was used to close the frame after the event occurred. With the trigger and the timing information it is now possible to reconstruct the interaction point of the neutron. Due to the trigger the detection rate decreased a bit compared to the run without a trigger, as the detector was busy reading the frame for a longer fraction of the time compared to earlier measurements with long frames. The neutron detection rate turned out to be approximately 1/5 Hz.

The trigger mainly consists of an amplifier and an Arduino [44]. The electronics board for the
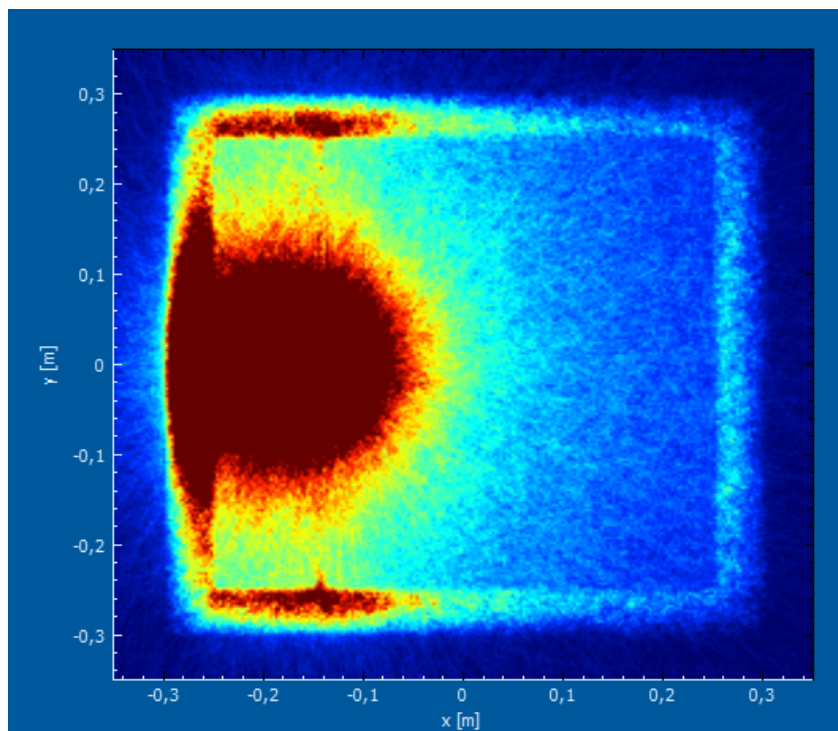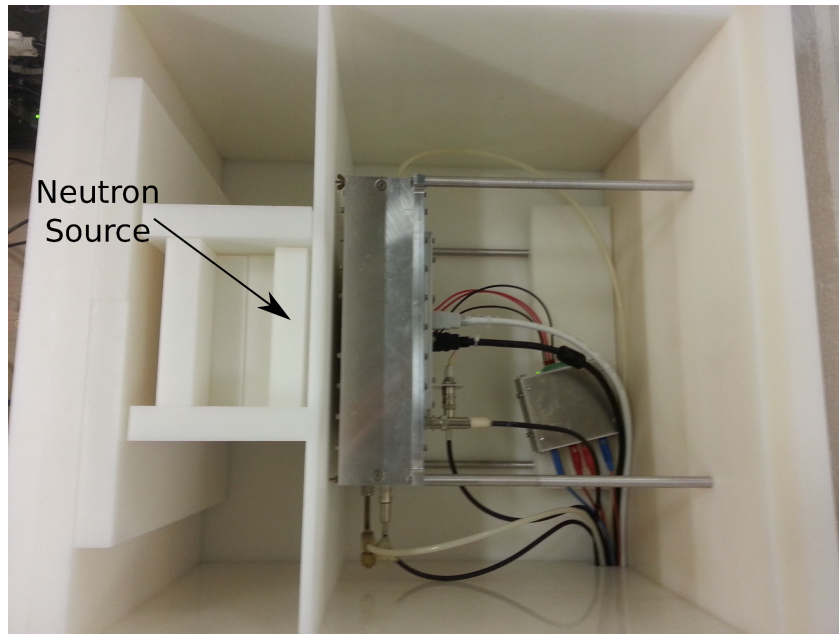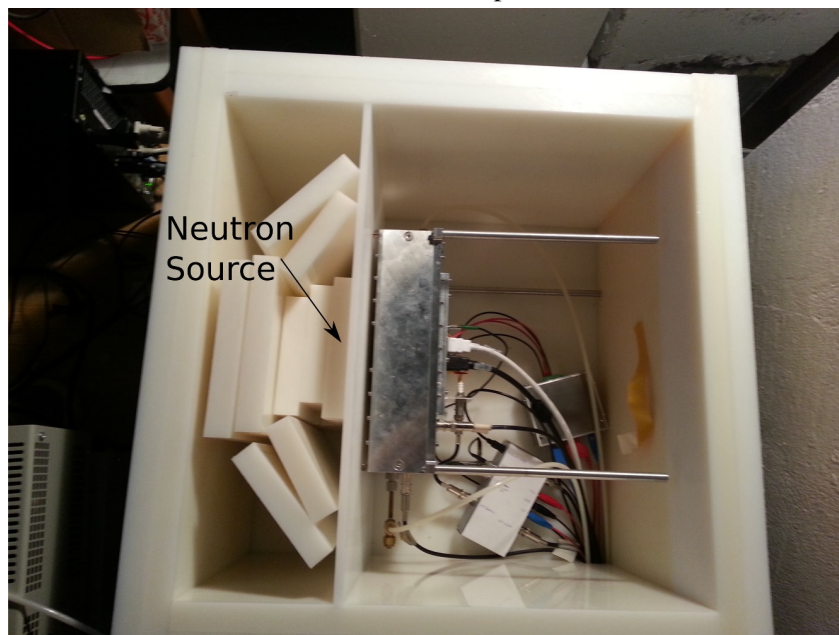
Figure 6.4: A simulation of the neutron source to determine the best position for the source. In the picture one can see the thermal neutron tracks of neutrons moderated by the polyethylene. The source is in the center of the circular pattern. The position is better visible in figure 6.5(a). The simulation was done with URANOS [43].

trigger is a modified version of a counting tube readout board [45]. The input signal is the high voltage of the grid. If the track is detected the ions will flow to the grid and yield a small voltage pulse on top of the high voltage. This can be coupled out via a capacitor and be amplified. If the amplified signal exceeds a certain threshold it works as a trigger signal. After the trigger signal the shutter of the frame is closed and the readout cycle of the chip starts. In picture 6.6(a) one can see the trigger board and in picture 6.6(b) one can see the behavior of the trigger signals. The detailed explanation of the working principle can also be found in the caption.

This trigger was used to measure for multiple days of data taking and all the results of this thesis were recorded with said trigger.

(a) First setup

(b) Second setup

Figure 6.5: depiction of the two setups that were used for the measurement with the neutron source. The first setup was simulated to be the best position for the neutron source and the second setup is an improved version. The improvements were done in order to increase the neutron detection rate, though it only improved it a little.
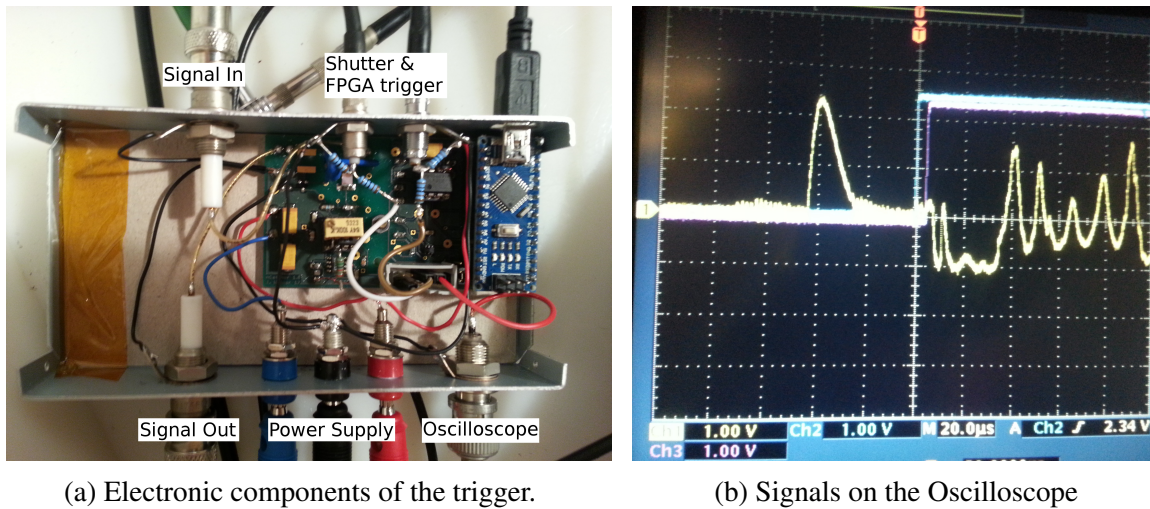
(a) Electronic components of the trigger.

(b) Signals on the Oscilloscope

Figure 6.6: On the left one sees the electronics of the trigger. There are the connections for the high voltage feed though where the signal is coupled out. These are labeled signal in and signal out. Signal in is the connection to the detector, whereas signal out is the connection to the high voltage supply. Additionally the power supply and a connection to an oscilloscope are shown. The connection to the oscilloscope can be used to monitor different intermediate signals of the circuit in order to do crosschecks. On the top there are connections to the shutter and the FPGA trigger. The shutter signal is directly fed into the intermediate board and the FPGA trigger signal is fed into the FEC to instruct the FPGA to perform a readout cycle.

On the right one sees the behavior of the signals if an event occurred. The yellow signal, which peaks at the beginning and later oscillates is the signal after the amplifiers. The peak corresponds to the signal of the ion back flow to the grid of the GridPix, which was amplified by the preamplifier and main amplifier. After that the blue signal, which rises to a high state, is the shutter that closes. This stops the data acquisition on the chip and now the chip can be read out. Shortly after that the magenta signal, which is the FPGA trigger, rises to a high state, which instructs the FPGA to read the frame. The oscillations on the yellow signal are due to the FPGA reading the data and thus inducing this signal onto the trigger circuit. The oscillations during the readout are no harm, as the trigger is set to be blind for input signals during the readout cycle. After a specific time, when the readout is complete, both signals go to low again, which stops the readout instruction of the FPGA and opens the shutter again to take a new frame.

Event reconstruction

The reconstruction is done in multiple parts. At first the data was modified in order to obtain data, like the Timepix3 would output. For the Timepix3 data every pixel has a TOT and TOA value, but for Timepix data every pixel has only one of them, depending on the mode it ran. Thus all pixels obtained the value they were missing by calculating the best estimate for that. For TOT values missing the average of the neighboring TOT values was taken. For TOA values missing, which was the case for most of the pixels, as only 5 % of the pixels ran in TOA mode, the TOA value of the nearest pixel was copied. This way all pixel have a TOT and TOA value. The data had to be modified, because the reconstruction should easily be applicable to Timepix3 data, as the Timepix3 chip will be used in the final BODELAIRE detector. Then track candidates were searched and the interaction point of the neutron was extracted with several fits.

7.1 Cluster finding

As some frames are empty and frames can also contain noise the data has to be filtered. At first the empty frames or frames with very little active pixels are sorted out. This is done by a cut on the file size, such that only frames with signal make it to the next step. This signal can be a track or also unwanted intense noise. In order to filter further a cluster finding algorithm is used. The algorithm used is the so called density-based spatial clustering of applications with noise (DBSCAN) [46]. It is useful for finding clusters and excluding noise, as it is based on a search for clusters via a minimum density of points. This enables the classification of singular points as noise and can exclude the noise for the further fitting process. The main advantage compared to other clustering algorithms like k-means is that it does not need an input on the number of clusters inside a data set and it can find arbitrarily shaped clusters.

The algorithm of DBSCAN needs two parameters and the data set to work. The two parameters are a distance ϵ and a number of points *minPts*. The distance ϵ is used to determine the neighborhood of a point. All points that are closer than said distance ϵ are considered neighbors of the point. Then it is checked if the number of neighbors is bigger than the second parameter *minPts*. If this is the case the point is considered a core point of a cluster, else it is considered noise. For a core point a cluster object is generated and all neighbors and the point itself are added to the cluster. For the neighbors found it is also checked if they are core points. If that is

the case the neighbors of the additional core points are also added to the cluster. If one of the points to be added to a cluster is already flagged as noise that flag is removed and it is added to the cluster. When there are no more core points found for the cluster it is complete. If all points are checked and either added to a cluster or classified as noise, if there are not enough neighbors for that point, the algorithm is finished. An illustration for the algorithm can be found in figure 7.1.

For this algorithm the user has to set the parameters to sensible values. This was done by checking the performance of the algorithm by letting it run over initial measurements and checking by hand if all clusters were found. The final values for the parameters were set to be 5 pixels for the distance ϵ and 15 points for the minimum number of neighbor points *minPts*. The high number of minimum neighbor points leads to a suppression of small clusters of noise pixels and to still get clusters of not very dense tracks it was necessary to set the distance to a relatively large value. After all clusters are found, the corresponding data is written into a root file. The file contains, for each found cluster, the full data recorded by the chip with TOT and TOA and the cluster by itself. This is then handed over to the fitting routine.
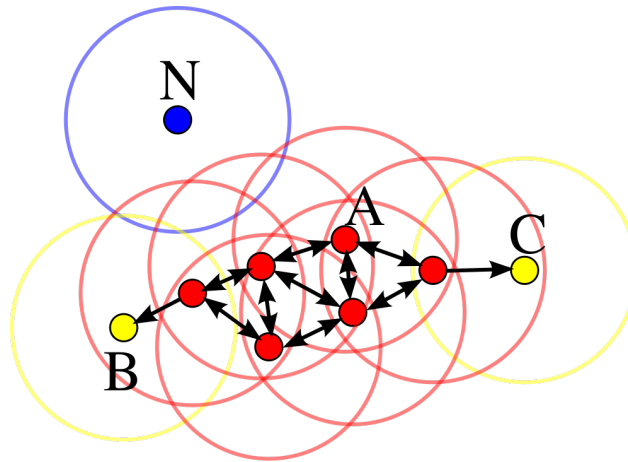
Figure 7.1: Illustration of the DBSCAN algorithm. The parameter *minPts* is chosen to be 3 for this illustration and the parameter ϵ is depicted as the circles. Point A is considered a core point, as well as all other red points. Point B and C are no core points, but still belong to the cluster, as they are neighbors of a core point. Point N has no neighbors, thus is considered a noise point. [47]

7.2 Fitting and cuts

The file generated by the cluster finding algorithm is taken by a fitting routine. The fitting is done with root [48] using custom functions. Here the steps for the reconstruction will be explained and at the end of this chapter pictures following these steps will be shown additionally a flow chart summarizing the reconstruction is shown in figure 7.2.

At first it is checked if there are at least a certain number of points, meaning active pixels, available. The threshold on the number of points required for a track was set to be 450 points in one cluster. If there are less than 450 points the event is skipped. Clusters with less than 450
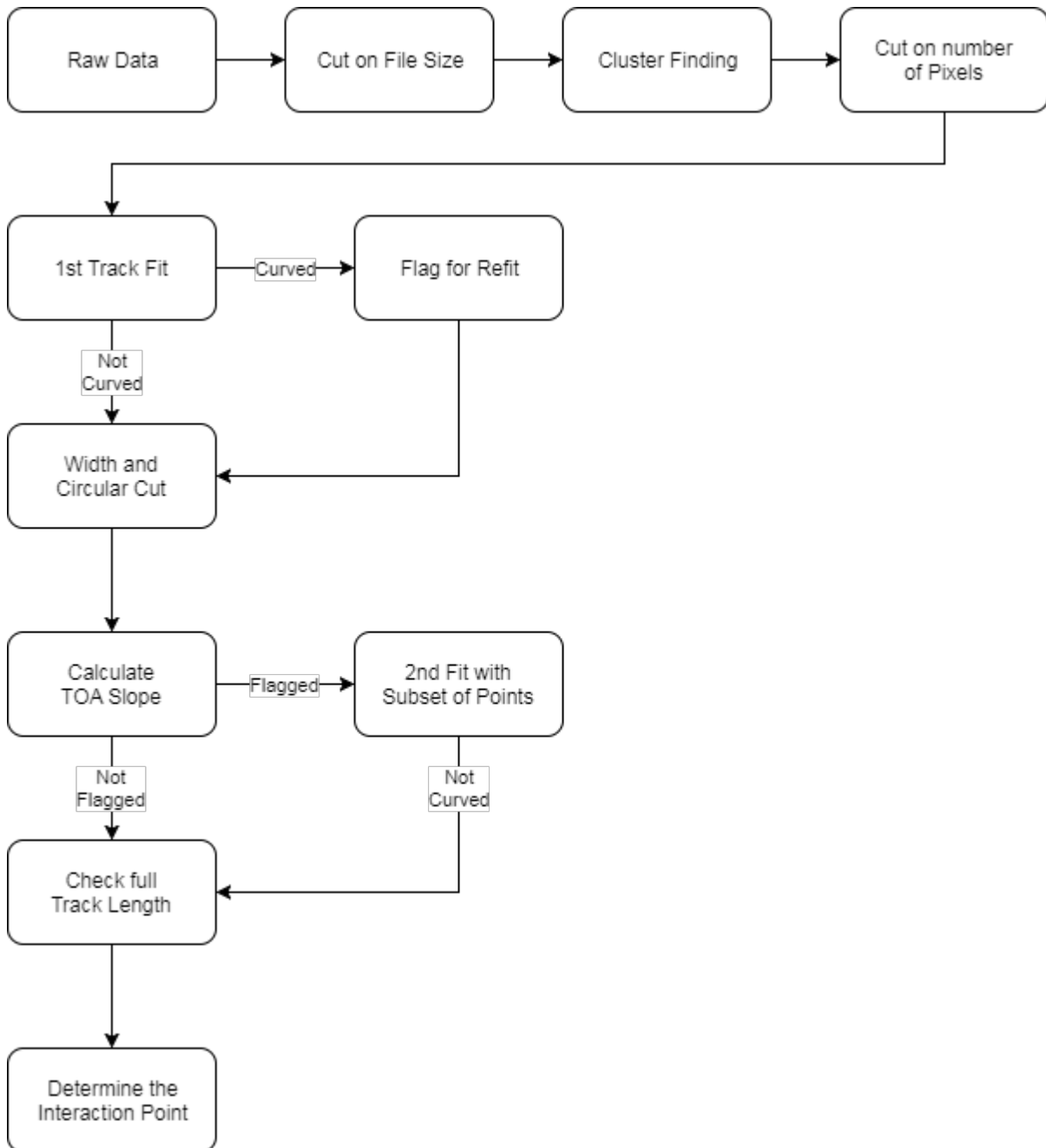
Figure 7.2: A flow chart depicting the reconstruction steps for the measured data. If any of the steps yields an exclusion the track is discarded. The details on the corresponding cuts are explained in chapter 7.1 and 7.2.
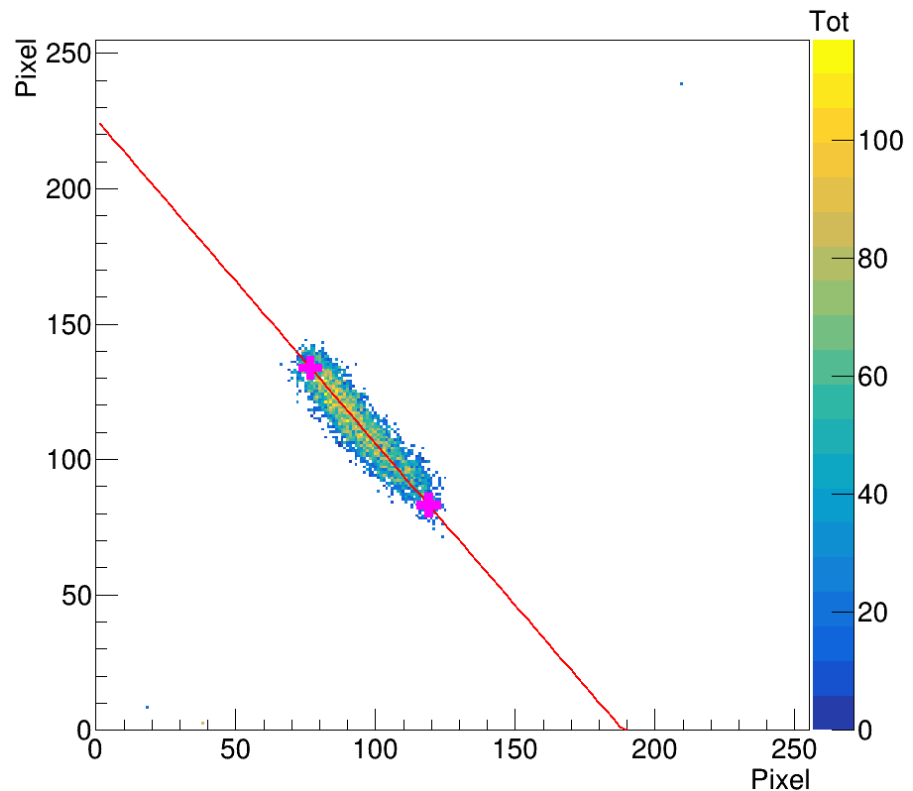
Figure 7.3: The cluster survived the initial cuts on the amount of active pixels and also not being circular. Then the fit was performed for the track and the two possible neutron interaction points were calculated and are shown as magenta crosses.

points are no tracks and typically also fail other conditions, thus computing time is saved. After that a first linear fit is performed to reconstruct the track. The first fit is of course crosschecked and if it is not sufficiently good it will be redone with some modifications, later on.

After the fit is done the length of the track is easily computable. Also the width of the track is computed and if the track is not at least twice as long compared to its width it is also discarded. This is due to the fact, that if the track is circular it is quite complicated to perform a decent track fitting, as the direction of the track is not always directly clear. This also rejects photons, which are a background for neutron sources, as photons form circular patterns instead of long tracks.

After that the initial fit is checked for quality. It has to be sufficiently straight and go through the center of the cluster. This check is done by projecting the track on the x-axis in a new diagram and checking if the resulting moved cluster yields a horizontal line as a fit. The curvature is checked by looking at terms of higher order of the fit. If the fit shows a too high curvature it is flagged for a refit later on.

After that the possible neutron interaction points are determined. This is done by determining the end points of the track and from there on moving to the inside by a small amount. The distance moved inside along the track is determined by the width of the track, as the charge diffused during the drift diffuses equally in all directions and thus the starting point is not directly on the edge of the track. With this one obtains two possible neutron interaction points. An example can be seen in figure 7.3.

Without timing information one would be lost here, or one would have to find a complicated algorithm to choose the right interaction point. With timing information this task is rather trivial.
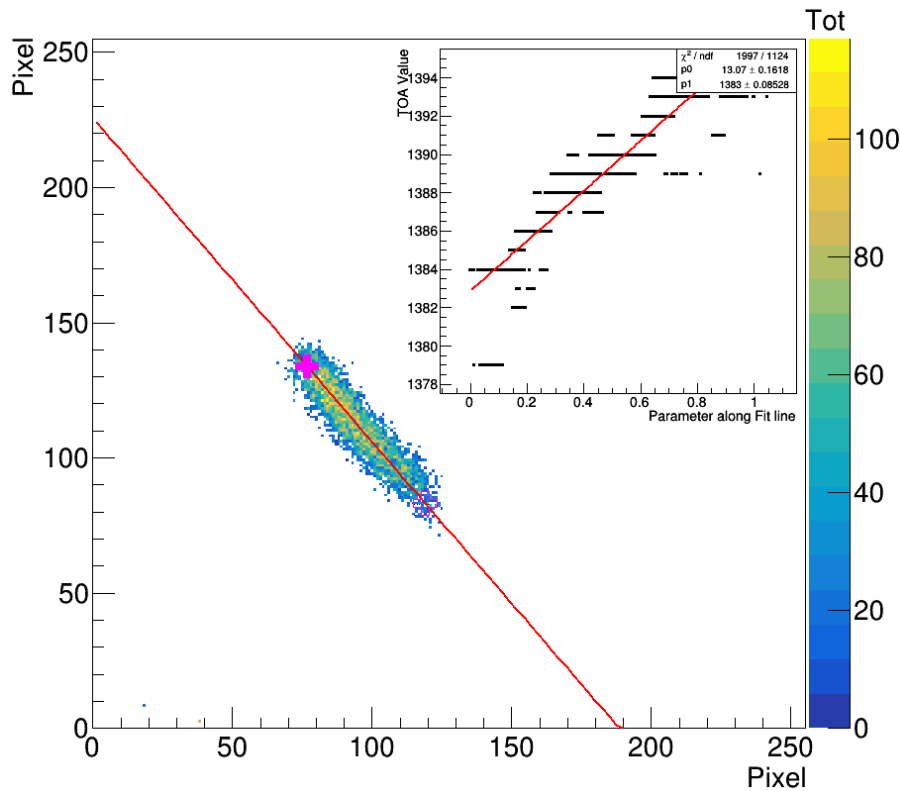
Figure 7.4: In order to determine the right interaction point out of the two options, the TOA values are mapped along the track. In the smaller diagram the axis labeled parameter along fit line goes into positive x direction. Thus the possible interaction point with the smaller x value is the correct one. The correct interaction point is shown as a filled magenta cross, whereas the incorrect one is shown as an outlined magenta cross.

The end of the track with the pixels activated last is the end with the starting point, as they arrived last and had the longest drift distance from the cathode. This can be determined by mapping the TOA values of the pixels along the track and fitting a straight line through them. Then the end with the lower TOA values is the end with the interaction point. One has to keep in mind that the TOA counter counts from the activation of the pixel to the end of the frame, thus the lowest TOA values correspond to the pixels activated last. An example can be seen in figure 7.4.

After knowing the position of the neutron interaction the tracks flagged for a refit are being processed. The tracks are cut either horizontally or vertically, depending on their orientation, to obtain half of the track with the neutron interaction point. The part of the track is then refitted and checked for the curvature again. If it is still curved it is discarded, but if it is sufficiently straight, the neutron interaction point will be recalculated based on the new fit. A successful example can be seen in figure 7.5.

After determining the position of the interaction point the track is checked to be an actual neutron conversion product. The length of the track is calculated by calculating the length in two dimensions, which was already done before, and also the length along the drift direction and adding them in quadrature. The length along the drift direction is calculated by taking the difference of the TOA values at the start and end of the track and converting that with the drift velocity and the clock frequency to a distance. If the calculated length of the track is more than 1.05 cm it is also discarded, because it is longer than the neutron conversion products could make it in the counting gas (Ar CO_2 70:30 or 80:20). The maximal distance the conversion products can traverse in the counting gas is about 1 cm (see figure 2.2). All tracks longer than

Figure 7.5: For this track the initial fit (red line) was not successful, as the track has a big curvature. Therefore it was flagged for a refit and after cutting the cluster in half the new fit succeeded (yellow line). The cut is not depicted here, but the yellow fit only operated on a subset of the shown pixels. Then the interaction point was recalculated according to the new fit.
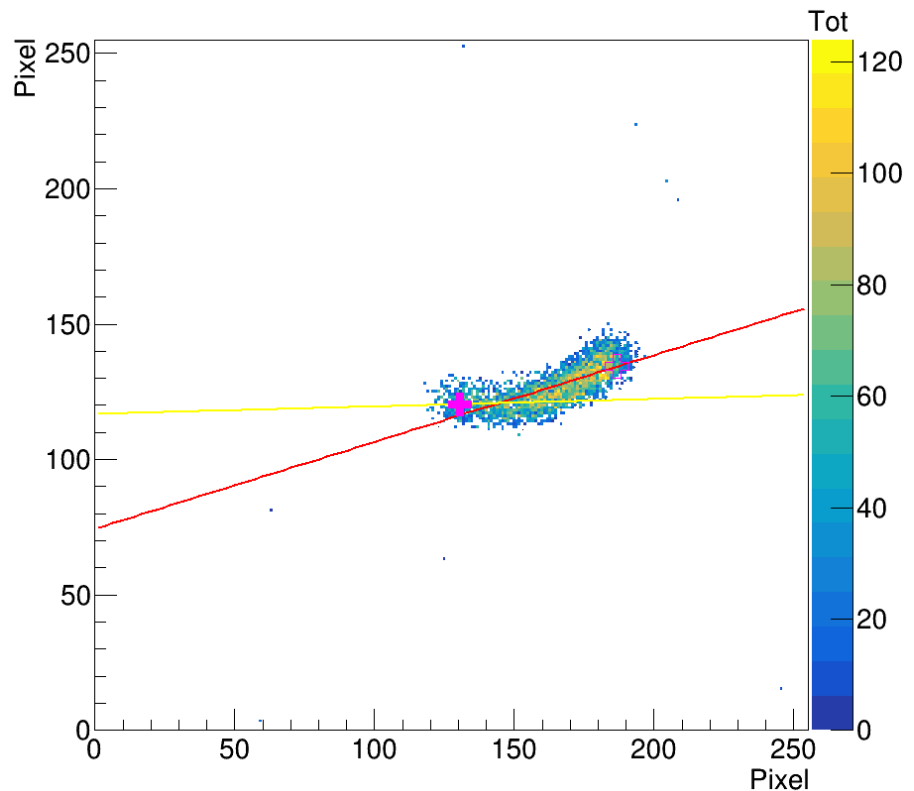
that are most likely electrons or protons, which are either background or unwanted neutron interactions with a proton originating out of a light atom.

Then all neutron interaction points and fit parameters are written to a file. The neutron interaction points are additionally put into a root histogram in order to visualize the distribution. This distribution for the different measurements can be seen in chapter 8. Pictures for all of these reconstruction steps can be seen in figures 7.3 to 7.5. Additional pictures, also with rejected tracks, can be seen in the appendix A.

7.3 Data and track characteristics

During the reconstruction it was necessary to know the properties of the Octoboard and also where the defects are. This is to exclude areas where the track will be deformed due to field distortions and holes inside the grid. The easiest way to see that is an occupancy plot. The occupancy plot for one measurement can be seen in figure 7.6. The first thing one notices are the field distortions at the corners of the chips, as there are nearly no hits. Also one can see that chip three, which is the second one in the top row, is dead and that chip eight, which is the last one in the bottom row, has nearly no events. The low amount of events on chip eight are intended, as is has a tendency to spark, where the red area on that chip is, as the grid is damaged there. Also the red shape in the lower corner of chip two, which is the third one in the top row, is a defect of the grid. Additionally all the cuts and holes in the occupancy plot show where there are small field distortions due to grid defects. In this occupancy plot one can also get an

estimate of the structure, as most of the hits are where the boron sheets are located. With the information of the defects the areas with large detects could be excluded for the reconstruction.
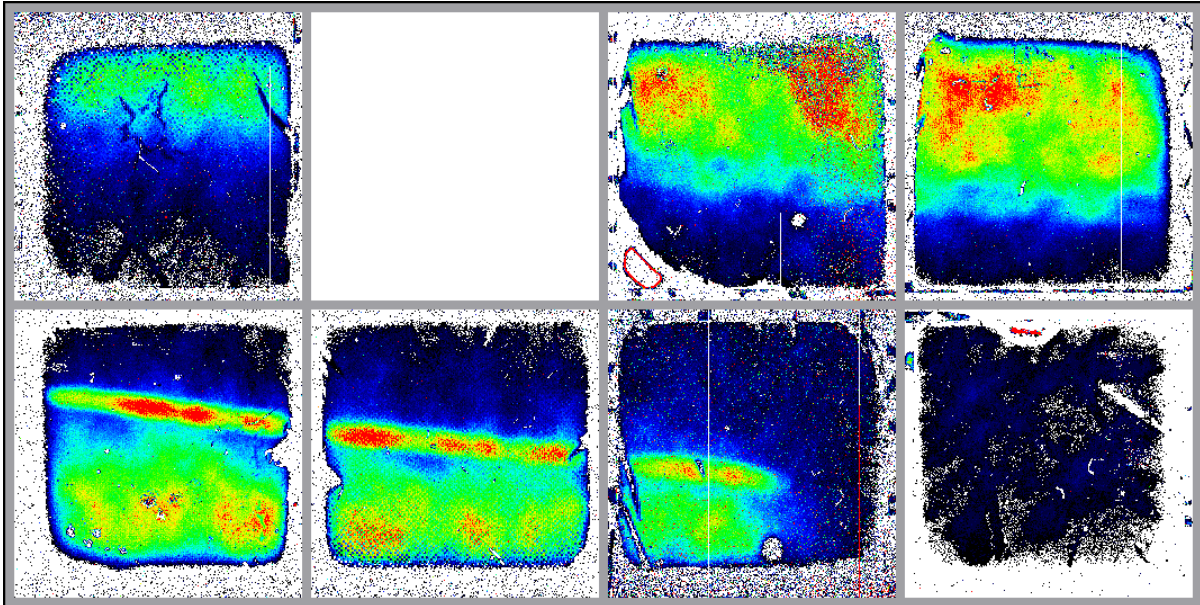

Figure 7.6: The occupancy plot of the Octoboard for one measurement can be seen. The occupancy is the number of hits on the pixels over the full measurement. The more red the area is the more hits were there.

During the reconstruction also statistics for the different track parameters, like the with, length or others, are calculated. The distributions for some of them can be seen in figure 7.7 and 7.8. The width of the tracks is relatively constant, as it can be seen by the sharp peak. The average width is about 12 pixels and the variation is up to 2 pixels. The average width of 12 pixels corresponds to a diffusion of 660 µm, as one pixel has a size of 55 µm. If one compares that to the diffusion one can expect for Ar CO_2 (80:20), which is about 550 µm [49] for the drift distance of 3.8 cm, it is relatively close. For the length one can see a distribution that starts at 0.2 cm. That there are no shorter tracks is due to the reconstruction, as the tracks can only be reconstructed is they are not too circular, thus have a minimum length. The distribution is relatively flat until it declines towards 1 cm. This is the expected behavior, as the maximal track length of a neutron conversion product is about 1 cm. All tracks with a length above that value are either not reconstructed correctly or other particles like electrons or protons. Additionally the simulated track length is given as a comparison in the same figure. In the reconstruction all tracks above 1.05 cm are excluded to remove the electrons and protons.

The measurement that was done for the reconstruction, as described in chapter 8.3, contained 1070 thousand frames. Out of these 1070 thousand frames only 162 thousand frames were not empty. These frames were then handed to the cluster finding algorithm. After the cluster finding there were 161 thousand clusters found. These were then analyzed and 29 thousand clusters were identified as neutrons that could be correctly reconstructed. The interaction points of these are later on depicted in figure 8.4(b).
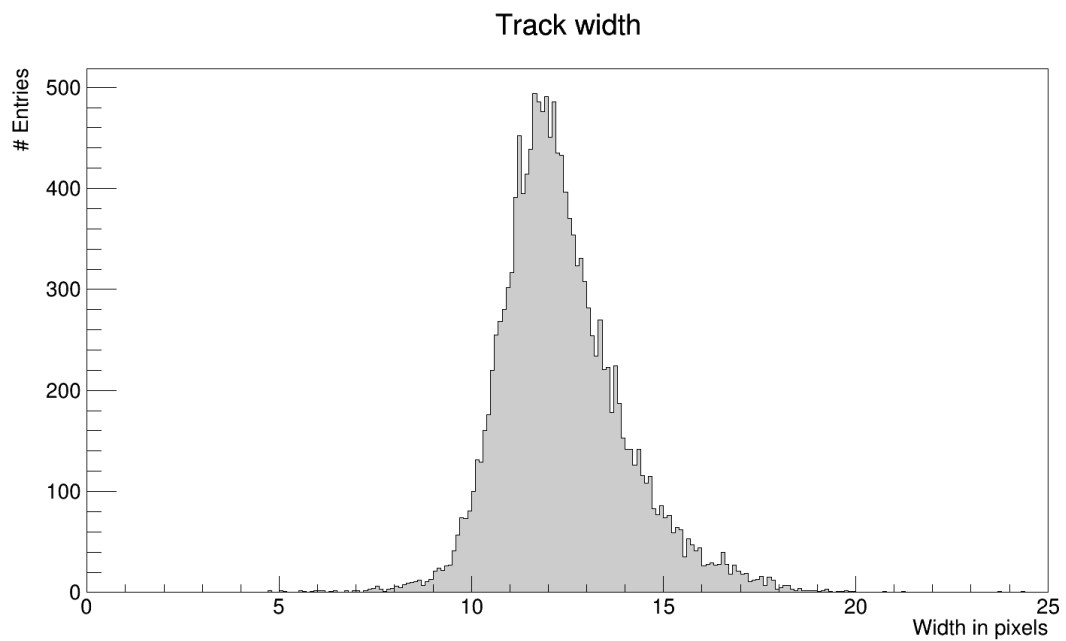
Track width

Figure 7.7: The distribution of the width of the tracks is depicted. The average width is 12 pixels and the variation around that is about 2 pixels. The average width of 12 pixels corresponds to a diffusion of 660 μm, as one pixel has a size of 55 μm. If one compares that to the diffusion one can expect for Ar CO_2 (80:20), which is about 550 μm for the drift distance of 3.8 cm, it is relatively close.
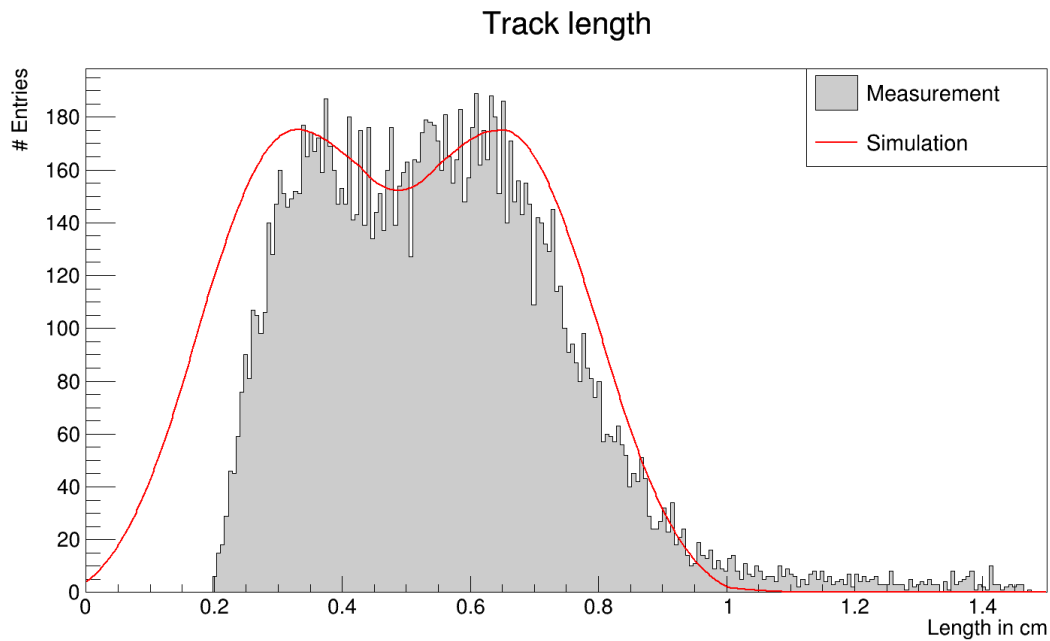
Figure 7.8: The distribution for the length of the tracks is depicted. The start at $0.2\,\mathrm{cm}$ is due to the requirement of 450 pixels during the reconstruction and the decline towards $1\,\mathrm{cm}$ is due to the maximal range of the conversion products. In red a simulation for the track length is given. The deviation on the right is due to tracks cut off at the edges and the deviation on the left is due to the minimum required number of pixels.

Measurements and Results

8.1 Tests with neutrons

First tests of the detector with a neutron source showed the topology of the tracks generated by neutron conversions. For all the measurements, if not noted otherwise, Ar CO_2 (70:30) was used. The first measurements were done in full TOT mode and had the disadvantage that the neutron interaction point could not be reconstructed. The first measurements yielded an estimate on the rate of neutron conversions inside the detector, which was about 0.5 Hz. An example how such neutron conversion events could look like can be seen in figure 8.1 with multiple neutrons recorded over a frame duration of 18 s. These test revealed that there was additional information necessary in order to obtain the neutron interaction point. The detector had to be operated in a mixed TOT and TOA mode in order to make it possible to reconstruct the neutron interaction point. Therefore further tests to include the timing information were needed, but as the neutron source was rather weak the tests were performed with alpha particles, as those are one of the neutron conversion products.

8.2 Tests with alpha particles

As the neutron conversion product in boron is either lithium or helium - an alpha particle - it is possible to test the detector with an alpha source. The alpha source used for the test was an americium source. Although it yields alphas of approximately twice the energy compared to the energy of the alphas created by the neutron conversion, it still shows a similar topology. Additionally the measurement with an alpha source is much easier, as it has a higher intensity and is easier to handle, as it does not need a moderator. The measurements done with the alpha source were tests of the TOA setup in order to decide the fraction of pixels the should be set to TOA mode instead of TOT mode. The tested fractions of pixels set to TOA mode was 10%, 5% and 1%. The setting with 10% of the pixels set to TOA mode was way too much, as there were too many pixels set to TOA mode which could be running in TOT mode instead and record the charge information. The test with 1% of the pixels set to TOA mode showed too low occupancy of TOA pixels, as there was a chance that a track does not have enough TOA pixels in order
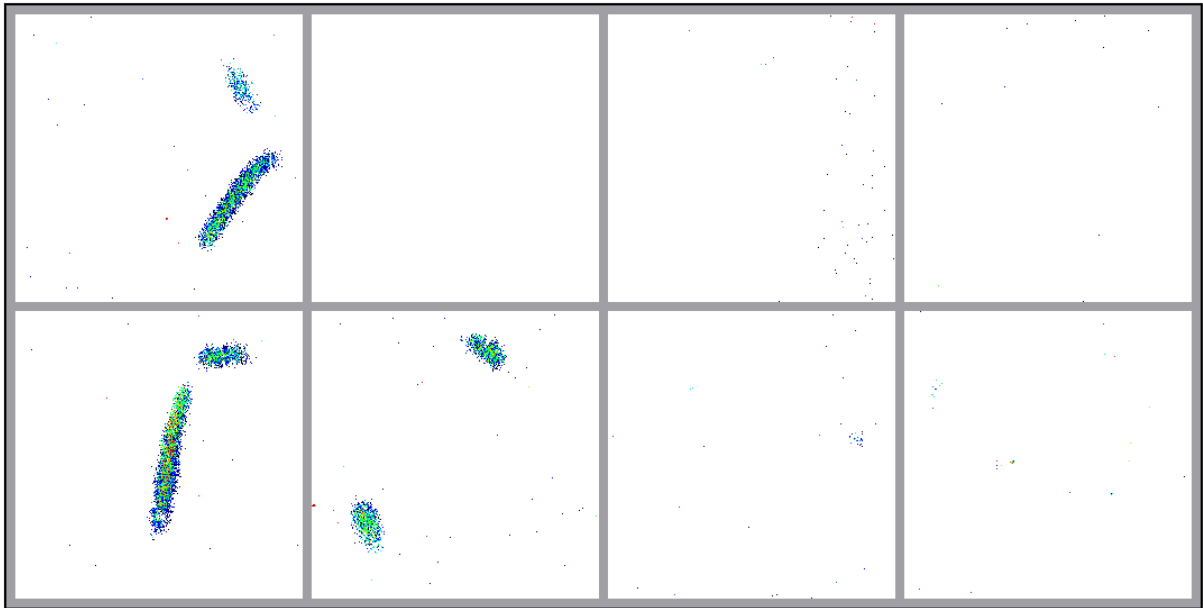
Figure 8.1: One of the first recorded frames showing neutron conversion products. The duration of the frame is 18 s. The color of the pixels indicates the TOT value. If the color is more red it corresponds to higher TOT values and if the color is more blue it corresponds to lower TOT values. One also sees the small amounts of noise that occur during a measurement over that long duration.

to determine the correct starting point. In the end the setting with 5% of the pixels set to TOA mode was chosen, as it did not have too many pixels set tot TOA mode, but enough to ensure that there are enough pixels per track that recorded a TOA value.

The alpha source also aided in developing the analysis code, as the data set for the alpha particles will be bigger for a set recording time, as the source has a much higher intensity and does not need a trigger. Additionally it aided during the tests of the trigger, as the rate was known and one did not have to wait for a trigger signal for several seconds. Final measurements for resolving a structure and determining the spatial resolution are of course done with neutrons.

8.3 Structure measurements

In order to resolve a structure with neutrons the detector was operated with a trigger, as timing information was needed for the reconstruction. There were two setups that were used for the structure measurements, but the reconstruction steps were the same for both of them, as described in chapter 7.

The object that was resolved with neutrons changed between some measurements, thus there are different patterns visible. Additionally the Octoboard that was used for the data taking was not in the best shape anymore, so some defects will be visible, like one chip not working at all. Other defects of the Octoboard include an other chip always yielding higher signals compared to the others and having a tendency to spark. Also the InGrid structure above the Octoboard was not in the best shape and had some holes and bumps, thus was not perfectly uniform and lead to
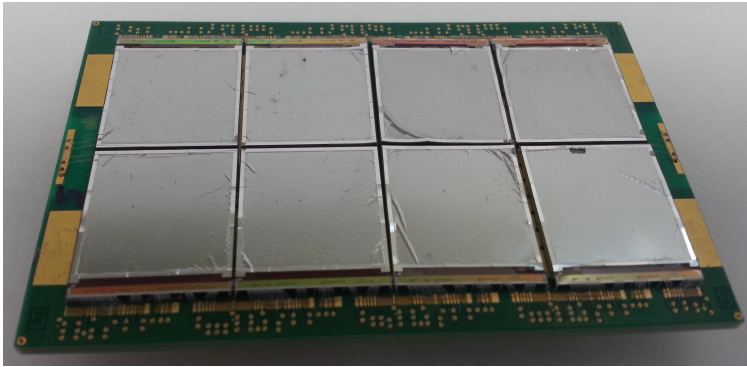
Figure 8.2: This picture shows the Octoboard that was used for measurements. The defect on the last chip in the bottom row is clearly visible and the bumps on the grid are also visible.

field inhomogeneities. A picture of that Octoboard can be seen in figure 8.2. Due to the defects in all measurements one chip will show no signal at all and an other chip, which is at the corner, will be left uncovered by the object in order to reduce or prevent sparks. The chip not working was the chip with the number three, which will always be depicted as the second chip in the first row. The chip which had a tendency to spark was the chip eight, which will always be depicted as the last chip in the second row. Additional defects of the board were that the grid structure above the chips was slightly damage at some positions, thus reducing the gas gain there and potentially generating holes inside a track. The issue with the holes inside the track is rather unfortunate for the track fitting, but could not be circumvented. Additionally one chip, to be exact chip seven which is depicted as the third chip in the second row, had a partially defect column of pixels. The partially defect column lead to a column of pixels missing for tracks on that chip, but that did not influence the performance of the fitting by much.

The first structure resolved was a boron coated aluminum strip. The strip was mounted on the cathode with kapton tape and the picture one would expect on the readout by the strip is depicted in picture 8.3(a). As one sees the middle of the chips is covered and the outer area is left blank. The actual measurement to resolve that strip was done over several hours and the result can be seen in figure 8.3(b). There one clearly sees that the chip 3, which is the second one in the top row is not working, as there are no hits. Next one recognizes that towards the border of the chips there is an increase of hits and then nothing. This is due to the field distortions between the chips. There is a small gap between the chips mounted on the Octoboard. This gap has a size of about $100\,\mu m$, but this is enough to distort the field on the borders of the chips. Thus on the borders of the chips there are no pixels active due to a low gas gain and the tracks end there. All tracks that have the interaction point at the border of the chip and additionally all tracks that have the interaction point off the chip will get a reconstructed interaction point at the corner where the field distortions begin. Thus there is a large increase of interaction points depicted there. The rest of the chip is relatively evenly filled with interaction points and at the corner of the boron coated aluminum strip there is a drop in neutron interaction points. Thus one can resolve the strip by resolving the drop in interaction points.This was the first measurement done and there are improvements to be made. One improvement is to not place the edge of the strip so close to the edge of the chips, as that will end up not detected due to the field distortions. Another improvement is to make the strip thinner to again move the edge inwards.

As the improvement could not easily be done with the current setup, because the strip had a fixed width, the setup was reversed. Instead of one strip in the middle, there were two strips
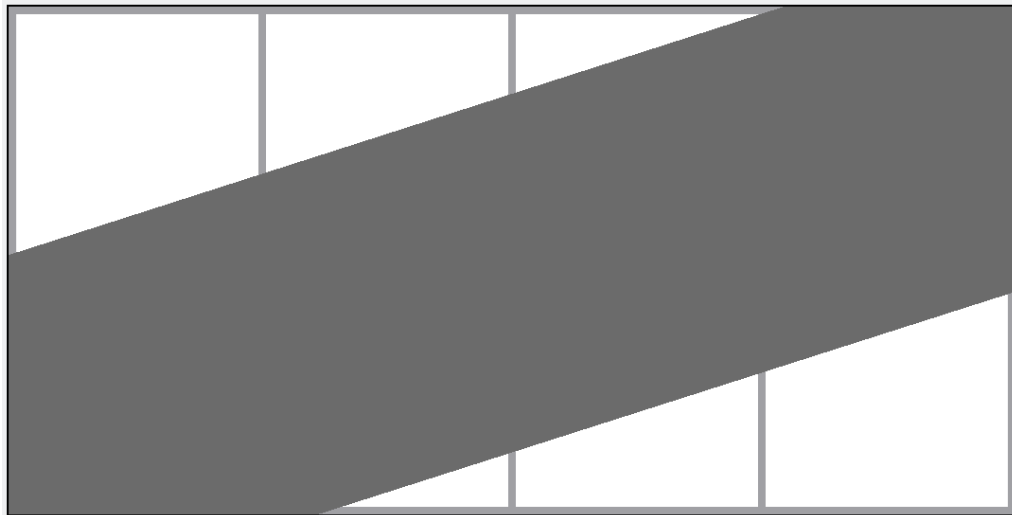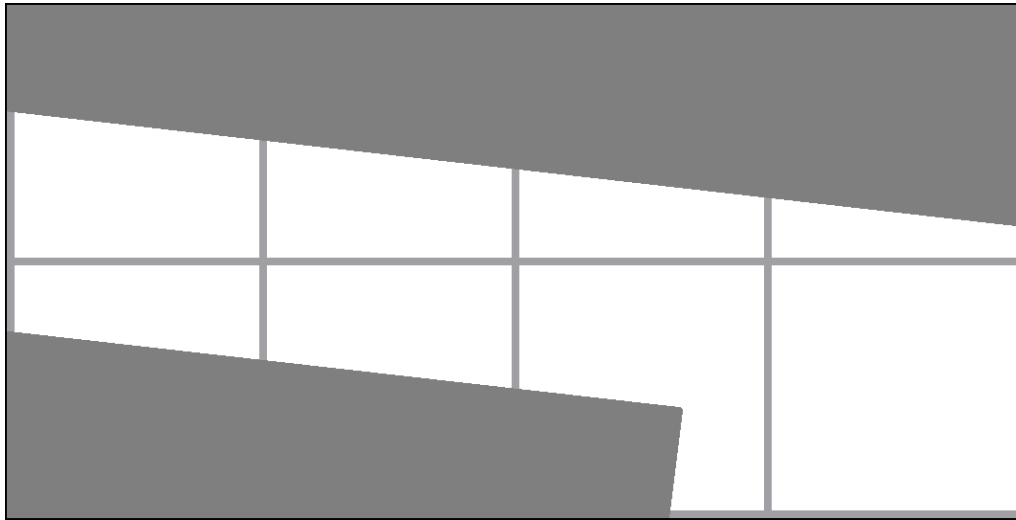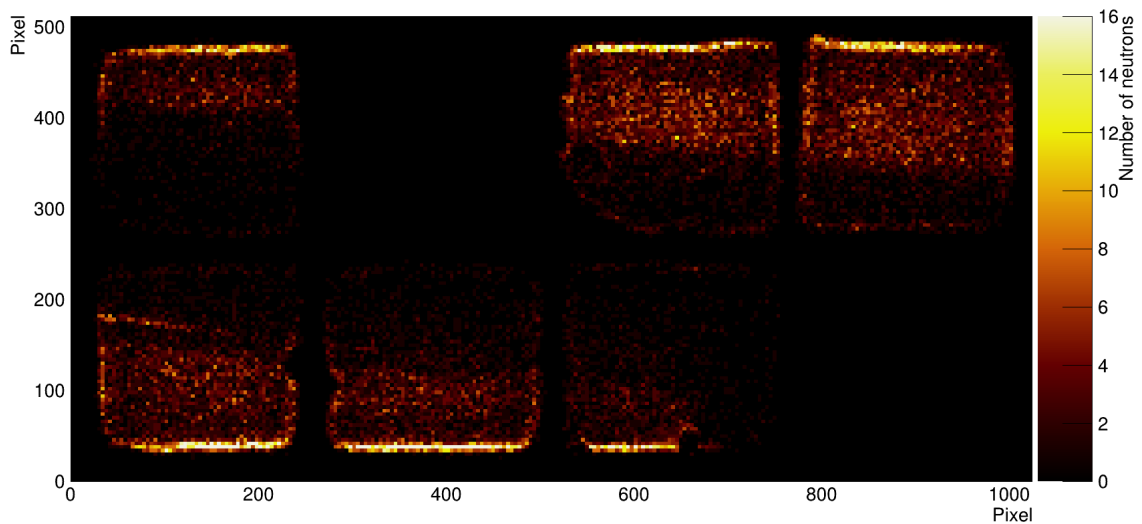
(a) Expected structure
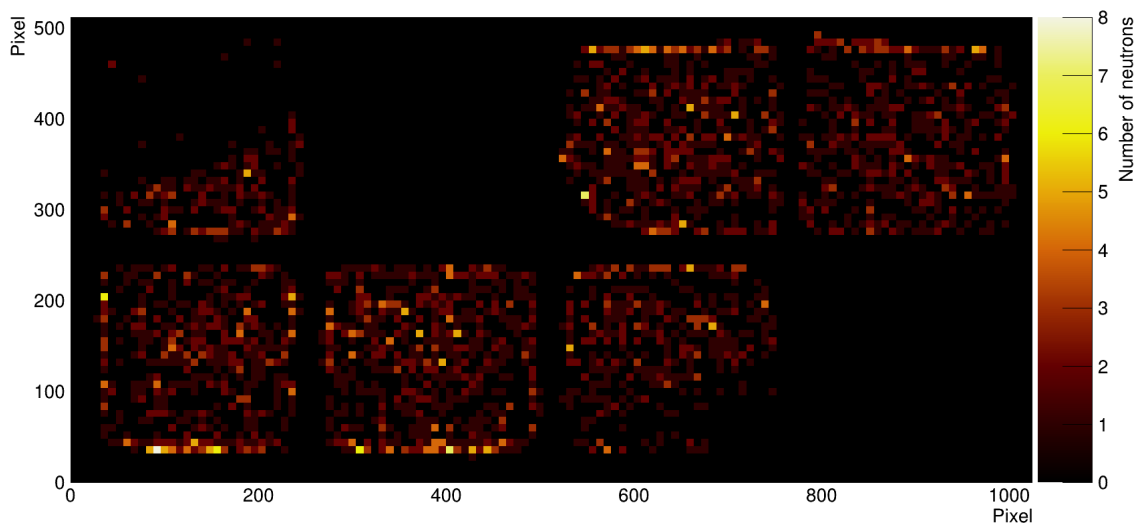
(b) Measured distribution of interaction points

Figure 8.3: These pictures show the expected structure that should be resolved with the neutrons and the actual measurement for that. The amount of data is not very high, as there are only about 3000 reconstructed neutron interaction points. Note that the chip three, which is the second one in the top row is dead, thus shows no signal. Also the chip eight, which is the last one in the bottom row, was not covered much and sparked often. This measurement lead to improvements of the structure, such that it could be resolved in a better way.

(a) Expected structure

(b) Measured distribution of interaction points

Figure 8.4: These pictures show the expected structure that should be resolved with the neutrons and the actual measurement for that. This structure differs from the first one, as it can be clearly seen, with the reasoning described in the text. The amount of data is way higher compared to the first measurement and it was possible to change the size of the bins in the histogram. In this histogram there are about 29000 reconstructed neutron interaction points depicted. The z axis - Number of neutrons - was cut at 16 in order to have a better visible edge, as the corners of the chips would dominate the color spectrum. Note that the chip three, which is the second one in the top row is dead, thus shows no signal. Also the chip eight, which is the last one in the bottom row, was not covered because it would spark often. If one compares the bin size of this distribution to the bin size depicted in figure 8.3(b) one can clearly see a difference. This is due to the different amount of statistics, as this measurement has much more statistics.

mounted on the sides and leaving the middle blank. The new arrangement can be seen in figure 8.4(a). This now has the edges closer to the middle of the chips and makes this structure easier to resolve. Additionally one sees that the last chip in the bottom row is left out intentionally, as this is the chip which had a tendency to spark. The measurement for this setup was done a longer time over several days. Over that time frame the gas bottle with Ar CO_2 (70:30) got empty and the major part of the measurement was done with another gas bottle with Ar CO_2 (80:20). The different gas mixture did not influence the shape or topology of the tracks by much, thus the same analysis could be applied. The two data sets were analyzed separately, but the final picture showing the resolved structure is merged. This measurement has much higher statistics, thus it is easier to resolve the structure which can be seen in figure 8.4(b). There one clearly sees the edges of the two boron sheets and the middle left blank. On this picture there are also the features visible due to field distortions, like the hole at the corner of the third chip in the bottom row.

8.4 Spatial resolution

With the structure measurements one can get an estimate for the spatial resolution. Although the data set is quite small and with higher statistics the spatial resolution would most likely improve, an attempt was made in order to determine the spatial resolution. As a first step the measured data was correctly arranged, as the chips of the Octoboard are not right next to each other. There is a small gap between the chips and additionally the pixels do not stretch all the way to the edges. Thus the data for all the chips had to be separated by a fixed amount. The distance between the edges of the chips is 22 pixels. In order to suppress the field distortions on the edges of each chip the space there was cut away. The cut was 45 pixels from the edge, thus the central part consisting of 42 percent of the chip was only considered. This can be seen in figure 8.5.

In order to determine a spatial resolution a two dimensional step function would be perfect to be fitted to the data. This is not easily possible, because of the low statistics and the gaps between the filled areas. Thus instead a line was adjusted to the edge, where the boron sheet ended. Then the distance of all points to the line is calculated and inserted into a histogram. This way the two dimensional problem is converted to a one dimensional fit. To determine the spatial resolution a one dimensional error function was fitted to the histogram. This way one can obtain the spatial resolution as the width of the error function. Of course this depends on the line that was initially chosen to fit the edge, so the slope of the line was varied and the best was chosen. The way to determine the best line was by varying the slope and optimizing the width of the error function. The y-intersection of the line is not relevant for the spatial resolution, as it only results in a shift of the error function and has no influence on the width.

As there are two edges possible to fit one can try to do it for both. Upon attempting that it turned out that the bottom edge was not perfectly straight, but a little curved. This can be explained by looking at the fixation of the boron coated aluminum sheets. The one which is on the bottom was slightly lifted with a curvature from the cathode, thus the field distortions could yield such a curvature. The other one was placed flat onto the cathode, thus no curvature could be observed. Both views can be seen in figure A.7. Due to the curvature only the upper

edge could be used to determine the spatial resolution. The final result for the spatial resolution can be seen in figure 8.6. The spatial resolution is (2.106 ± 0.213) pixels which is equivalent to (115.8 ± 11.7) μm. The resolution can still be improved by a better reconstruction algorithm, where the full shape of the track can be fitted, and also more statistics in order to use stricter cuts for the data reconstruction.

8.5 Neutron spectrum

With the measurement that was used to determine the spatial resolution also the spectrum could be determined. This was done by adding all TOT values of all pixels of one track together, as that corresponds to the energy deposited by that track. This way one can determine the spectrum of the neutron conversion products. The spectrum is shown in figure 8.7(a), and the expected spectrum can be seen in figure 8.7(b). For the measurement one clearly sees the same structure if one compares it to the expected spectrum. For low energies the part is cut away due to the reconstruction algorithm. Then the peak follows and the plateau is clearly visible. The second peak corresponds the the second peak in the expected spectrum. The part that is missing is the minimum between the plateau and the second peak. It is missing, because the second peak is shifted into the minimum. This is the case due to the limited size of the chip. The high energy tracks are very likely to be cut at the corners of a chip, thus the peak will shift towards lower energies. So in total the measured spectrum clearly corresponds to the expected spectrum.
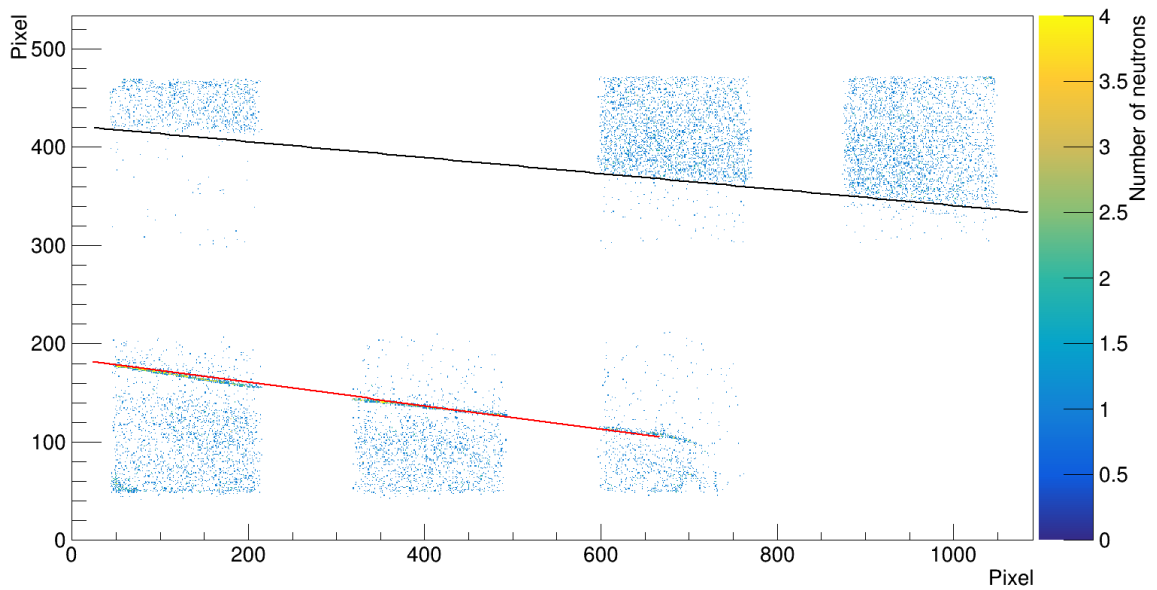
Figure 8.5: Here the interaction points that are used for the determination of the spatial resolution are shown. The edges of the chips are cut away in order to remove the effects of the field distortions on the reconstructed interaction points. Additionally the correct spacing between the chips was applied in order to position them correctly. Then the lines were adjusted by hand and the spatial resolution was calculated. The bottom, red, line could not be used for the determination of the spatial resolution, as the measured line shows a curvature, which is explained in the text. The top, black, line was used to determine the spatial resolution by varying the slope and choosing the optimal one. In order to obtain the best spatial resolution only a subset of all measured data was considered. Only the data measured with Ar CO_2 80:20 was taken for this calculation.
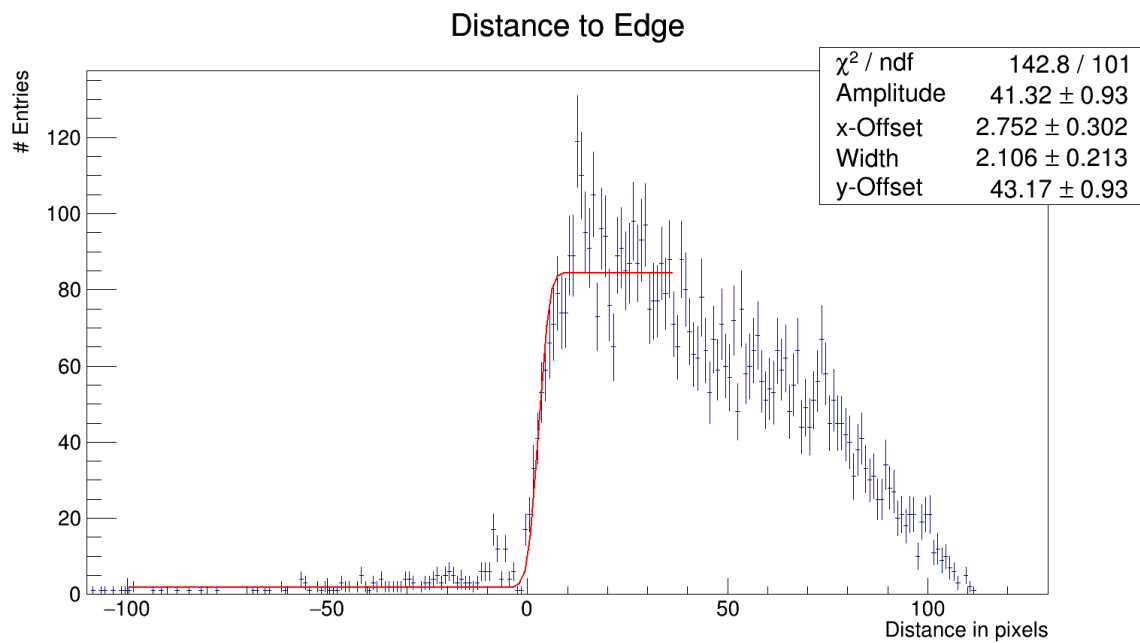
Figure 8.6: Here the histogram used for the determination of the spatial resolution is shown. The distance of all measured points to the line which describes the edge best was calculated and depicted here. Then an error function was fitted and the width of the error function corresponds to the spatial resolution. The width is given in pixels, where one pixel has a size of 55 μm. The decline of of the upper plateau is due to the lower number of points towards longer distances towards the track. There are less points, because the chips end at some point and some end earlier than the others.
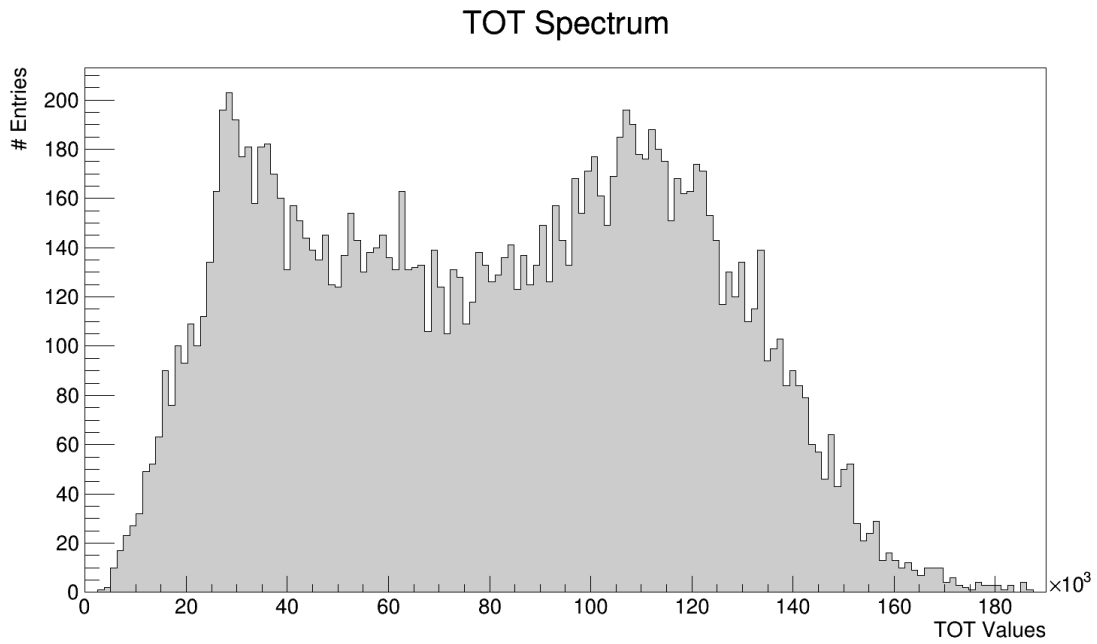
TOT Spectrum

(a) Measured neutron conversion spectrum.

Converted neutron spectrum with 30%FWHM resolution
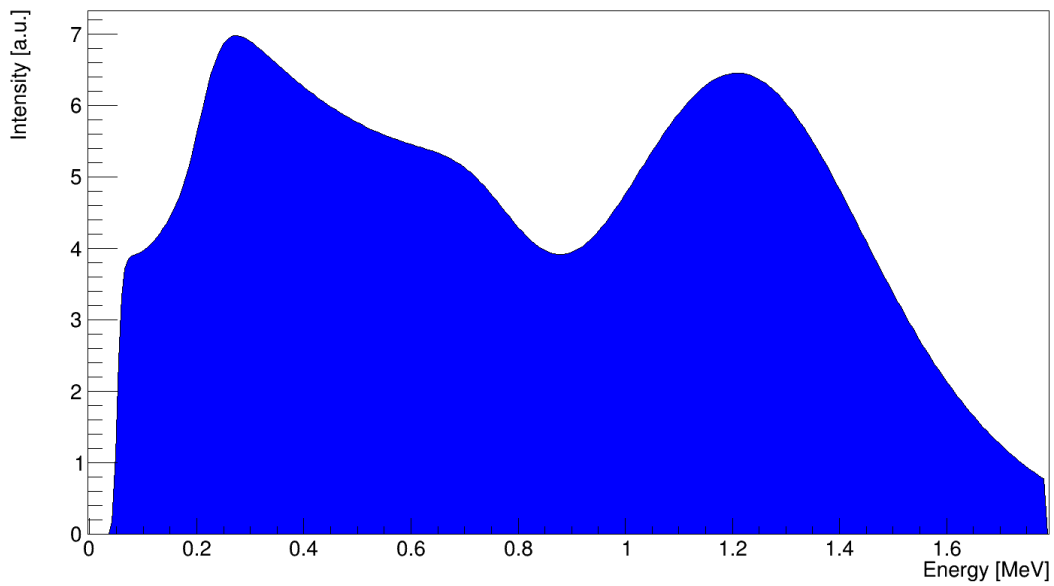
(b) Simulated neutron conversion spectrum [10]

Figure 8.7: The measured neutron conversion spectrum is shown in the first picture. Comparing it to the simulated spectrum (second picture) for a boron layer of 1 μm thickness with a resolution of 30 percent one can see that they match, as described in the text. The TOT values are proportional to the energy.

Conclusion & Outlook

During the year for this master thesis the detector concept for the BASTARD detector and a working prototype for the BODELAIRE detector was being developed.

The BASTARD detector consists of GEM foils, which are made of five layers of alternating copper and kapton with the lowest copper layer coated with boron. The top and middle layer of the foils are segmented into strips and contain the holes. The bottom layer is a solid copper layer. The kapton layers are in between the copper layers to shield then from each other. The structure for the two layers with strips was developed and turned out to have two different pitches for the two perpendicular directions, as the holes are arranged in a hexagonal pattern. The pitches are $242.5\,\mu m$ and $280\,\mu m$. The details of the patterns can be seen in chapter 4.2. Also the frame for the GEM foils was developed including the mounting of multiple modules with each other. The BASTARD detector is modular and can be extended to several layers of GEM foils for an increase of neutron detection efficiency due to more boron layers.

The BODEALIRE detector was already existent as a design, but some prototyping had to be done. The BODELAIRE detector works with the principle of a time projection chamber with boron coated walls. The walls work as a field cage, trigger and conversion material all together. As the boron is coated on a scintillator the neutron conversion products will yield a light signal used as a trigger and a track inside the gas volume of the time projection chamber. This way a three dimensional reconstruction of the track is possible and the neutron interaction point can be reconstructed. The main question was how converted neutrons will look like on a GridPix readout and how to reconstruct them properly. Therefore a prototype was built during the course of the master thesis. The prototype has a boron coated cathode on top of a GridPix readout. The neutrons will convert at the boron layer and the track will drift towards the readout. It turned out that it was possible to run the detector at a low gas gain, as the neutron conversion products are highly ionizing. The tracks are easily visible on the GridPix and could be detected and reconstructed quite good. The only obstacle to overcome was the determination of the interaction point, as there is no easy way to distinguish the start- and endpoint of the track. In order to solve this problem an additional measurement mode had to be enabled on the Timepix chip. In addition to the charge information timing information had to be gained by changing some of the pixels to time measurement mode. In order to get the timing information the detector had to be run with an external trigger, due to the low neutron rate of the source and possible

overflow in the timing counter. The timing information of the arrival of the track solved the problem for the reconstruction.

With the setup built during the master thesis a structure of boron strips could be resolved, which can be seen in chapter 8. The measurement of the structure also made it possible to obtain an estimate for the spatial resolution. This was done by fitting a line to the edge of the measured boron strip and determining the deviation of the reconstructed structure from a straight line. The spatial resolution turned out to be $(115.8 \pm 11.7)\,\mu$m. It can still be improved by adding more statistics and also improving the reconstruction algorithm. Also with more statistics the cuts can be made tighter. An other step into the direction of BODELAIRE would be to turn the boron layer by 90 degrees, as the boron layer was not vertical to the readout plane as it will be in the final design. For a vertical orientation of the born layer the reconstruction will also change, as there is a clear plane where the track had to originate from vertical to the readout plane.

Summing up, the structure of the GEM foils for the BASTARD detector was developed and the mounting of those was designed. For BODELAIRE a prototype detector was built and with it a structure of boron strips could be resolved. With the structure also the spatial resolution of the prototype could be determined.

Bibliography

[1] J. Chadwick, *Possible Existence of a Neutron*, Nature **129** (1932) 312, URL:
     `http://www.nature.com/nature/journal/v129/n3252/pdf/129312a0.pdf`
     (cit. on p. 3).

[2] H. Becker and W. Bothe, *Die in Bor und Beryllium erregten γ-Strahlen*,
     Zeitschrift für Physik **76** (1932) 421, ISSN: 0044-3328,
     URL: `http://dx.doi.org/10.1007/BF01336726` (cit. on p. 3).

[3] H. Abele, *The neutron. Its properties and basic interactions*,
     Progress in Particle and Nuclear Physics **60** (2008) 1, ISSN: 0146-6410, URL:
     `http://www.sciencedirect.com/science/article/pii/S0146641007000622`
     (cit. on p. 3).

[4] A. Snell et al., *Studies of the Delayed Neutrons. I. The Decay Curve and the Intensity of
     the Delayed Neutrons*, Phys. Rev. **72** (7 1947) 541,
     URL: `https://link.aps.org/doi/10.1103/PhysRev.72.541` (cit. on p. 3).

[5] C. Patrignani et al., *Review of Particle Physics*, Chin. Phys. **C40** (2016) 100001
     (cit. on pp. 3, 4, 12).

[6] S. Dar, *The Neutron EDM in the SM: A Review*, 2000,
     arXiv: `hep-ph/0008248 [hep-ph]`,
     URL: `http://arxiv.org/abs/hep-ph/0008248` (cit. on p. 3).

[7] K.-H. Beckurts and K. Wirtz, *Neutron Physics*, Springer Verlag, 1964 (cit. on p. 5).

[8] J. Ziegler, M. Ziegler and J. Biersack,
     SRIM - The stopping and range of ions in matter (2010), Nuclear Instruments and
     Methods in Physics Research Section B: Beam Interactions with Materials and Atoms
     268 (2010) 1818, 19th International Conference on Ion Beam Analysis, ISSN: 0168-583X,
     URL:
     `http://www.sciencedirect.com/science/article/pii/S0168583X10001862`
     (cit. on p. 5).

[9] M. Köhli et al., *CASCADE - a multi-layer Boron-10 neutron detection system*,
     J. Phys. Conf. Ser. **746** (2016) 012003, arXiv: `1602.04064 [physics.ins-det]`
     (cit. on p. 7).

[10] M. Köhli, Private Communication (cit. on pp. 8, 38, 40, 68).

[11] W. Stacey, *Nuclear Reactor Physics*, 2nd, Completely Revised and Enlarged Edition,
     Wiley-VCH Verlag GmbH & Co. KGaA, 2007, ISBN: 0-471-39127-1 (cit. on p. 8).

[12] W. R. Leo,
      Techniques for Nuclear and Particle Physics Experiments: A How to Approach, 2nd ed.,
      1994, ISBN: 9783540572800 (cit. on p. 9).

[13] C. Leroy and P.-G. Rancoita, *Principles of Radiation Interaction in Matter and Detection*,
      2nd ed., World Scientific, 2009, ISBN: 981-281-827-8,
      URL: `http://www.worldscientific.com/worldscibooks/10.1142/8200#t=toc`
      (cit. on p. 11).

[14] W. Blum, L. Rolandi and W. Riegler, *Particle detection with drift chambers*,
      Particle Acceleration and Detection, 2008, ISBN: 9783540766834, 9783540766841, URL:
      `http://www.springer.com/physics/elementary/book/978-3-540-76683-4`
      (cit. on p. 13).

[15] S. Ramo, *Currents induced by electron motion*, Proc. Ire. **27** (1939) 584 (cit. on p. 17).

[16] W. Shockley, *Currents to Conductors Induced by a Moving Point Charge*,
      Journal of Applied Physics **9** (1938) 635,
      URL: `http://dx.doi.org/10.1063/1.1710367` (cit. on p. 17).

[17] S. Peggs, *ESS Technical Design Report*, tech. rep.,
      European Spallation Source ESS, 2013 (cit. on p. 19).

[18] F. Fernandez-Alonso and D. Price,
      Neutron Scattering – Applications in Biology, Chemistry, and Materials Science, vol. 49,
      Experimental Methods in the Physical Sciences, Elsevier Science, 2017 782,
      ISBN: 9780128053249, URL: `https://www.elsevier.com/books/neutron-`
      `scattering-applications-in-biology-chemistry-and-materials-`
      `science/fernandez-alonso/978-0-12-805324-9` (cit. on p. 19).

[19] M. Arai and K. Crawford,
      "Neutron Imaging and Applications: A Reference for the Imaging Community",
      ed. by I. Anderson, R. McGreevy and H. Bilheux,
      Neutron Scattering Applications and Techniques, Springer US, 2009,
      chap. Neutron Sources and Facilities 13, ISBN: 9780387786933,
      URL: `http://link.springer.com/book/10.1007%2F978-0-387-78693-3`
      (cit. on p. 19).

[20] F. Sauli, *The gas electron multiplier (GEM): Operating principles and applications*,
      Nucl. Instrum. Meth. **A805** (2016) 2 (cit. on pp. 20, 21).

[21] D. R. Nygren, *The Time Projection Chamber: A New 4 pi Detector for Charged Particles*,
      eConf **C740805** (1974) 58 (cit. on p. 20).

[22] M. Chefdeville et al., *An electron-multiplying Micromegas grid made in silicon wafer
      post-processing technology*,
      Nuclear Instruments and Methods in Physics Research Section A: Accelerators,
      Spectrometers, Detectors and Associated Equipment **556** (2006) 490, ISSN: 0168-9002,
      URL:
      `http://www.sciencedirect.com/science/article/pii/S0168900205021418`
      (cit. on p. 21).

[23] C. Krieger et al., *A GridPix-based X-ray detector for the CAST experiment*,
Nuclear Instruments and Methods in Physics Research Section A: Accelerators,
Spectrometers, Detectors and Associated Equipment **867** (2017) 101, ISSN: 0168-9002,
URL:
`http://www.sciencedirect.com/science/article/pii/S0168900217304400`
(cit. on p. 21).

[24] X. Llopart et al., *Timepix, a 65k programmable pixel readout chip for arrival time,
energy and/or photon counting measurements*,
Nuclear Instruments and Methods in Physics Research Section A: Accelerators,
Spectrometers, Detectors and Associated Equipment **581** (2007) 485 , VCI 2007,
ISSN: 0168-9002, URL:
`http://www.sciencedirect.com/science/article/pii/S0168900207017020`
(cit. on pp. 21, 23).

[25] X. Llopart et al., "Medipix2, a 64k pixel read out chip with 55 μm square elements
working in single photon counting mode",
2001 IEEE Nuclear Science Symposium Conference Record (Cat. No.01CH37310),
vol. 3, Vol. 3, 2001 1484, ISBN: 0-7803-7324-3,
URL: `http://ieeexplore.ieee.org/document/1008618/` (cit. on p. 21).

[26] T Poikela et al., *Timepix3: a 65K channel hybrid pixel readout chip with simultaneous
ToA/ToT and sparse readout*, Journal of Instrumentation **9** (2014) C05013,
URL: `http://stacks.iop.org/1748-0221/9/i=05/a=C05013` (cit. on p. 22).

[27] C. Krieger, Private Communication (cit. on p. 23).

[28] T. Krautscheid et al., *Gridpix: Production and application of integrated pixel readouts*,
Nuclear Instruments and Methods in Physics Research Section A: Accelerators,
Spectrometers, Detectors and Associated Equipment **718** (2013) 391, Proceedings of the
12th Pisa Meeting on Advanced Detectors, ISSN: 0168-9002, URL:
`http://www.sciencedirect.com/science/article/pii/S0168900212011904`
(cit. on p. 22).

[29] J. Kaminski, Private Communication (cit. on p. 24).

[30] M. A. Chefdeville, *Development of Micromegas-like gaseous detectors using a pixel
readout chip as collecting anode*, PhD thesis: University of Amsterdam, 2009
(cit. on p. 24).

[31] C. Krieger, *Construction and First Measurements of a GridPix based X-ray Detector*,
MA thesis: Universität Bonn, 2011 (cit. on p. 25).

[32] S. Martoiu et al., *Development of the Scalable Readout System for micro-pattern gas
detectors and other applications*, Journal of Instrumentation **8** (2013) C03015,
URL: `http://stacks.iop.org/1748-0221/8/i=03/a=C03015` (cit. on p. 26).

[33] M. Lupberger et al.,
Toward the Pixel-TPC: Construction and Operation of a Large Area GridPix Detector,
IEEE Transactions on Nuclear Science **64** (2017) 1159, ISSN: 0018-9499,
URL: `http://ieeexplore.ieee.org/document/7889045/` (cit. on p. 26).

[34] Xilinx, *Virtex-6 FPGA Overview*,
`https://www.xilinx.com/support/documentation/data_sheets/ds150.pdf`,
2017, URL:
`https://www.xilinx.com/support/documentation/data_sheets/ds150.pdf`
(cit. on p. 28).

[35] M. Lupberger, K. Desch and J. Kaminski,
Implementation of the Timepix ASIC in the Scalable Readout System,
Nuclear Instruments and Methods in Physics Research Section A: Accelerators,
Spectrometers, Detectors and Associated Equipment **830** (2016) 75 , ISSN: 0168-9002,
URL:
`http://www.sciencedirect.com/science/article/pii/S0168900216304235`
(cit. on p. 28).

[36] P. Milde et al., *Unwinding of a Skyrmion Lattice by Magnetic Monopoles*,
Science **340** (2013) 1076, ISSN: 0036-8075,
eprint: `http://science.sciencemag.org/content/340/6136/1076.full.pdf`,
URL: `http://science.sciencemag.org/content/340/6136/1076` (cit. on p. 31).

[37] L. Hirose Electronic CO., *Specification sheet FX10A-140P/14-SV*,
URL: `https://www.hirose.com/product/en/download_file/key_name/FX10A-140P__14-SV%2891%29/category/Specification%20Sheet/doc_file_id/40351/?file_category_id=9&item_id=05700004391&is_series=`
(cit. on p. 35).

[38] F. Piegsa et al., *Neutron spin phase imaging*, Nuclear Instruments and Methods in
Physics Research Section A: Accelerators, Spectrometers, Detectors and Associated
Equipment **586** (2008) 15 , Proceedings of the European Workshop on Neutron Optics,
ISSN: 0168-9002, URL:
`http://www.sciencedirect.com/science/article/pii/S0168900207023819`
(cit. on p. 37).

[39] C. W. Clark et al., *Controlling neutron orbital angular momentum*,
Nature **525** (2015) 504, Letter, ISSN: 0028-0836,
URL: `http://dx.doi.org/10.1038/nature15265` (cit. on p. 37).

[40] F. Schmidt, *Entwicklung eines SiPM-Szintillationstriggers für einen Neutronendetektor*,
Bachelor Thesis: Physikalisches Institut, University of Bonn, 2017 (cit. on p. 39).

[41] L. Weber,
Konzeption und Bau eines Szintillationstriggers zur Detektion thermischer Neutronen,
Bachelor Thesis: Physikalisches Institut, University of Bonn, 2017 (cit. on p. 39).

[42] SolidWorks, *SolidWorks Website*, URL: `http://www.solidworks.com` (cit. on p. 41).

[43] M. Köhli et al., *URANOS - The Ultra Rapid Adaptable Neutron-Only Simulation for
Environmental Research*, URL:
`http://www.physi.uni-heidelberg.de/Forschung/ANP/Cascade/URANOS/`
(cit. on p. 45).

[44] arduino.cc, *Arduino Nano*,
URL: https://www.arduino.cc/en/uploads/Main/ArduinoNanoManual23.pdf
(cit. on p. 44).

[45] J. Weimar,
Entwicklung und Charakterisierung eines ^{10}B-basierten Neutronendetektors im Rahmen der COSMOS-Methode zur Bestimmung von Bodenfeuchte auf der Hektarskala,
Master Thesis: Physikalisches Institut, Heidelberg University, 2017 (cit. on p. 45).

[46] M. Ester et al.,
"A density-based algorithm for discovering clusters in large spatial databases with noise",
AAAI Press, 1996 (cit. on p. 49).

[47] Chire, *DBSCAN Illustration*,
https://commons.wikimedia.org/wiki/File:DBSCAN-Illustration.svg,
[Online; accessed 05 July 2017], 2011 (cit. on p. 50).

[48] R. Brun and F. Rademakers, *ROOT: An object oriented data analysis framework*,
Nucl. Instrum. Meth. **A389** (1997) 81 (cit. on p. 50).

[49] Y. Assran and A. Sharma, *Transport Properties of operational gas mixtures used at LHC*,
(2011), arXiv: 1110.6761 [physics.ins-det] (cit. on p. 55).

Additional plots

As mentioned in chapter 7.2 more examples of tracks and also some that were rejected are depicted in the following figures. Also figures depicting the cathode, as mentioned in chapter 8.4, are shown.
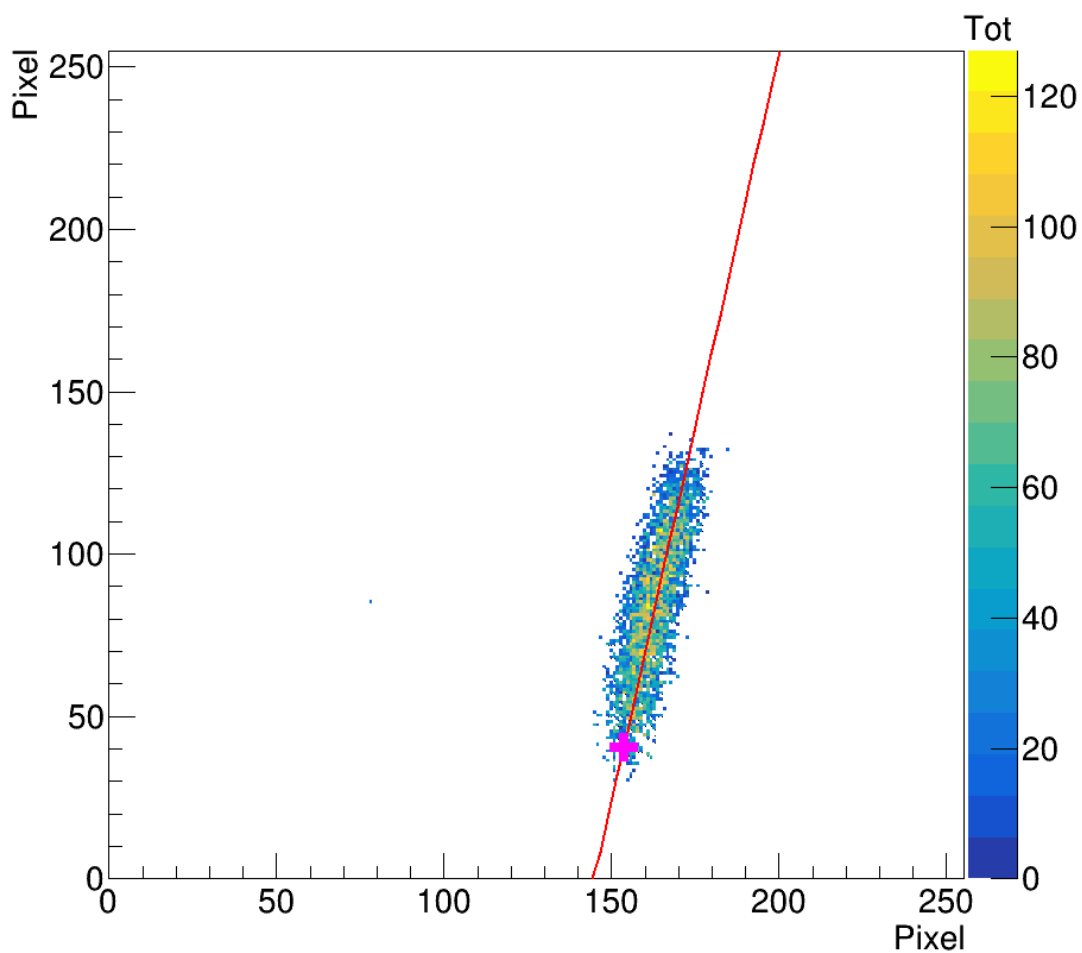
Figure A.1: This is a helium track candidate due to the size and the homogeneous ionization distribution.
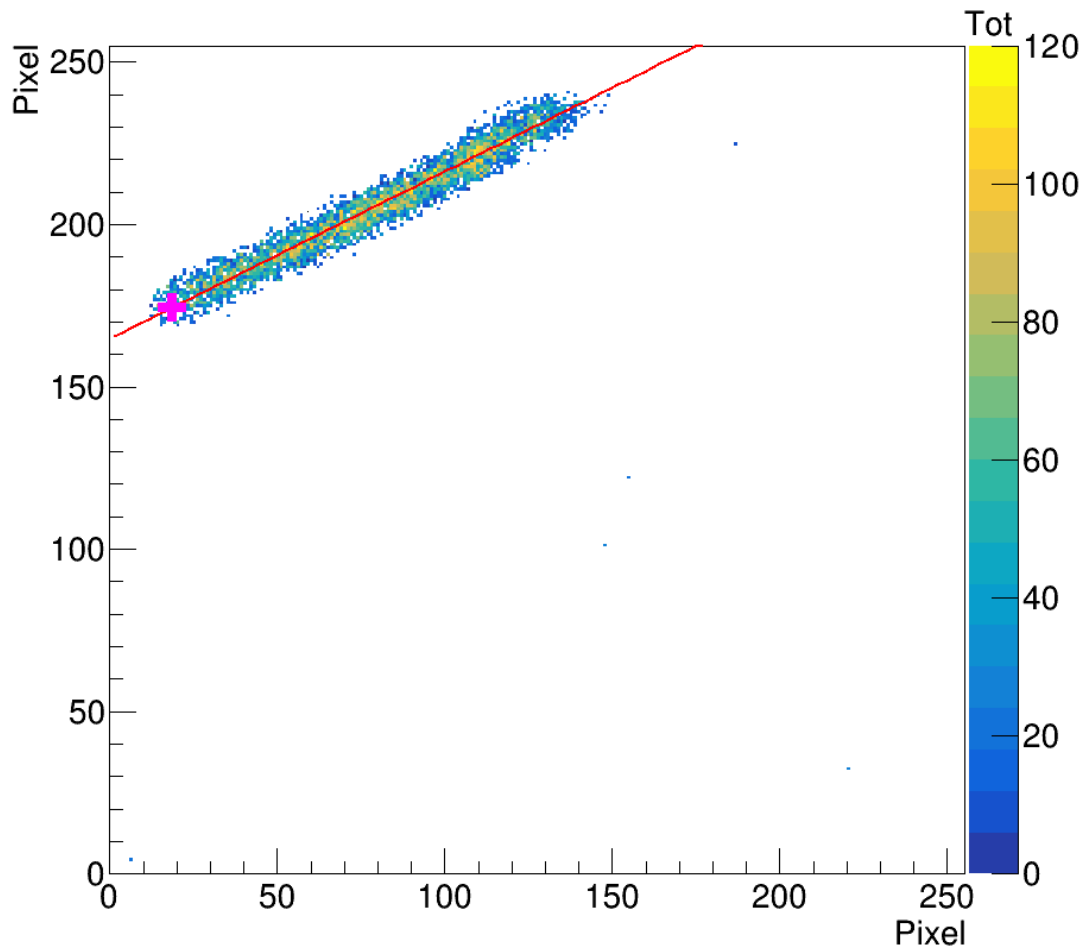
Figure A.2: This is a helium track candidate due to the size and the homogeneous ionization distribution.
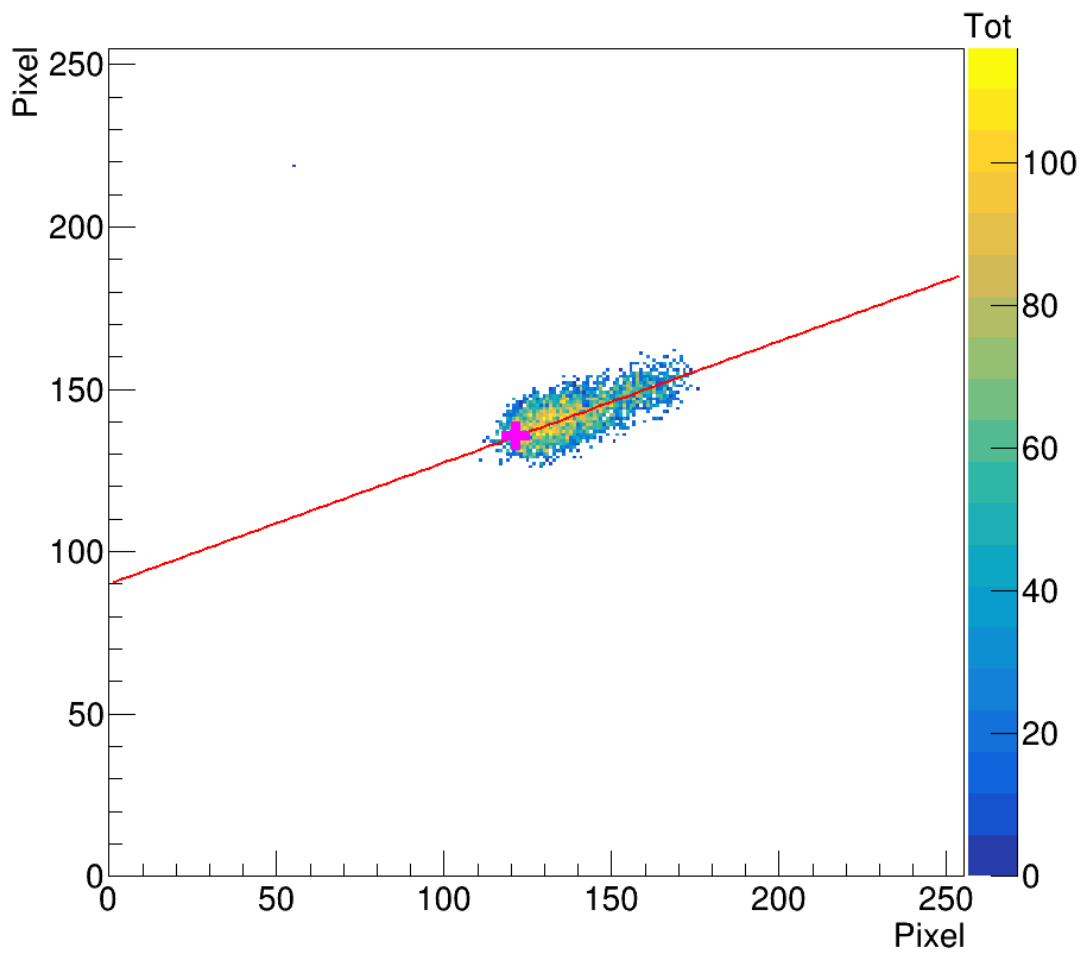
Figure A.3: This is how a typical lithium track looks like. It deposits most of its energy at the start of the track and is very short.
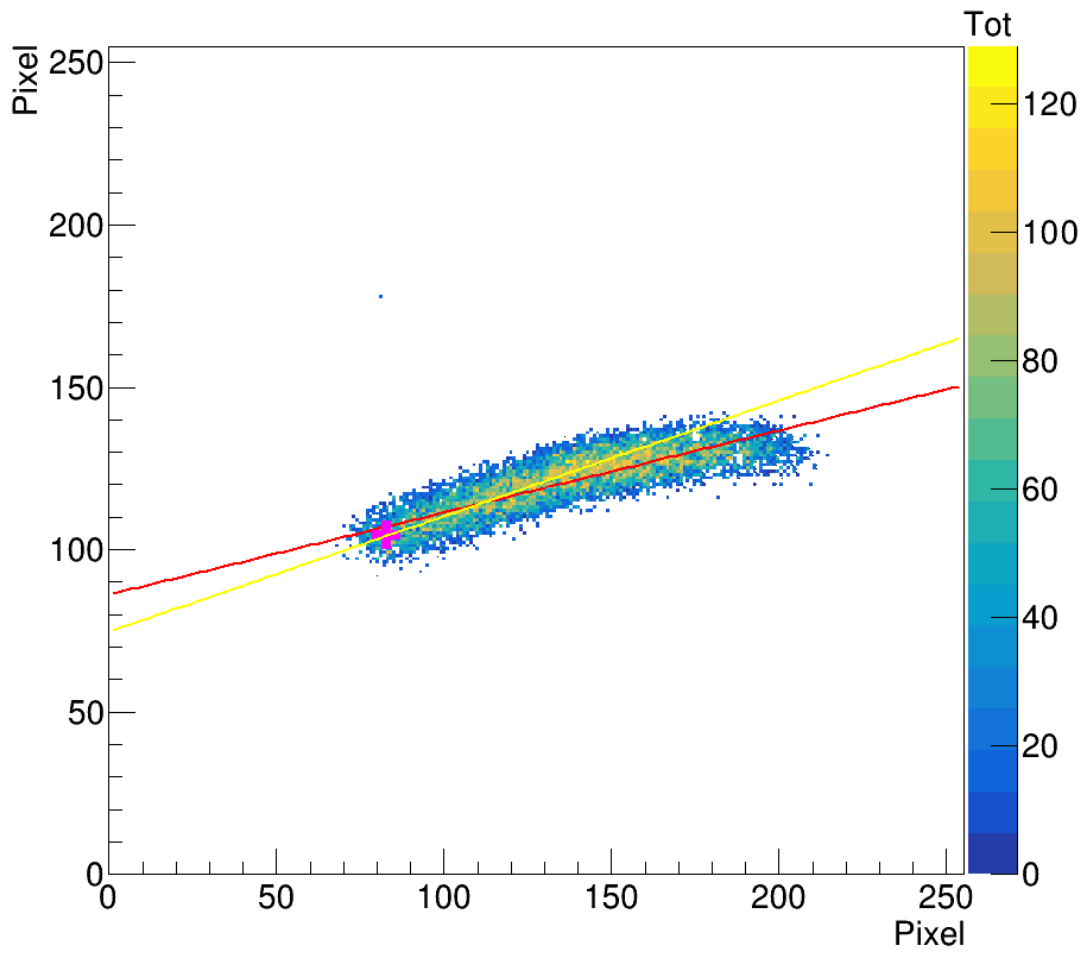
Figure A.4: This is a curved track. It was flagged for a refit, because it shows a curvature. The red line is the first fit and the yellow line is the second fit where only the half with the interaction point is taken. After the new fit it is accepted as a good reconstruction.
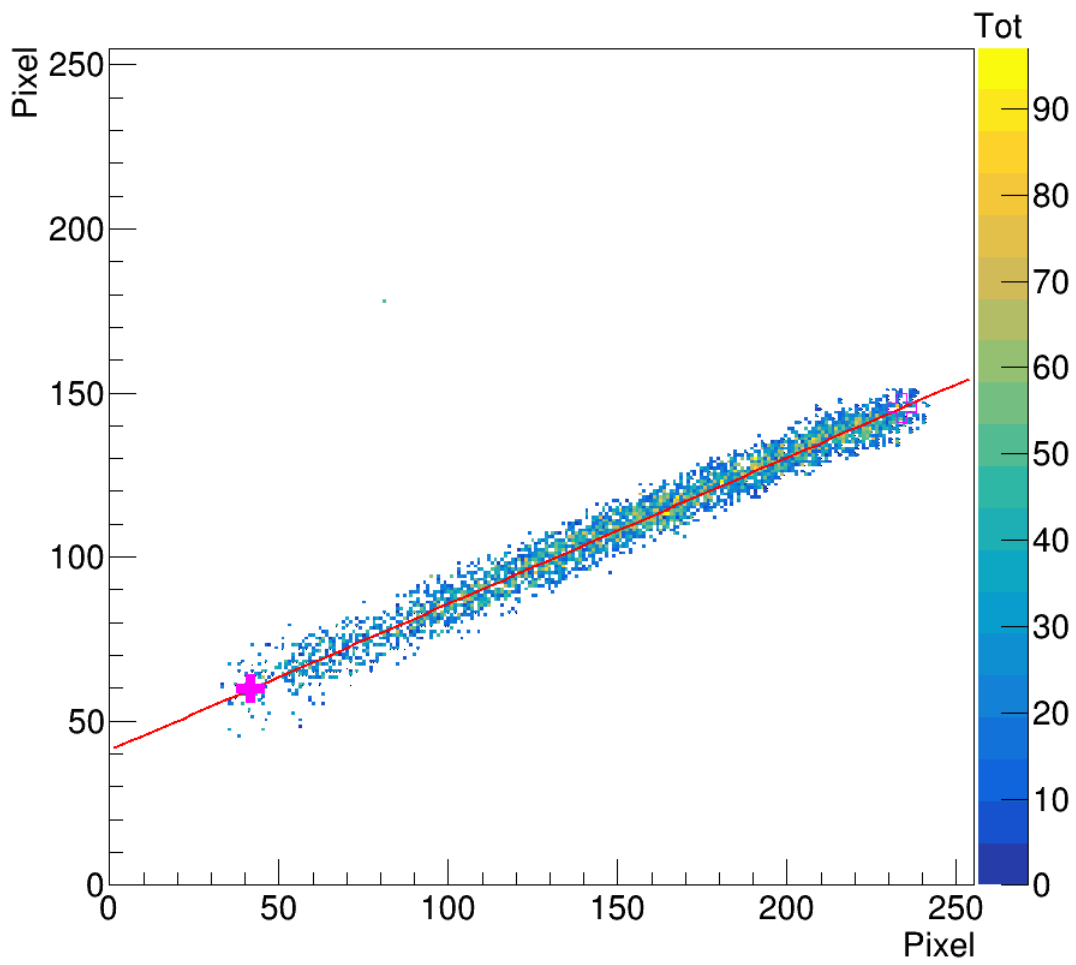
Figure A.5: This is a rejected track. It was rejected because the track is too long. This track is longer than the range a conversion product could have. It is most likely a proton, which traversed the detector.
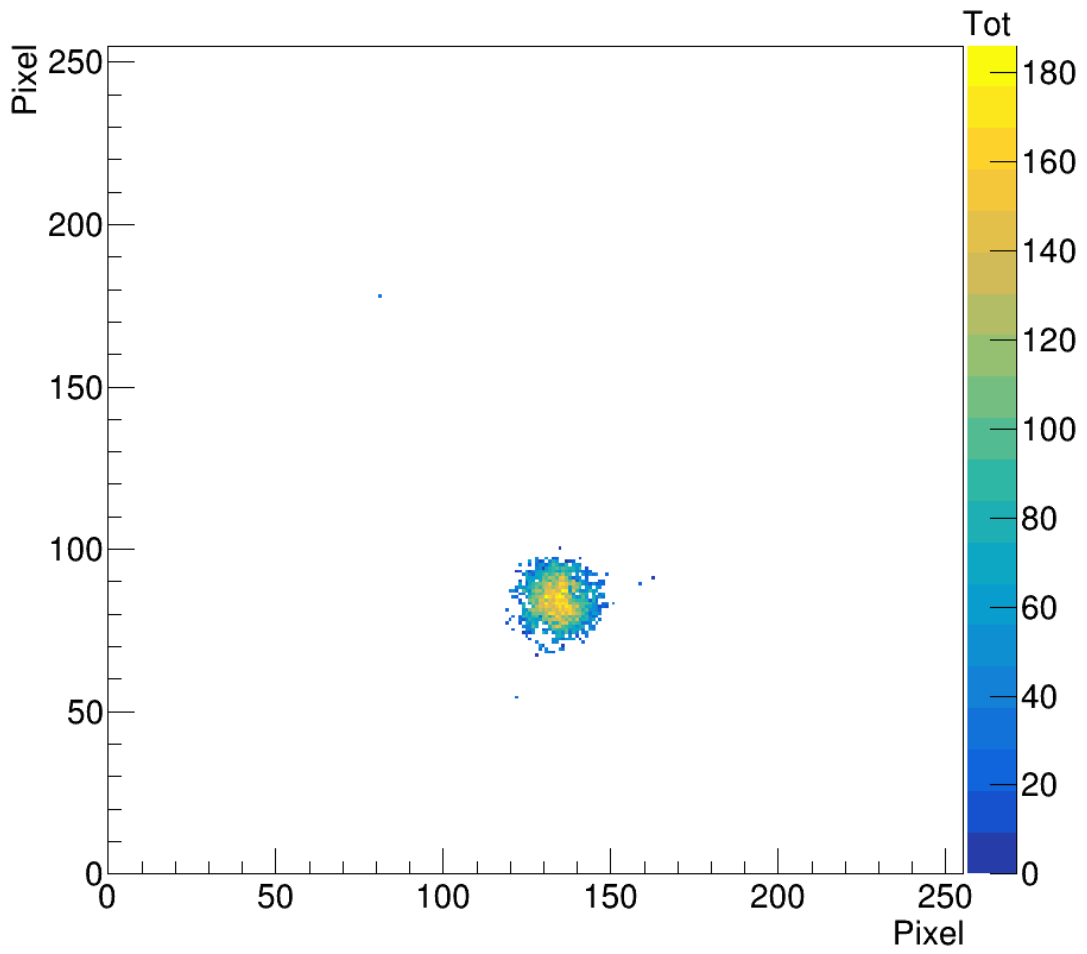
Figure A.6: This is a rejected track. It was rejected because it is too circular, thus the direction could not be determined.
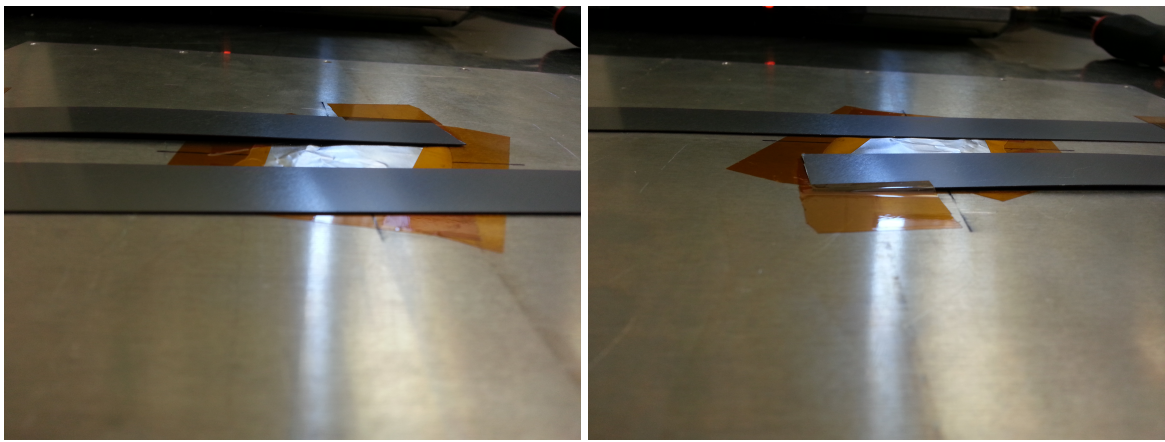
(a) Picture taken from top side.   (b) Picture taken from bottom side.

Figure A.7: The two pictures show the two boron coated aluminum strips which are mounted on the cathode. The first picture is taken from the top side, thus the strip on the far side corresponds to the lower one in the distributions of the interaction points. One can see that the strip is bent slightly, thus field distortions can occur. The second picture is taken from the other side, so the far strip corresponds to the upper one. There one can see that this strip lies flat on top of the cathode and is not bent. This leads to a straight edge in the measurements. The aluminum foil in the middle is there to cover a hole in the cathode, as it was also used for testing the detector and needed a possibility to mount radioactive sources inside.

List of Figures

List of Tables